Universität Stuttgart
Institut für
Statik und Dynamik

University of Cambridge
Department of Engineering

Gravity Compensation of Deployable Solar Arrays for Small Spacecraft

Diploma Thesis submitted to the Universität Stuttgart
for the degree of Diplom-Ingenieur

by

Daniel Schultheiß

November 2003

Declaration

The author declares that, except for commonly understood and accepted ideas, or where specific references is made to the work of other authors, the contents of this *Diplomarbeit* (diploma thesis) are his own work and contain nothing that is the outcome of work done in collaboration. This *Diplomarbeit* has not been previously submitted for any degree, diploma or other qualification. This *Diplomarbeit* is presented in 76 pages and contains approximately 21000 words, excluding bibliography and appendices.

Acknowledgement

I would like to thank my supervisor Prof. Sergio Pellegrino, University of Cambridge, for his guidance and encouragement. I would also like to thank Paul Charman and Guy Richardson, Surrey Satellite Technology Ltd, for their external help. I would like to thank Alan Watt for his help in designing. I would also like to thank the members of the Structures group for their companionship and assistance. I am especially grateful to Matthew Santer for his continuous help in linguistic problems. I would also like to thank Roger Denton and Peter Knott for their help and technical assistance and the workshop staff for their accurate manufacture of many parts.

I would like to thank Prof. Bernd Kröplin, Universität Stuttgart, for introducing me to Prof. Sergio Pellegrino. Furthermore, I would like to thank Peter Kungl for supervising and assisting during this *Diplomarbeit*.

I was given financial aid by several persons and institutions. I would like to thank my parents, Prof. Sergio Pellegrino, the Flughafen Frankfurt Main Stiftung, the Hermann Reissner Stiftung, and the German Ministry of Education and Research for BAföG.

Finally, I would like to thank my parents and brothers.

Contents

List of Tables

List of Figures

Notation

Important and Often-Used Variables

eq	equation of motion constraint number
g	gravity accelleration constant
$i,\ j,\ k$	index variables, if not mentioned differently, ranging from 1 to 3
l	length of panel 2 and 3, double length of panel 1
l_s	length of suspension string
la	latching process number
m_i	mass of panel i
m_h	mass of supports and tape springs in one hinge line
m_r	mass of transverse rail and belonging longitudinal trolleys
m_t	(1) mass of one trolley (2) mass of transverse trolley
q_{ij}	coefficients of transformation matrix
s_p	separation distance between two panels
t	time
$u,\ v$	coordinates in the image system
$x,\ y,\ z$	(1) cartesian coordinates (2) coordinates in the world system
$x_1 \dots x_6$	coordinates of panels' centre
$E_{a,kin}$	kinetic energy of the array
$E_{s,pot}$	potential energy of the release spring
F	force (general); restoring force
F_n	normal force
$(F_{susp,y})_i$	horizontal component of the force in suspension string $i = 1, 2$
$(F_{susp,z})_i$	vertical component of the force in suspension string $i = 1, 2$
F_μ	force of friction
H	set of equations containing only holonomic constraint conditions
H_i	hinge line i
I_i	mass moment of inertia of panel i
L_i	angular momentum of panel i
M_{h0}	constant torsion moment in hinge line
M_{hi}	torsion moment in hinge line H_i
$\mathrm{R}_1 \dots \mathrm{R}_8$	restriction number
$(S_M)_i$	angular impulse at hinge line H_i
Δt	integration step size
$\Delta\theta_{Hi}$	opening angle of hinge line H_i
$\epsilon_1,\ \epsilon_2$	(very small) positive constants
ϕ_i	generalized variables
μ	coefficient of friction
μ_{kin}	coefficient of kinetic friction
μ_{stat}	coefficient of static friction
μ_x	μ in longitudinal direction
μ_y	μ in transverse direction
θ_i	angle of panel i against x-axis
$\boldsymbol{c_i}$	auxilary vectors
$\boldsymbol{g}$	gravity acceleration vector
$\boldsymbol{m_p}$	matrix of panel masses
$\boldsymbol{p}_i$	vector of panel i's linear momentum
$\boldsymbol{u}$	pointing vector in the image coordinate system
$\boldsymbol{x}$	(1) vector of all panel centre coordinates (2) pointing vector in the world coordinate system
$\boldsymbol{x}_i$	position vector of the panel i
$\boldsymbol{x}_\mathrm{H}$	vector of hinge line coordinates
$\boldsymbol{x}_{\mathrm{H}_i}$	position vector of hinge line H_i

$\boldsymbol{x_{susp}}$	position vector of y-coordinates of suspension points
$\boldsymbol{x_t}$	position vector of the x-coordinates of the trolleys
$\boldsymbol{y}$	vector of the y-coordinates of the panel's centre
$\boldsymbol{z}$	vector of the z-coordinates of the panel's centre
$\boldsymbol{B}$	impulse matrix
$\boldsymbol{C_i}$	auxilary matrixes
$\boldsymbol{E}$	identity (eye) matrix
$\boldsymbol{F_n}$	vector of normal forces
$\boldsymbol{F_{susp}}$	vector of forces in suspension strings
$\boldsymbol{F_{susp,y}}$	vector of y-components of forces in suspension strings
$\boldsymbol{F_{susp,z}}$	vector of z-components of forces in suspension strings
$\boldsymbol{F_\mu}$	vector of forces of friction
$\boldsymbol{I_p}$	matrix of panel mass moments of inertia
$\boldsymbol{J}$	Jacobian matrix
$\boldsymbol{M}$	system mass matrix
$\boldsymbol{M_h}$	vector of the hinge line moments
$\boldsymbol{Q}$	system load vector
$\boldsymbol{S_F}$	vector of all linear impulses
$\boldsymbol{S_M}$	vector of all angular impulses
$\boldsymbol{W_h}$	vector of work in hinge lines due to bending of tape springs
$\boldsymbol{W_{\ddot{x}}}$	vector of work due to panels' translation
$\boldsymbol{W_{susp}}$	vector of work due to forces in suspension strings
$\boldsymbol{W_t}$	vector of work due to trolley's translation
$\boldsymbol{W_{tx}}$	vector of work due to translation of longitudinal moving parts
$\boldsymbol{W_{ty}}$	vector of work due to translation of transverse moving parts
$\boldsymbol{W_{tot}}$	vector of the system's total work
$\boldsymbol{W_\mu}$	vector of work due to friction between trolley and rail
$\boldsymbol{W_{\mu x}}$	vector of work due to friction between long. trolley and rail
$\boldsymbol{W_{\mu y}}$	vector of work due to friction between transverse trolley and rail
$\boldsymbol{W_{\ddot{\theta}}}$	vector of work due to panels' rotation
$\boldsymbol{\Delta\theta_h}$	vector of the opening angles of the hinge lines
$\boldsymbol{\delta}^{(i)}$	modified Kronecker matrices
$\boldsymbol{\phi}$	vector of generalized variables
$\boldsymbol{\mu}$	coefficient matrix of friction
$\boldsymbol{\theta}$	angle vector of the array

Subscripts

new	new values (after integration step)
old	old values (before integration step)

Superscripts

a	after latching
b	before latching
$*$	including four-rail suspension system

Operators

∂	partial differentiation of
δ	virtual
Δ	(1) change of (2) error of
$\forall$	for all
$\in$	element of
$\notin$	not element of
$\dot{\square}$	first derivative of $\square$ w.r.t. time
$\ddot{\square}$	second derivative of $\square$ w.r.t. time

Abbreviations

CFRP	Carbon Fibre Reinforced Plastic
DLR	Deutsches Zentrum für Luft- und Raumfahrt
DSL	Deployable Structures Laboratory of University of Cambridge
MDF	Medium Density Fibre Board
SSTL	Surrey Satellite Technology Ltd.
stddev	standard deviation
ZSRM	Zero Spring Rate Mechanism

Chapter 1

Introduction

1.1 Project Background

The company Surrey Satellite Technology Ltd (SSTL) is currently investigating design concepts for low cost rigid arrays, which is a part of the BNSC[1] study into high power solar arrays for small satellites. The aim is to develop a 1 kW deployable array for an affordable small satellite with a lifetime of 7 years The array design should be scalable upwards to meet future power demands of up to 2 kW.

In the initial stage of the study a range of rigid array concepts was defined. From these a preferred concept was selected. One concept design can be seen in figure 1.1. This design was taken onto the next stage of the project where it was considered in a more detailed level.

The rigid array must undergo extensive ground validation tests to ensure reliability and function-

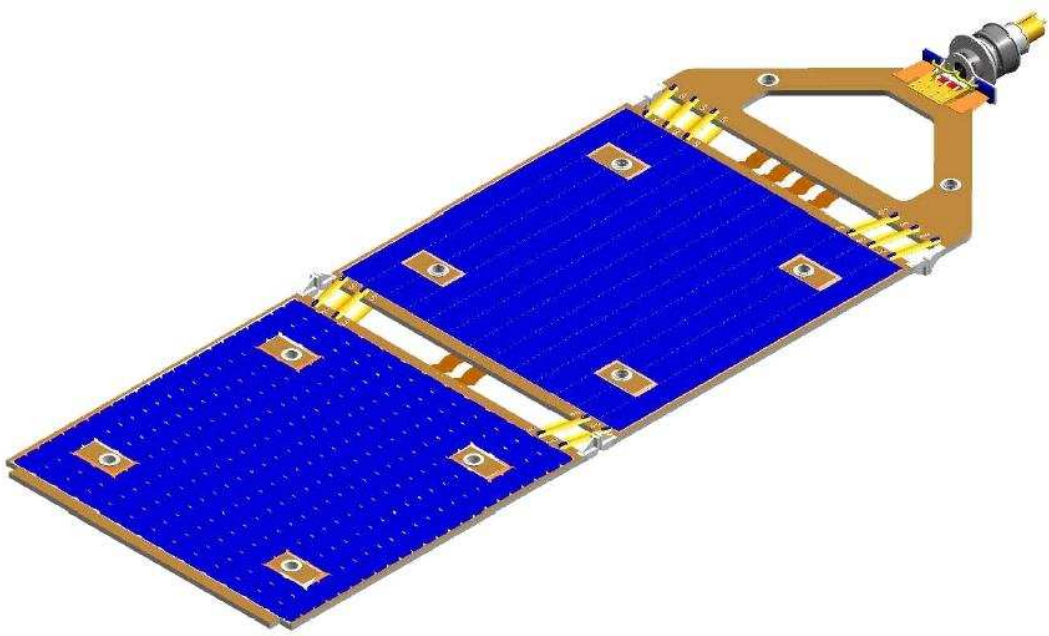

Figure 1.1: Rigid Array Concept Design in Deployed Configuration

[1] British National Space Centre

ality in space. One task is to prove that the array will deploy fully and without any complications. This is the task that was delegated to the Deployable Structure Laboratory (DSL) of the Cambridge University Engineering Department.

1.2 The Rigid Array

The concept necessitating further investigation is shown in figure 1.1. The array shall consist of two wings each consisting of two panels and one yoke. These three main parts of one wing are connected by hinge lines. The hinge lines are made up of tape springs. The yoke is joined to the spacecraft by the root hinge, which again is composed of tape springs.

One solar panel is approximately 1.2 m long, 1 m wide and 15 mm thick. It is made from aluminium honeycomb core with 0.4 mm thick carbon fibre skins. The masses of the inner and outer panel including solar cells are 4.6 kg and 4.5 kg, respectively. The yoke is made of the same material and is half as long as one panel. The mass of the yoke is 1 kg.

The main parts of the hinge lines are tape springs which are cut from normal tape-measure or made from unpainted tape. In this state of design, in each hinge line four tape springs are mounted (differently drawn in figure 1.1). The tape springs fulfill three main functions:

- they connect the panels, the yoke and the satellite
- in a bent configuration they provide the moment to deploy the array
- in a deployed configuration they ensure the alignment of the panels

Detailed information about hinges with tape strings can be found in [15].

1.3 Gravity Compensation Systems

Testing the deployment of a solar array on earth is mandatory to receive space qualification. However, the effect of gravity interferes with the dynamic behaviour of every structure on earth, while in space the influence of gravity is negligible (0g). E.g., on earth the array could not be suspended only at the root hinge – as it is planned for the space application – because the stiffness and strength of the root hinge are not high enough to support the weight appearing on earth. In order to obtain a similar behaviour of the structure during ground tests, the influence of gravity must be minimized using a gravity compensation system.

There are plenty of possibilities to simulate the 0g environment (ref. [11]): From testing on the International Space Station, via ballistic rockets and drop towers, to simple ground methods like mechanical suspensions, air cushions or buoyancy in water. Due to the size and mode of operation of deployable structures like rigid arrays, only the following methods are conceivable:

- water floats
- helium balloons
- air bearings
- passive or active suspension system by means of rails, trolleys, cables ...

A common problem with all gravity compensation systems is the interaction with the original structure. The results of the ground tests always consist of an additional, disturbing portion of the compensation system. The aim must be to find a suitable gravity suspension system which alters the behaviour on earth as little as possible.

1.4 Scope and Aims

The general aim of this diploma thesis was to find and investigate suitable gravity compensation system(s) for the deployment of the array described in section 1.2. Requirements on the gravity compensation system(s) were:

- small interaction with the original structure; ground deployment shall be comparable to deployment in space
- the gravity compensation system shall be not too complex in order to have simulations as simple as possible
- easy, fast and cheap to produce.

For the possible gravity compensation system(s), the deployment of an array similar to that described in section 1.2 had to be investigated. Simulations of the deployment process had to be developed in order to predict the behaviour in space and on the ground. The space and the ground deployment had to be similar. Furthermore, the deployment times of the experiments and the prediction had to be within a margin of 10%.

1.5 Outline of Diploma Thesis

Following this present, introductory chapter, Chapter 2 reviews current gravity compensation systems in general, and for deployable solar arrays in particular. At the end of this chapter it was concluded that a mechanical suspension system would be used.

Chapter 3 first describes a One-Rail Suspension System and the array used for experiments and simulations. Following this, a mathematical model of the deployment process was created. Two model parameters were experimentally determined. Subsequently, the first results of the simulation are presented and sensitivity studies were carried out. The results of the experimental deployment are displayed in the following section. With these results the simulation was compared and predictions for the SSTL array were made. Finally this gravity suspension system was evaluated. It was realized that this system restricts the behaviour of the array too much.

Chapter 4 presents a Four-Rail Suspension System. The simulation of Chapter 3 was adjusted to describe the new gravity compensation system. Initial results of the simulation showed that the mass of the moving parts of the suspension system had to be minimized. Furthermore, the friction had to be reduced in order to ensure full deployment. The friction problem was investigated in extensive tests. With the help of the simulation and the improvements on the friction problem, the Four-Rail Suspension System was designed. Following, tests on the deployment were carried out. The experimental results were compared with the simulations and discrepancies were explained.

Chapter 5 first gives a summary of the done work. Conclusions are drawn based on the results from the simulations and the experiments. Finally, an outlook on future work is written.

Chapter 2

Review of Gravity Compensation Systems

This chapter will give an overview about existing gravity compensation systems in general. The primary intention is to identify applicable systems for the solar array described in section 1.2.

2.1 Overview of Gravity Compensation Systems

2.1.1 Purpose of Gravity Compensation Systems

The main aim of ground-based gravity compensation systems is to create a near 0g environment as well as possible. Every system is characterized by the fact that it must provide anti-gravity forces (applied as body, surface forces or volume forces). An example of body force is the mechanical suspension of a test article by means of a string. Surface forces occur during buoyancy suspension. Volume forces are used in electromagnetic suspension systems [3].

By adding a compensation system to the test article its mechanical behaviour can change for the following reasons:

- The compensation system mass and moment of inertia. Due to connections to the test article the dynamic behaviour can change.
- Depending on the fastening of the test article to the gravity compensation system the kinematic behaviour of the test article can change. The compensation system may apply constraints which lead to the loss of degrees of freedom of motion.

The following sections will introduce different gravity compensation systems and will list their advantages and disadvantages, and typical fields of application.

2.1.2 Free Fall Methods

In this category one can count ballistic rockets, parabolic flights manoeuvres and drop towers.

Ballistic rockets can provide 0g for a duration of 5-15 minutes [1], but in most cases the available space for experiments is rather small. The high price and access available mostly only for military missions are big disadvantages.

Parabolic flights with aircrafts like the French 'Caravelle', ESA's 'Zero-G' A300 Airbus or the Russian IL-76 MDK can provide 0g for approximately 25 seconds [1]. The costs are affordable

and access to these facilities is not to difficult. However, 0g only exists for that short duration and before/afterwards there exist accelerations of more than 1g. Furthermore, for large structures there is not enough space available on the aircraft.

Drop towers are another example of free-fall testing. The Bremen (Germany)-based ZARM drop tower delivers 4.74 seconds of near 0g up to three times a day [1]. In Japan 0g can be achieved up to 11.7 seconds by dropping into a 490 meter deep mine shaft [12]. These facilities have the big disadvantage of high decelerations occurring after the experiment. The test space is only suitable for small experiment specimens.

2.1.3 Buoyancy Methods

Some aspects of 0g can be simulated in a neutral buoyancy tank filled with water. This method in particular is used for astronaut training, requiring scuba equipment. It is not suitable for most experiments because the test articles must be water-resistant and movement is highly restricted by drag forces. The duration of 0g experiments is theoretically unlimited. Practically, reactions between the water and the specimen or breathing problems of human beings restrict the maximum test time.

Water floats can also be included in this section. It must however be considered that the friction of floats on water is higher than sophisticated mechanical systems like trolleys or air cushions. Vertical displacements are not supported, so that only 2D motions are suitable for this type of compensation. The advantages of water floats are their simplicity, their low cost and the possible big dimensions of the test article.

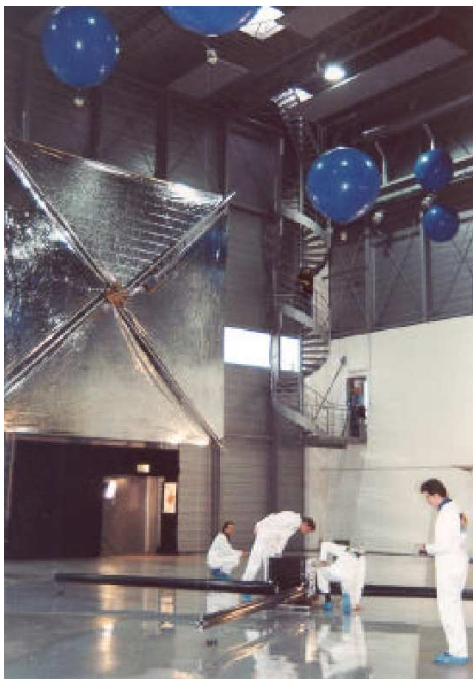

Figure 2.1: Boom Deployment supported by a Helium Balloon Gravity Compensation System (from [10])

Another example of buoyancy methods are helium balloons. Due to the small difference of mass between air and helium the buoyancy is not very high for small balloons. This implies that the specimen must be light or the balloon must be rather large. Big balloons are again not suitable for motions because of the high air drag.

In order to suspend the middle panel of the array described in section 1.2 (mass: 4.6 kg) a balloon with the diameter of 2 m would be necessary, which is not reasonable.

An application is shown in figure 2.1. The DLR performed a deployment of a light-weight solar sail structure in 1999. The structure consists of four CFRP (Carbon Fiber Reinforced Plastic) booms, each 14 m long, and a rectangular sail with 4 μm to 12 μm thick segments. The beams were highly endangered to collapse under their own weight. They were therefore suspended by helium filled balloons. The mass of the continuously deploying beam increases permanently and thus the suspension forces of the balloons need to be adjusted. This was achieved by remotely controlled pumps draining water from small tanks below the balloons. At mid-deployment four new balloons were attached to support the beams.

2.1.4 Pneumatic Methods

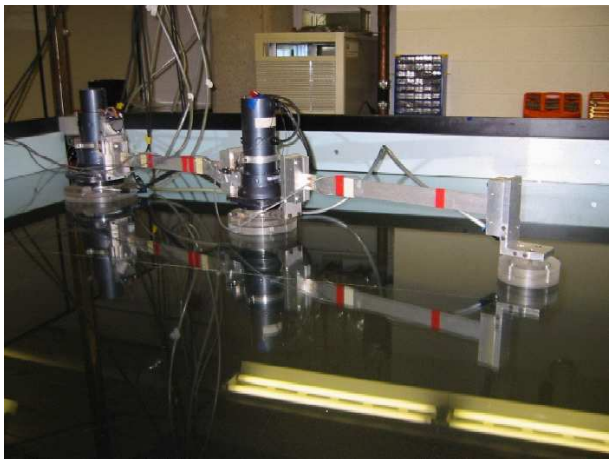

Figure 2.2: Planar Robots with Flexible Links (each with 2 strain gauges), Moving with Air Bearings on a Glass Table (from [5])

Pneumatic gravity compensation systems are air tables or air bearings. Both are characterized by 0g conditions only in horizontal directions. Movement in the vertical direction is not allowed. The suspension force is transmitted via a thin pressurized air film to the points of the specimen.

Air tables are mostly suitable for small-scale experiments. The pneumatic equipment is static which is a big advantage to air bearings. Air bearings are widely-used in the robotics field and allow large-scale applications because the table can have arbitrary dimensions. The very low friction is a big advantage, while the complexity, price and the necessary cleanliness are disadvantageous.

Fig. 2.2 shows WATFLEX (Waterloo Flexible Link Experimental Facility) of the University of Waterloo [2]. It is a modular test facility designed to emulate space-like conditions for flexible robotic manipulators. The entire system including the base and shoulder motors are supported on air bearings on a large horizontal glass surface in order to reduce friction and gravitational loadings.

2.1.5 Mechanical Methods

Mechanical methods are suspension systems with elements like cables, strings, pulleys, trolleys, rails or springs. In most cases gravity is compensated by more-or-less discrete forces which occur due to discrete suspension points. In some cases the specimen can also be suspended continuously, e.g. with an adhesive joint to a bar which is then suspended again at discrete points. The application of discrete forces on the test article changes the stress distribution and can thus be critical.

A feature of mechanical suspension systems is their simplicity. The basic elements (cable, pulley, ...) are cheap, available, simple to mount and reliable. These systems can host test structures of almost unlimited size even when motion exists. Especially because of this fact, in most cases they are the only option for large-scale experiments.

Disadvantages are the occurrence of friction, additional masses and mass moments of inertia and the unsatisfactory gravity compensation in vertical direction.

Because of the importance of mechanical methods in gravity compensation on earth the next section gives a more detailed description and some examples.

2.2 Mechanical Suspension Systems

2.2.1 1D Suspension

The simplest method is to use a cable which connects the specimen and the stand. It is characterized by restricted motion in the horizontal and especially in the vertical direction. Pendulum restoring forces disturb the horizontal motion and can only minimized by sufficiently long cables. Vertical motion under 0g conditions can only be achieved with very soft cables, which again

requires a high length. However, most test facilities cannot provide the appropriate heights.

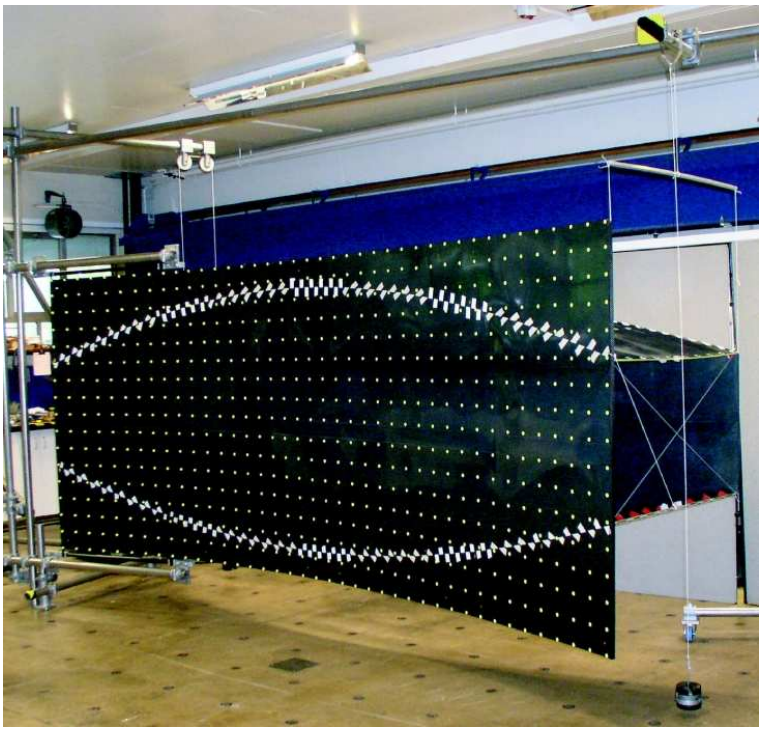

Figure 2.3: Passive Mechanical Gravity Compensation System used by the DSL: the structure of an antenna reflector is suspended by means of cables, pulleys and counterweights (on the right of figure).

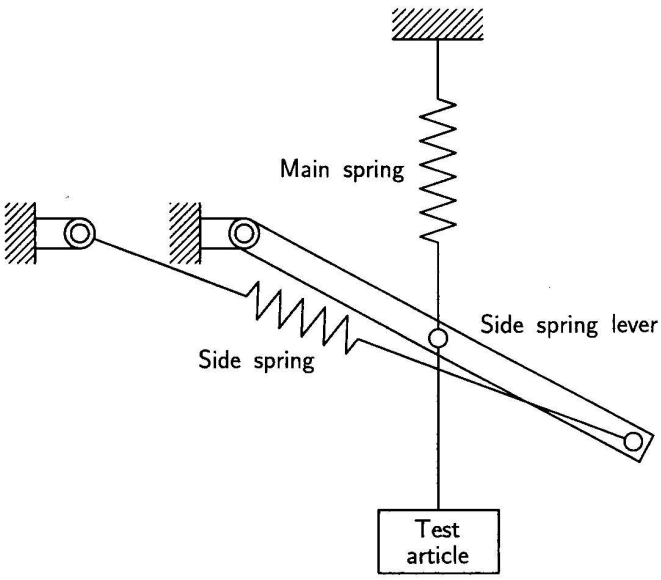

Figure 2.4: Passive ZSRM using a Side Spring Lever: the two springs are linked via a lever in such a way that the overall spring rate is near zero. (from [8])

The unsatisfactory behaviour in the vertical direction can be improved by means of a pulley and counterweight or a zero rate spring mechanism (ZSRM). The usage of counterweights provides anti-gravity forces at every vertical position and is thus equivalent to a cable with near-zero stiffness. The disadvantage of this suspension system is the doubling of the total system mass. By this, the dynamic behaviour of the total system changes and therefore is only suitable for quasi-static testing. An approach to reduce the influence of the added inertia is to control actively and correct the force in the suspension cable (see [9]). An example of counterweight suspension is shown in figure 2.3. Strings, pulleys and counterweights were used by the DSL for the deployment and folding of an antenna structure. This antenna is made of thin CFRP sheets which are connected by tape spring hinges. In the front of the figure the reflector can be seen to be a parabolic-shaped surface. Other structures in the back are used to support this front surface.

ZSRMs have a very soft behaviour at the setpoint. For small elongations of the spring from this setpoint the restoring force is almost constant. A possible simple mechanism is shown in fig. 2.4. A more advanced mechanism can be seen in fig. 2.5.

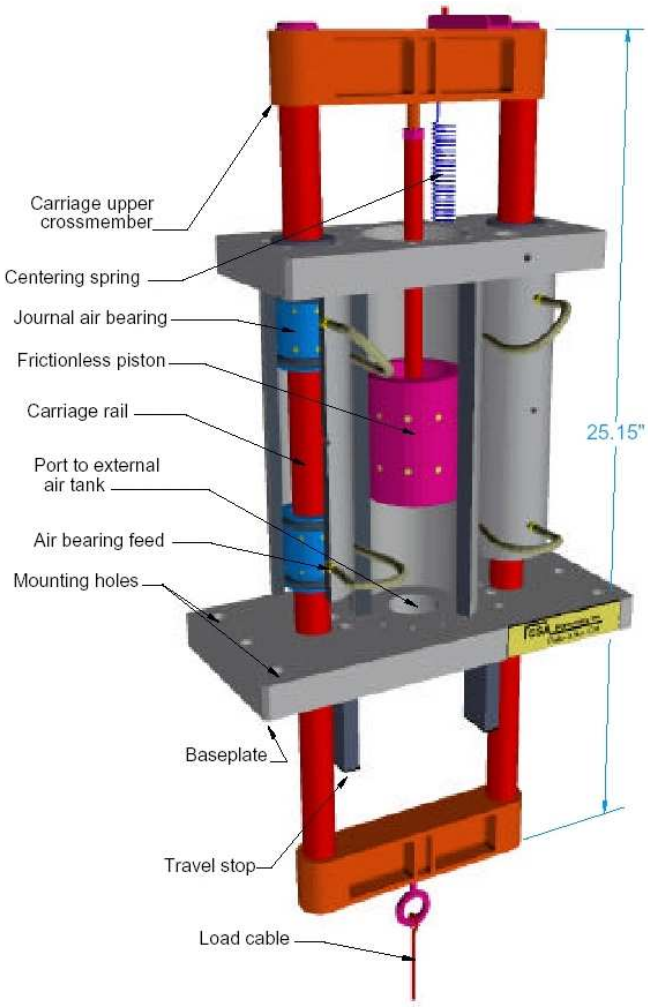

Figure 2.5: Zero-Gravity Suspension System Model 60350-0 from CSA Engineering, Inc. This device can support payloads up to 1550 kN and works virtually frictionless. The vertical suspension frequency is less than 0.2 Hz. (from [4])

2.2.2 2D/3D Suspension

Although the 1D suspension methods described above allow motion in all directions, they are mainly used to create a vertical 0g condition. They can however be combined with each other or with rail/trolley elements to ensure 2D/3D gravity compensation.

A 0g environment in horizontal directions can be achieved with the help of trolleys and rails. Friction between the two elements and the added mass of the moving elements are a disadvantage. However, the range of possible dimensions of test articles is almost unlimited.

With one rail and one trolley the horizontal motion is constrained to one degree of freedom. The usage of one rail that is able to rotate around a vertical axis and one trolley makes unconstrained motion in horizontal direction available. This is especially used for robot systems that work in a polar-coordinate system. For structures that can better be described in a x-y coordinate system two parallel and one transverse rail can be used. The trolley moves on the transverse rail, which in turn manoeuvres perpendicular to the trolley on the two other rails. In fig. 2.6 such a system is schematically drawn with the one exception that trolleys on the transverse rails are not shown.

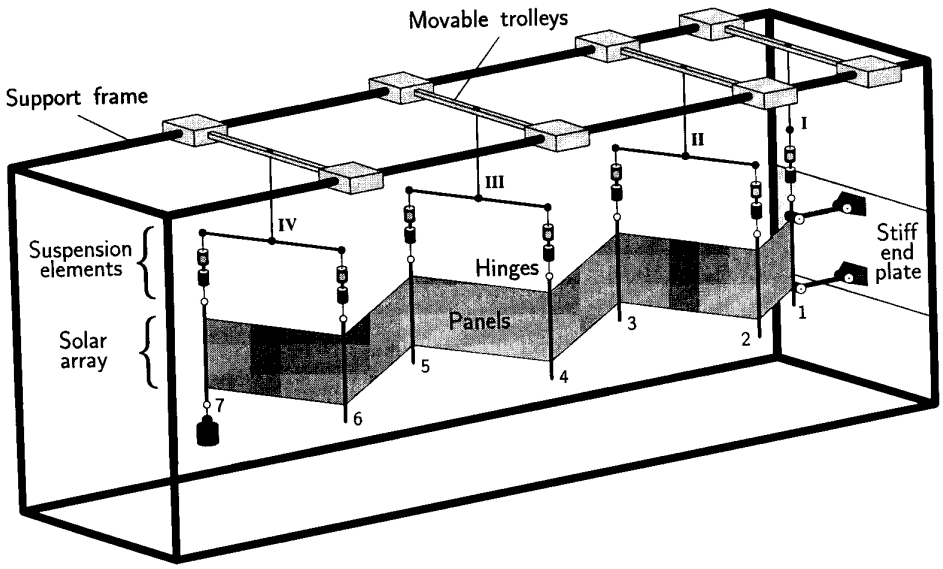

Figure 2.6: Schematic Diagram of a Solar Array Model and a Suspension System Utilizing Trolleys and Rails (from [6])

For further information and examples of mechanical suspension systems, A. Fischer's dissertation [6] about this topic is strongly recommended. In particular, the usage of actively controlled systems is described in detail.

2.3 Choice of suitable Gravity Compensation System(s)

Due to the size of the specimen (see section 1.2) and the fact that it must deploy, only mechanical suspension systems are feasible. Air bearings were excluded because of their price and scarce availability. Furthermore they introduce additional stiffness along the hinge line.

The array's deployment in space has only two degrees of freedom because motion in the direction of the hinge lines does not exist. The space deployment behaviour would be simulated very well

by means of a 2×2-rail system as shown in figure 2.7.

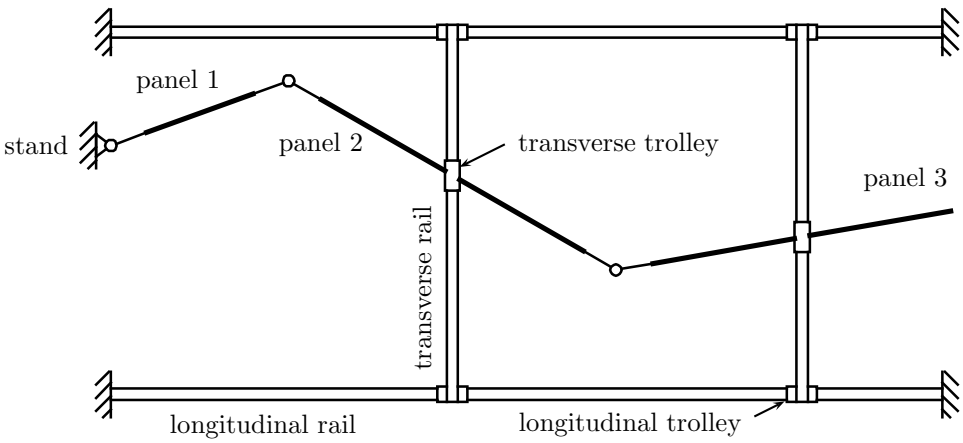

Figure 2.7: Schematic Diagram of a Possible Four-Rail Suspension System for the Rigid Array described in section 1.2; panel 1 is another term for yoke

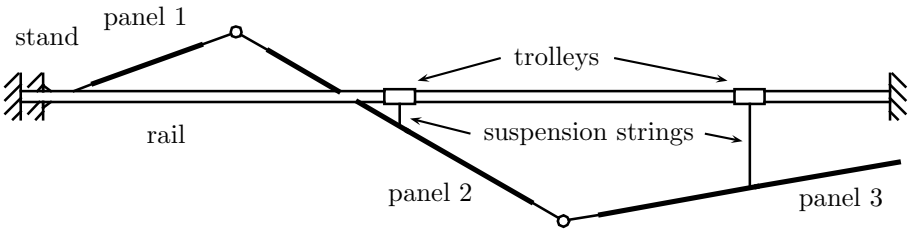

Figure 2.8: Schematic Diagram of a Possible One-Rail Suspension System for the Rigid Array described in Section 1.2

The mass of the moving parts of the four-rail suspension system (mass of 2 transverse rails and 6 trolleys) is much higher than the corresponding moving mass of a one-rail suspension system (see fig. 2.8). Although the one-rail suspension system has the disadvantage of strong pendulum restoring forces from the suspension strings, this system was chosen to be investigated first.

Chapter 3

One-Rail Suspension System

3.1 Description of One-Rail Suspension System

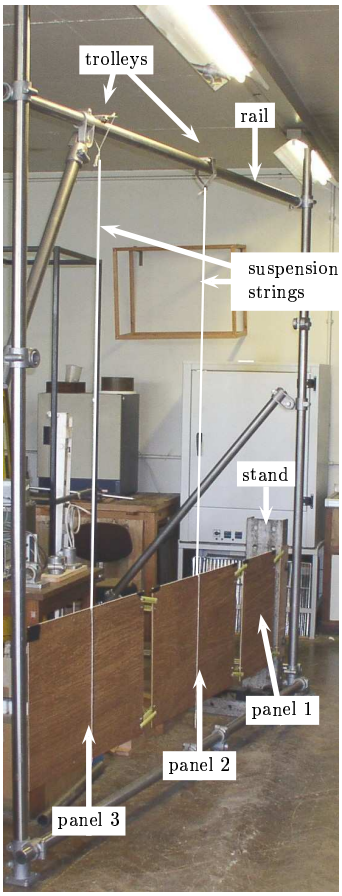

Figure 3.1: Test Set-up of the One-Rail Suspension System

In this chapter the usage and usefulness of a One-Rail Suspension System (ORSS) for the deployment of the rigid array of section 1.2 is investigated.

The ORSS consists of very few moving parts and is consequently very easy to simulate. Figure 3.1 shows the experimental set-up. The main part of this gravity compensation system is a horizontal stainless steel tube with a circular cross-section (outer diameter: 50 mm, wall thickness: 3mm) as the rail. This tube is mounted on scaffolding consisting of the same type of tubes.

Because of the smaller mass of panel 1[1] only the two large panels are suspended at the centre of their upper edge. A string connects this centre point of one panel with the corresponding trolley. The yoke is mounted via the root hinge to a stand.

For the deployment experiments a test array was used that has different dimensions and properties to the SSTL array. This fact was excepted, because the test array should only serve first experiences about the overall behaviour. The test array is described in section 3.2.

The deployment of the array was started by a release mechanism. In the folded configuration a horizontal stop holds any movement of the array back. This stop is connected to a lever, which is mounted with means of a joint to the scaffold. By rotating the lever the beam loses contact with the array and the deployment can begin.

The strings were fixed in such a way that their length could be adjusted. This was necessary to guarantee the exact horizontal orientation of the panels.

[1] The array actually only consists of two panels and one yoke. However, because of the fact that in later sections the yoke and panels were treated equally mathematically and numbered accordingly, the yoke is called panel 1.

3.2 Description of Test Array

3.2.1 Introduction

In order to get a feeling for the behaviour of the deployable panels a test array was created. The requirements were that the array should be

- easy and quick to build using existing materials
- cost-effective / cheap
- easy to handle
- robust
- similar to the planned "real" array in terms of dimensions and masses.

Based on the importance of the first two requirements, plywood was chosen for the panel material.

The whole 3-panel array set-up consists of the following parts:

- a stand which represents the connection of the array to a spacecraft
- the three panels
- the parts of the three hinge lines
  - tape springs
  - lower, upper and flat washers
  - bolts
  - nuts

In the following sections the individual parts are described.

3.2.2 The Stand and the Panels

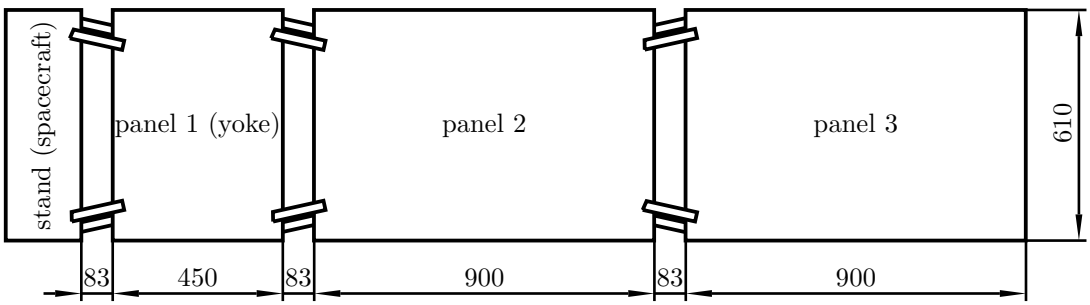

Figure 3.2: Side View of Test Array and Stand

As already mentioned the material of the three panels is plywood. The stand is made of the same material. Figure 3.2 shows a diagram of the stand and the three panels as they would be mounted. Table 3.1 summarizes the geometric and physical properties of the panels.

It must be mentioned that the dimensions and the mechanical properties of the test array are quite different to the ones of the SSTL array. However, for preliminary experiments and comparing with the simulation the test array is sufficient.

panel	length [mm]	width [mm]	thickness [mm]	mass [kg]	moment of inertia [kg m^2]
1	450	610	6	1.125	0.018984
2	900	610	6	2.250	0.151875
3	900	610	6	2.250	0.151875

Table 3.1: Properties of the Panels of the Test Array

Holes where drilled into the plywood for attaching the tape springs on the panels. Their positions can be seen in figure 3.3.

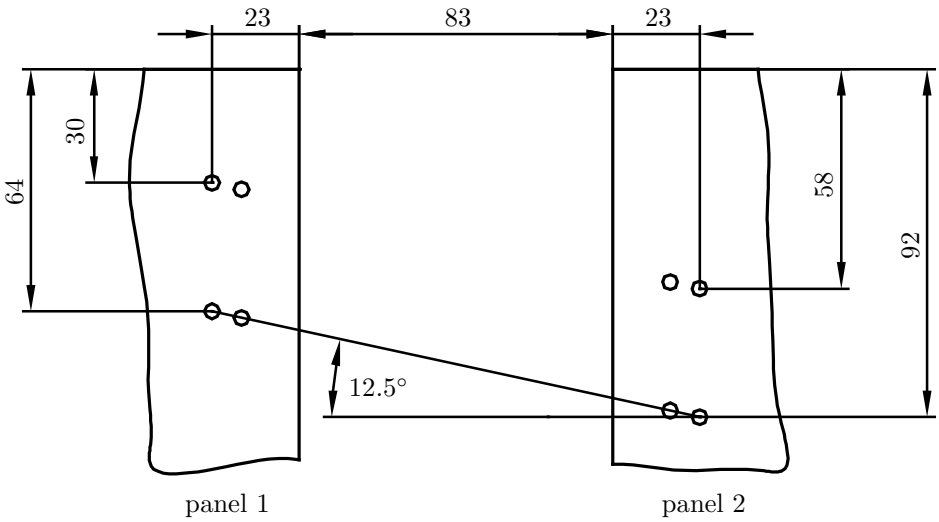

Figure 3.3: Positions of the Holes in Panel 1 and 2 for Fixing the Tape Springs

3.2.3 The Tape Springs

The tape springs are the main parts of the hinge lines. They ensure the connection of two panels, are responsible for the moment to deploy the panels and, when they are latched, guarantee the alignment of the panels in the working configuration. Photos of one tape spring can be seen in figure 3.5. The dimensions of a tape spring are shown in figure 3.4.

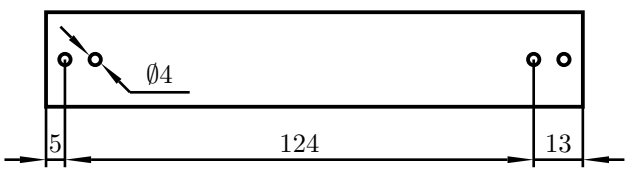

Figure 3.4: Dimensions of Tape Spring used for the Hinge Lines

The mass of one tape spring is $m_{\text{tape spring}} =$ 3.84 g. The overall length is $l_{\text{tape spring}} = 142$ mm while the distance between the two outer holes is 132 mm.

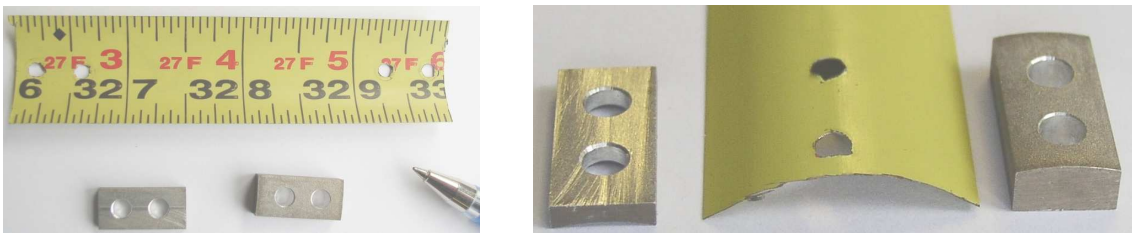

(a) top view (b) side view

Figure 3.5: Photos of one Tape Spring and the According Lower and Upper Washer

3.2.4 Tape Spring Fittings

The tape springs must be fastened to the panels. Figure 3.6 shows the section through such a connection. The upper and lower washers are made of aluminium. The surface of the washers

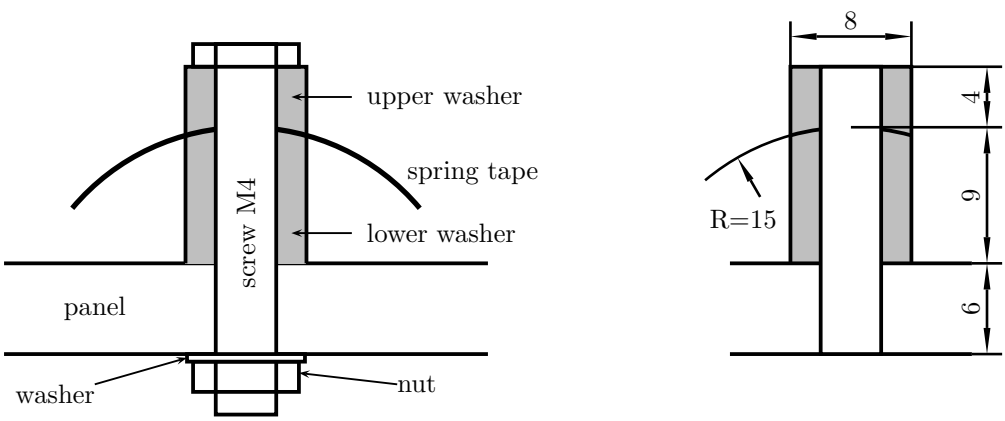

Figure 3.6: Section through the Parts of Tape Spring Fastening (left); Dimensions of Washers (right)

where the tape springs are fastened is curved. A photo of the used upper and lower washer may be viewed in fig. 3.5. The bolts, nuts and washers are typical metric industrial parts. The mass of the supports for one tape spring (2 upper and 2 lower washers, 4 screws, 4 washers, 4 nuts) is

$$m_{\text{supports of one tape spring}} = 11.825 \text{ g}.$$

The mass of the supports and tape springs in one hinge line is then

$$m_h = 62.66 \text{ g}. \tag{3.1}$$

3.3 Simulation of Array Deployment

3.3.1 Introduction and Notation

In order to receive the position and orientation of the three panels at every point of time during the deployment, the principle of virtual work for rigid structures was applied (internal virtual work was not considered). At a specific time all forces (loads, acceleration forces) and moments (spring and acceleration moments) are multiplied by infinitesimal small virtual displacements, which must

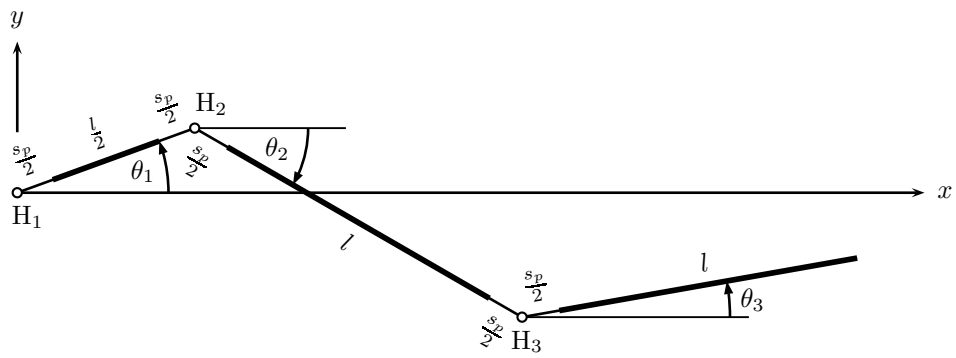

Figure 3.7: Arbitrary Constellation of the Panels

be kinematically compatible
($\delta W = \sum_i \boldsymbol{F}_i \circ \boldsymbol{\delta x}_i + \sum_j M_j \circ \delta\theta_j$).

In figure 3.7 the three panels are drawn in an arbitrary configuration. The angles of the panels are $\boldsymbol{\theta} = [\theta_1,\, \theta_2,\, \theta_3]^T$. The array has – if no hinge lines (H_1, H_2 or H_3) are latched – three degrees of freedom. Thus $\boldsymbol{\theta}$ can fully describe the system. The following variables were used to describe the geometry of the array:

l	length of the second and third panel, double length of panel 1
s_p	separation distance between two panels.

For this model it is assumed that the mass of all panels are equally distributed over their lengths. The mass of each hinge line was considered as a point mass at the position of H_1, H_2 or H_3, respectively. Hence, the body properties are those summarized in table 3.3.1.

panel	mass	mass moment of inertia
1	$m_1 + m_h$	$I_1 = \frac{l^2}{48}(m_1 + 3m_h)$
2	$m_2 + m_h$	$I_2 = \frac{l^2}{12}(m_2 + 3m_h)$
3	$m_3 + \frac{1}{2}m_h$	$I_3 = \frac{l^2}{24}(2m_3 + 3m_h)$

Table 3.2: Body Properties of the Panels

The equation of motion for the deployment will be risen in the next section. However, as already mentioned, the system description changes if tape springs get latched. If, e.g., the first hinge line gets locked there are only two degrees of freedom left and the equation of motion differs from the original equation. Another change in the deployment behaviour results from kinematic restrictions. E.g. panel 2 is not allowed to penetrate the satellite, which means that the x-value of H_3 must be greater than zero. Both, the latching conditions and the kinematic restrictions can be handled by imposing constraints on the basic equation. All the problems of applying constraints will be explained in section 3.3.3.

Whenever the type of constraint changes, e.g. preventing penetration, additional forces or moments are applied by the constraint. These loads always appear as impacts (linear or angular). Because of their importance only the impacts due to latching of the hinge lines are considered. The change of the angular velocities after any latching is investigated in section 3.3.4.

The initial conditions of the deployment can be changed by applying different angular velocities. This adjustment is described in section 3.3.5.

Finally, in order to solve the equation of motion and handle the different constraints and impact equations, a complex program was necessary. It is summarized in section 3.3.6.

3.3.2 Basic Equation of Motion

In this section no restrictions due to latching or penetration are considered. The system includes the panels and hinge line supports, the springs in the joints and the suspension system. In this, the total virtual work consists of components resulting from

1. the moments in the hinge lines
2. the linear inertia of the panels and the hinge line parts
3. the angular inertia of the panels and the hinge line parts
4. the restoring forces in the suspension strings
5. the linear inertia of the trolleys
6. the friction between the trolleys and the rail.

The total (external) virtual work due to virtual displacements must be zero.

The virtual work is calculated using virtual displacements. In this case it means an infinitesimal small change of the angles of the panels θ_i. Three possible independent virtual variations are:

$$\delta\boldsymbol{\theta_1} = [1,0,0]^T \qquad \text{virtual displacement due to } \delta\theta_1 = 1$$
$$\delta\boldsymbol{\theta_2} = [0,1,0]^T \qquad \text{virtual displacement due to } \delta\theta_2 = 1$$
$$\delta\boldsymbol{\theta_3} = [0,0,1]^T \qquad \text{virtual displacement due to } \delta\theta_3 = 1$$

The matrix of the three fundamental virtual displacements is then

$$\begin{aligned}\boldsymbol{\delta\theta} = \delta(\boldsymbol{\theta}) = \frac{\partial\boldsymbol{\theta}}{\partial\boldsymbol{\theta}} &= [\delta\boldsymbol{\theta_1}, \delta\boldsymbol{\theta_2}, \delta\boldsymbol{\theta_3}] \\ &= \boldsymbol{E}\end{aligned} \tag{3.2}$$

with $(\delta\theta)_{ij}$ being the virtual displacement of θ_i due to a virtual change of θ_j.

Virtual Work due to Bending of the Tape Springs $\delta\boldsymbol{W_h}$

The moments in the hinge lines shall be $\boldsymbol{M_h} = [M_{h1}, M_{h2}, M_{h3}]^T$. The moments are dependent on the angles between two adjacent panels $\boldsymbol{\Delta\theta_h} = [\theta_1, \theta_2 - \theta_1, \theta_3 - \theta_2]^T$:

$$(M_h)_i = f_{M_h}((\Delta\theta_h)_i) = \begin{cases} -M_{h0} & \text{if } (\Delta\theta_h)_i < 0 \\ 0 & \text{if } (\Delta\theta_h)_i = 0 \\ M_{h0} & \text{if } (\Delta\theta_h)_i > 0 \end{cases} \tag{3.3}$$

The virtual angular displacements of the spring tapes are

$$\begin{aligned}\delta(\boldsymbol{\Delta\theta_h}) = \frac{\partial}{\partial\boldsymbol{\theta}}(\boldsymbol{\Delta\theta_h})\delta(\boldsymbol{\theta}) &= \frac{\partial}{\partial\boldsymbol{\theta}}\left(\begin{bmatrix} 1 & 0 & 0 \\ -1 & 1 & 0 \\ 0 & -1 & 1 \end{bmatrix}\boldsymbol{\theta}\right)\boldsymbol{E} = \begin{bmatrix} 1 & 0 & 0 \\ -1 & 1 & 0 \\ 0 & -1 & 1 \end{bmatrix} \\ &= \boldsymbol{C_1}\end{aligned} \tag{3.4}$$

The virtual work of the tape springs due to the virtual change $\delta\phi_j = 1$ is (written in Einstein's summation convention)

$$\begin{aligned}(\delta W_h)_j &= -(M_h)_i(\delta\Delta\theta_h)_{ij} = -(\delta\Delta\theta_h)_{ji}(M_h)_i \\ &= -(C_1)_{ki}(M_h)_i,\end{aligned}$$

which can be written again in matrix style:

$$\delta\boldsymbol{W_h} = -\boldsymbol{C_1}^T\,\boldsymbol{M_h} \tag{3.5}$$

Virtual Work due to the Panels' Translation (Linear Inertia) $\delta \boldsymbol{W}_{\ddot{\boldsymbol{x}}}$

The three panels have 6 translational degrees of freedom in total as each panel can move in the x- and y-direction but has no degree of freedom in the z-direction. The position vector of the centre of each panel is defined by

$$
\begin{aligned}
\boldsymbol{x} &= \begin{bmatrix} x_1 \\ x_2 \\ x_3 \\ x_4 \\ x_5 \\ x_6 \end{bmatrix} = \begin{bmatrix} x_{\text{panel 1}} \\ y_{\text{panel 1}} \\ x_{\text{panel 2}} \\ y_{\text{panel 2}} \\ x_{\text{panel 3}} \\ y_{\text{panel 3}} \end{bmatrix} \\
&= \begin{bmatrix} l/4 + s_p/2 & 0 & 0 & 0 & 0 & 0 \\ 0 & l/4 + s_p/2 & 0 & 0 & 0 & 0 \\ l/2 + s_p & 0 & l/2 + s_p/2 & 0 & 0 & 0 \\ 0 & l/2 + s_p & 0 & l/2 + s_p/2 & 0 & 0 \\ l/2 + s_p & 0 & l + s_p & 0 & l/2 + s_p/2 & 0 \\ 0 & l/2 + s_p & 0 & l + s_p & 0 & l/2 + s_p/2 \end{bmatrix} \begin{bmatrix} \cos\theta_1 \\ \sin\theta_1 \\ \cos\theta_2 \\ \sin\theta_2 \\ \cos\theta_3 \\ \sin\theta_3 \end{bmatrix} \\
&= \boldsymbol{C_2}\, \boldsymbol{c_3}
\end{aligned} \tag{3.6}
$$

The velocities of the centre points of the panel are

$$
\begin{aligned}
\dot{\boldsymbol{x}} &= \frac{\partial}{\partial t}\boldsymbol{x} = \boldsymbol{C_2}\frac{\partial}{\partial t}\boldsymbol{c_3} = \boldsymbol{C_2}\frac{\partial}{\partial \boldsymbol{\theta}}\boldsymbol{c_3}\frac{\partial \boldsymbol{\theta}}{\partial t} \\
&= \boldsymbol{C_2} \begin{bmatrix} -\sin\theta_1 & 0 & 0 \\ \cos\theta_1 & 0 & 0 \\ 0 & -\sin\theta_2 & 0 \\ 0 & \cos\theta_2 & 0 \\ 0 & 0 & -\sin\theta_3 \\ 0 & 0 & \cos\theta_3 \end{bmatrix} \begin{bmatrix} \dot{\theta}_1 \\ \dot{\theta}_2 \\ \dot{\theta}_3 \end{bmatrix} \\
&= \boldsymbol{C_4}\, \dot{\boldsymbol{\theta}}
\end{aligned} \tag{3.7}
$$

The accelerations of the centre points of the panels are

$$
\begin{aligned}
\ddot{\boldsymbol{x}} &= \frac{\partial}{\partial t}\dot{\boldsymbol{x}} = \frac{\partial}{\partial t}(\boldsymbol{C_4})\dot{\boldsymbol{\theta}} + \boldsymbol{C_4}\, \ddot{\boldsymbol{\theta}} \\
&= -\boldsymbol{C_2} \begin{bmatrix} \cos\theta_1\dot{\theta}_1^2 \\ \sin\theta_1\dot{\theta}_1^2 \\ \cos\theta_2\dot{\theta}_2^2 \\ \sin\theta_2\dot{\theta}_2^2 \\ \cos\theta_3\dot{\theta}_3^2 \\ \sin\theta_3\dot{\theta}_3^2 \end{bmatrix} + \boldsymbol{C_4}\, \ddot{\boldsymbol{\theta}} \\
&= \boldsymbol{c_5} + \boldsymbol{C_4}\, \ddot{\boldsymbol{\theta}}
\end{aligned} \tag{3.8}
$$

The inertia force is the negative product of mass and acceleration.

$$
\begin{aligned}
\boldsymbol{F}_{\ddot{\boldsymbol{x}}} &= -\begin{bmatrix} m_1 + m_h & 0 & 0 & 0 & 0 & 0 \\ 0 & m_1 + m_h & 0 & 0 & 0 & 0 \\ 0 & 0 & m_2 + m_h & 0 & 0 & 0 \\ 0 & 0 & 0 & m_2 + m_h & 0 & 0 \\ 0 & 0 & 0 & 0 & m_3 + m_h/2 & 0 \\ 0 & 0 & 0 & 0 & 0 & m_3 + m_h/2 \end{bmatrix} \ddot{\boldsymbol{x}} \\
&= -\boldsymbol{m_p}\, \ddot{\boldsymbol{x}}
\end{aligned} \tag{3.9}
$$

The linear virtual displacement of the panels' centre is

$$\begin{aligned}\delta(\boldsymbol{x}) &= \frac{\partial \boldsymbol{x}}{\partial \boldsymbol{\theta}}\delta(\boldsymbol{\theta}) = \frac{\partial}{\partial \boldsymbol{\theta}}(\boldsymbol{C_2}\,\boldsymbol{c_3})\,\boldsymbol{E} = \boldsymbol{C_2}\,\frac{\partial}{\partial \boldsymbol{\theta}}(\boldsymbol{c_3}) \\ &= \boldsymbol{C_4} \end{aligned} \tag{3.10}$$

The virtual work of the panels' linear inertia $(\delta W_{\ddot{x}})_j$ due to the virtual change $\delta\theta_j = 1$ is

$$\begin{aligned}(\delta W_{\ddot{x}})_j &= (F_{\ddot{x}})_i\,\delta x_{ij} \\ &= \delta x_{ji}\,(F_{\ddot{x}})_i\end{aligned}$$

or written in matrix style, using (3.10), (3.9) and (3.8):

$$\begin{aligned}\delta \boldsymbol{W_{\ddot{x}}} &= [\delta(\boldsymbol{x})]^T\,\boldsymbol{F_{\ddot{x}}} \\ &= -\boldsymbol{C_4}^T\,\boldsymbol{m_p}\,(\boldsymbol{c_5} + \boldsymbol{C_4}\,\ddot{\boldsymbol{\theta}}) \\ &= -\boldsymbol{c_6} - \boldsymbol{C_7}\,\ddot{\boldsymbol{\theta}}\end{aligned} \tag{3.11}$$

Virtual Work due to the Panels' Rotation (Angular Inertia) $\delta \boldsymbol{W_{\ddot{\theta}}}$

The three panels have three rotational degrees of freedom in total. The vector of the angular position of the panels is $\boldsymbol{\theta}$. The acceleration of the panels is $\ddot{\boldsymbol{\theta}}$.

The inertia torque is the negative product of the static moment of inertia and the angular acceleration. The mass moments of inertia can be found in table 3.3.1.

$$\begin{aligned}\boldsymbol{M_{\ddot{\theta}}} &= -\begin{bmatrix} I_1 & 0 & 0 \\ 0 & I_2 & 0 \\ 0 & 0 & I_3 \end{bmatrix}\begin{bmatrix}\ddot{\theta}_1 \\ \ddot{\theta}_2 \\ \ddot{\theta}_3\end{bmatrix} \\ &= -\boldsymbol{I_p}\,\ddot{\boldsymbol{\theta}}\end{aligned} \tag{3.12}$$

The virtual angular displacement of the panels is

$$\delta(\boldsymbol{\theta}) = \boldsymbol{E}$$

The virtual work of the panel j's angular inertia $(\delta W_{\ddot{\theta}})_j$ due to the virtual change $\delta\theta_j = 1$ is

$$\begin{aligned}(\delta W_{\ddot{\theta}})_j &= (M_{\ddot{\theta}})_i\,\delta\theta_{ij} \\ &= \delta\theta_{ji}\,(M_{\ddot{\theta}})_i\end{aligned}$$

or written in matrix style

$$\delta \boldsymbol{W_{\ddot{\theta}}} = -\boldsymbol{I_p}\,\ddot{\boldsymbol{\theta}} \tag{3.13}$$

Virtual Work due to Suspension Forces $\delta \boldsymbol{W_{susp}}$

So far, the panel's centre moved only in the $x - y$ plane, but now the suspension system shall be considered. The suspension strings at the panels 2 and 3 must carry the weight of all panels and all occurring acceleration forces. If a panel has a small excursion from the x-axis (see figure 3.8) a force component in y-direction is generated (see figure 3.9). Virtual displacements of the centres of the panels and these restoring forces (in y-direction) cause the virtual work δW_{susp}.

In figure 3.9 the two components of the suspension forces can be seen. Components in x-direction were not taken into consideration because the position of the trolley is exactly above the point of suspension on the panel. The inertia of the trolley and the friction between trolley and rail were neglected at this point of calculation which would cause an x-offset between the panel centre and

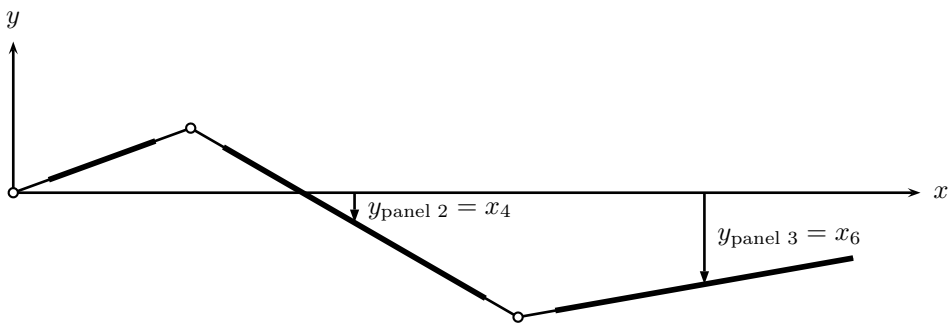

Figure 3.8: Excursion of the Suspension Points of the Panels 2 and 3

the trolley. Experiments showed that the x-offset between the trolley and the point of suspension on the panel was always very small compared to the length of the suspension string l_s.

The z-components $(F_{susp,z})_i$ equalize the weight of the panels and the acceleration forces in the z-direction. Thus the virtual work due to a virtual displacement in this direction would be zero and need not be calculated.

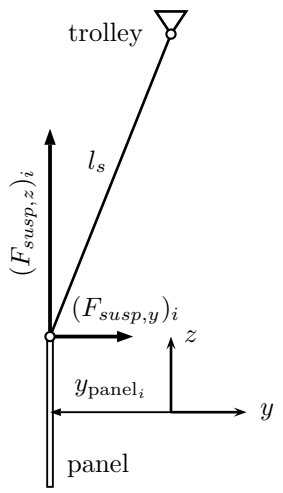

Figure 3.9: Forces in the Suspension String due to Excursion of the Panel's Centre

The restoring forces $(F_{susp,y})_i$ can be calculated if the vertical force component $(F_{susp,z})_i$ is known. Because the first panel is not supported, the two suspension strings must carry the weight of that panel too. The vertical forces in the strings can be estimated as followed, see also figure 3.10.

Forces in each direction (including z) and moments around the y-axis can be transmitted through the hinge lines. The moments around the y-axis appear due to a small rotation of the panels around the y-axis. In addition to neglecting the very small masses of the hinge line parts, the following assumption was made. If panel 1 rotates around the y-axis with ζ then panel 2 and 3 rotate with $-\zeta$ and ζ respectively. Thus we can assume that in the first hinge line the moment is only half of the moment in the two other hinge lines. Figure 3.10 shows the corresponding forces F_H and moments M. The weight and the acceleration forces in z-direction are $(m_i + \ddot{z}_i)g$.

After elimination of the forces and moments in the hinge lines one obtains:

$$\boldsymbol{F_{susp,z}} = \begin{bmatrix} (F_{susp,z})_2 \\ (F_{susp,z})_3 \end{bmatrix} = \begin{bmatrix} m_2 + 4/9\, m_1 \\ m_3 - 1/9\, m_1 \end{bmatrix} g + \begin{bmatrix} 4/9\, m_1 & m_2 & 0 \\ -1/9\, m_1 & 0 & m_3 \end{bmatrix} \begin{bmatrix} \ddot{z}_1 \\ \ddot{z}_2 \\ \ddot{z}_3 \end{bmatrix} \tag{3.14}$$

It can be seen that the suspension strings must carry additional force to the weight and D'Alembert force of panel 2 or 3, respectively. The suspension string of panel 2 additionally carries 4/9 of panel 1's weight and z-acceleration force. Suspension string 3 is even slightly relieved. The rest of the weight and D'Alembert force in the z-direction of panel 1 is carried by the hinge line between satellite and that panel. The suspension forces in z-direction thus are also dependent on the acceleration of the panels in the same direction. In the next lines, $\ddot{z}_i$ in (3.14) is replaced with the basic variables θ and their derivatives.

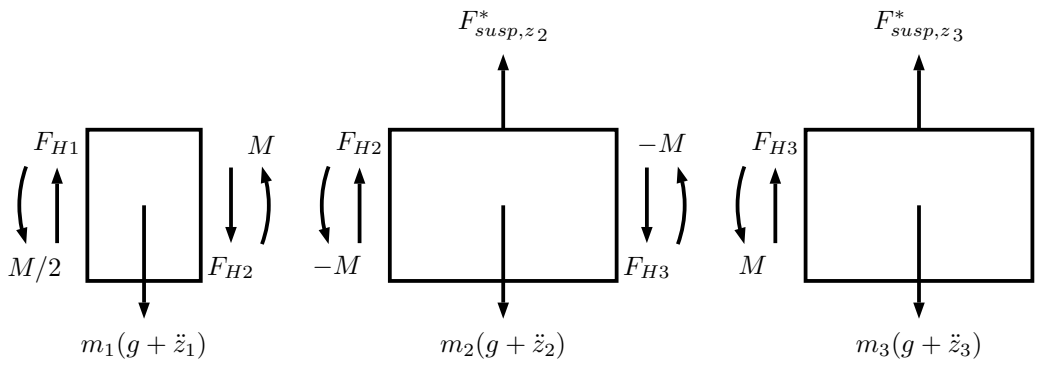

Figure 3.10: Forces and Moments for the Determination of the Suspension Forces

The z-coordinate of the panel's centre and its second derivative w.r.t. time are

$$
\begin{aligned}
z_i &= l_s - \sqrt{l_s^2 - y_i^2} \\
\ddot{z}_i &= \frac{l_s^2}{(l_s^2 - y_i^2)^{3/2}}\,\dot{y}_i^2 + \frac{y_i}{(l_s^2 - y_i^2)^{1/2}}\,\ddot{y}_i
\end{aligned}
$$

with y_i being the y-coordinate of panel i. The accelerations of z can be written as a vector.

$$
\ddot{\boldsymbol{z}} = \boldsymbol{c_9} + \boldsymbol{C_{10}}\,\ddot{\boldsymbol{y}}
$$

As the vector of the y-coordinates of the three panels is

$$
\begin{aligned}
\boldsymbol{y} &= \begin{bmatrix} x_2 \\ x_4 \\ x_6 \end{bmatrix} = \begin{bmatrix} 0 & 1 & 0 & 0 & 0 & 0 \\ 0 & 0 & 0 & 1 & 0 & 0 \\ 0 & 0 & 0 & 0 & 0 & 1 \end{bmatrix} \boldsymbol{x} \\
&= \boldsymbol{C_8}\,\boldsymbol{x}
\end{aligned}
$$

we can substitute the second derivative of $\boldsymbol{y}$ in the previous equation:

$$
\begin{aligned}
\ddot{\boldsymbol{z}} &= \boldsymbol{c_9} + \boldsymbol{C_{10}}\,\boldsymbol{C_8}\,\boldsymbol{c_5} + \boldsymbol{C_{10}}\,\boldsymbol{C_8}\,\boldsymbol{C_4}\,\ddot{\boldsymbol{\theta}} \\
&= \boldsymbol{c_{11}} + \boldsymbol{C_{12}}\,\ddot{\boldsymbol{\theta}}
\end{aligned}
$$

Using this equation in (3.14) we get

$$
\begin{aligned}
\boldsymbol{F_{susp,z}} &= \begin{bmatrix} m_2 + 4/9\,m_1 \\ m_3 - 1/9\,m_1 \end{bmatrix} g + \begin{bmatrix} 4/9\,m_1 & m_2 & 0 \\ -1/9\,m_1 & 0 & m_3 \end{bmatrix} (\boldsymbol{c_{11}} + \boldsymbol{C_{12}}\,\ddot{\boldsymbol{\theta}}) \\
&= \boldsymbol{c_{13}} + \boldsymbol{C_{14}}\,\ddot{\boldsymbol{\theta}}
\end{aligned}
\tag{3.15}
$$

The restoring forces of the suspension are

$$
\begin{aligned}
\boldsymbol{F_{susp,y}} &= \begin{bmatrix} -x_4/\sqrt{l_s^2 - x_4^2} & 0 \\ 0 & -x_6/\sqrt{l_s^2 - x_6^2} \end{bmatrix} \boldsymbol{F_{susp,z}} \\
&= \boldsymbol{C_{15}}\,\boldsymbol{F_{susp,z}}
\end{aligned}
$$

The corresponding locating vector can be written as

$$
\begin{aligned}
\boldsymbol{x_{susp}} &= \begin{bmatrix} x_4 \\ x_6 \end{bmatrix} = \begin{bmatrix} 0 & 0 & 0 & 1 & 0 & 0 \\ 0 & 0 & 0 & 0 & 0 & 1 \end{bmatrix} \boldsymbol{x} \\
&= \boldsymbol{C_{16}}\,\boldsymbol{x}
\end{aligned}
$$

and hence the virtual displacement of the restoring forces is

$$\delta(\boldsymbol{x_{susp}}) = \boldsymbol{C_{16}}\,\delta(\boldsymbol{x}) = \boldsymbol{C_{16}}\,\boldsymbol{C_4}.$$

Finally the virtual work $\delta\boldsymbol{W_{susp}}$ can be calculated by multiplying the restoring forces with the corresponding virtual displacements.

$$\begin{aligned}
(\delta W_{susp})_j &= (F_{susp,y})_i\ (\delta x_{susp})_{ij} \\
&= (\delta x_{susp})_{ji}\ (F_{susp,y})_i && \text{or in matrix notation} \\
\delta\boldsymbol{W_{susp}} &= [\delta(\boldsymbol{x_{susp}})]^T\boldsymbol{F_{susp,y}} \\
&= \boldsymbol{C_4}^T\boldsymbol{C_{16}}^T\boldsymbol{C_{15}}\,(\boldsymbol{c_{13}} + \boldsymbol{C_{14}}\,\ddot{\boldsymbol{\theta}}) \\
&= \boldsymbol{c_{17}} + \boldsymbol{C_{18}}\,\ddot{\boldsymbol{\theta}}
\end{aligned} \tag{3.16}$$

Virtual Work due to the Inertia of the Trolley $\delta\boldsymbol{W_t}$

A second virtual work in the suspension system results from the mass of the trolley and its acceleration along the rail. The D'Alembert force is

$$\boldsymbol{F_{\ddot{x}_t}} = -m_t \begin{bmatrix} \ddot{x}_{t1} \\ \ddot{x}_{t2} \end{bmatrix}. \tag{3.17}$$

The position of the trolleys are $(x_{t1}; 0)$ and $(x_{t2}; 0)$. To simplify the simulation it was assumed that the trolleys always have the same x-position as the centres of the panels, hence

$$\begin{aligned}
\boldsymbol{x_t} &= \begin{bmatrix} x_{t1} \\ x_{t2} \end{bmatrix} = \begin{bmatrix} x_3 \\ x_5 \end{bmatrix} = \begin{bmatrix} 0 & 0 & 1 & 0 & 0 & 0 \\ 0 & 0 & 0 & 0 & 1 & 0 \end{bmatrix} \boldsymbol{x} \\
&= \boldsymbol{C_{19}}\,\boldsymbol{x} \\
\ddot{\boldsymbol{x}}_{\boldsymbol{t}} &= \boldsymbol{C_{19}}\,\ddot{\boldsymbol{x}} \\
&= \boldsymbol{C_{19}}\,(\boldsymbol{c_5} + \boldsymbol{C_4}\,\ddot{\boldsymbol{\theta}})
\end{aligned}$$

The virtual displacement of the trolleys is

$$\begin{aligned}
\delta(\boldsymbol{x_t}) &= \boldsymbol{C_{19}}\,\delta(\boldsymbol{x}) \\
&= \boldsymbol{C_{19}}\,\boldsymbol{C_4}
\end{aligned}$$

The virtual work is calculated as follows:

$$\begin{aligned}
(\delta W_t)_j &= (F_{\ddot{x}_t})_i\,(\delta x_t)_{ij} = (\delta x_t)_{ji}\,(F_{\ddot{x}_t})_i && \text{or in matrix notation} \\
\delta\boldsymbol{W_t} &= [\delta\boldsymbol{x_t}]^T\boldsymbol{F_{\ddot{x}_t}} \\
&= -m_t\,\boldsymbol{C_4}^T\boldsymbol{C_{19}}^T\boldsymbol{C_{19}}\,(\boldsymbol{c_5} + \boldsymbol{C_4}\,\ddot{\boldsymbol{\theta}}) \\
&= -m_t(\boldsymbol{c_{20}} + \boldsymbol{C_{21}}\,\ddot{\boldsymbol{\theta}})
\end{aligned} \tag{3.18}$$

Virtual Work due to Friction between Trolley and Rail $\delta\boldsymbol{W_\mu}$

δW_μ is the last virtual work term which shall be considered in this section for the suspension system. The contact between trolley and the tubular rail is not frictionless. Figure 3.11 shows one trolley and the rail. The trolley has an angular displacement which can be caused by an excursion in y-direction of the belonging panel.

The force of friction shall be direct proportional to the normal force. The normal forces are composed of a small portion from the weight of the trolleys $(m_t\,g)$ and a large portion from

the weight and the accelerations of the panels $(F_{susp})_i$. The z-component of the forces in the suspension strings were already calculated, refer to equation (3.15):

$$\boldsymbol{F_{susp,z}} = \boldsymbol{c_{13}} + \boldsymbol{C_{14}}\,\ddot{\boldsymbol{\theta}}.$$

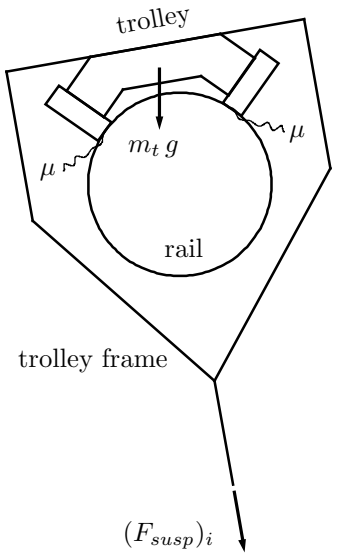

Figure 3.11: The Trolley and the Rail

From this, the suspension forces are

$$\begin{aligned}\boldsymbol{F_{susp}} &= \begin{bmatrix} l_s/\sqrt{l_s^2 - x_4^2} & 0 \\ 0 & l_s/\sqrt{l_s^2 - x_6^2}\end{bmatrix} \boldsymbol{F_{susp,z}} \\ &= \boldsymbol{c_{22}} + \boldsymbol{C_{23}}\,\ddot{\boldsymbol{\theta}}\end{aligned}$$

The normal forces at the two trolleys are summarized in the normal force vector

$$\begin{aligned}\boldsymbol{F_n} &= m_t\,g \begin{bmatrix} l_s/\sqrt{l_s^2 - x_4^2} \\ l_s/\sqrt{l_s^2 - x_6^2}\end{bmatrix} + \boldsymbol{F_{susp}} \\ &= \boldsymbol{c_{24}} + \boldsymbol{C_{23}}\,\ddot{\boldsymbol{\theta}}.\end{aligned}$$

The forces of friction $(F_\mu)_i$ are directly proportional to the corresponding normal forces

$$\begin{aligned}\boldsymbol{F_\mu} &= \boldsymbol{\mu}\,\boldsymbol{F_n} \\ &= \boldsymbol{\mu}\,(\boldsymbol{c_{24}} + \boldsymbol{C_{23}}\,\ddot{\boldsymbol{\theta}}).\end{aligned} \tag{3.19}$$

with $\boldsymbol{\mu}$ being the coefficient matrix of friction. It is defined as

$$\boldsymbol{\mu} = \begin{bmatrix} -\mathrm{sign}(\dot{x}_3) & 0 \\ 0 & -\mathrm{sign}(\dot{x}_5)\end{bmatrix} \mu. \tag{3.20}$$

μ is the (scalar) kinetic, rolling coefficient of friction. The coefficient matrix of friction guarantees that the direction of the force of friction is opposite to the trolley's velocity, or in case of no motion that the friction force is zero.

The virtual displacement of the trolleys has already been calculated:

$$\delta(\boldsymbol{x_t}) = \boldsymbol{C_{19}}\,\boldsymbol{C_4}.$$

The virtual work is the product of the forces of friction (in x-direction) and the corresponding virtual displacements (in opposite direction). Hence, this virtual work is always non-positive.

$$(\delta W_\mu)_j = (F_\mu)_i\,(\delta x_t)_{ij} = (\delta x_t)_{ji}\,(F_\mu)_i \qquad \text{or in matrix notation}$$

$$\begin{aligned}\delta\boldsymbol{W_\mu} &= [\delta(\boldsymbol{x_t})]^T\,\boldsymbol{F_\mu} \\ &= \boldsymbol{C_4}^T\boldsymbol{C_{19}}^T\mu \begin{bmatrix} -\mathrm{sign}(\dot{x}_3) & 0 \\ 0 & -\mathrm{sign}(\dot{x}_5)\end{bmatrix} (\boldsymbol{c_{24}} + \boldsymbol{C_{23}}\,\ddot{\boldsymbol{\theta}}) \\ &= \mu\,\boldsymbol{c_{25}} + \mu\,\boldsymbol{C_{26}}\,\ddot{\boldsymbol{\theta}}\end{aligned} \tag{3.21}$$

Total Virtual Work

The principle of virtual work for rigid-body systems states that the sum of all virtual works must be zero, hence

$$\begin{aligned}\delta\boldsymbol{W_{tot}} &= 0 \\ &= \delta\boldsymbol{W_h} + \delta\boldsymbol{W_{\ddot{x}}} + \delta\boldsymbol{W_{\ddot{\theta}}} + \delta\boldsymbol{W_{susp}} + \delta\boldsymbol{W_t} + \delta\boldsymbol{W_\mu} \\ &= -\boldsymbol{C_1}^T\,\boldsymbol{M_h} - \boldsymbol{c_6} - \boldsymbol{C_7}\,\ddot{\boldsymbol{\theta}} - \boldsymbol{I_p}\,\ddot{\boldsymbol{\theta}} + \boldsymbol{C_{17}} + \boldsymbol{C_{18}}\,\ddot{\boldsymbol{\theta}} - m_t\,\boldsymbol{c_{20}} - m_t\,\boldsymbol{C_{21}}\,\ddot{\boldsymbol{\theta}} + \mu\,\boldsymbol{c_{25}} + \mu\,\boldsymbol{C_{26}}\,\ddot{\boldsymbol{\theta}}\end{aligned}$$

At this point it shall be mentioned that different scenarios can be investigated. For example, if one wants to describe the deployment in space one can set $\mu = m_t = g = 0$ and $l_s \to \infty$. By this, the virtual works $\delta \boldsymbol{W_{susp}}$, $\delta \boldsymbol{W_t}$ and $\delta \boldsymbol{W_\mu}$ are zero each which means that the whole suspension system is not taken into account anymore for the equation of motion.

The above equation can be summarized to

$$\boxed{\boldsymbol{M}\,\ddot{\boldsymbol{\theta}} = \boldsymbol{Q}} \quad \text{Basic Equation of Motion} \tag{3.22}$$

with

$$\boldsymbol{M} = \boldsymbol{C_7} + \boldsymbol{I_p} - \boldsymbol{C_{18}} + m_t\,\boldsymbol{C_{21}} - \mu\,\boldsymbol{C_{26}}$$

being the mass matrix; dependent on $\boldsymbol{\theta}$ and the constant system parameters

$m_1, m_2, m_3, m_t, h_h, l, s_p, l_s, g, \mu$

$$\boldsymbol{Q} = -\boldsymbol{C_1}^T\,\boldsymbol{M_h} - \boldsymbol{c_6} + \boldsymbol{c_{17}} - m_t\,\boldsymbol{c_{20}} + \mu\,\boldsymbol{c_{25}}$$

being the load vector; dependent on $\boldsymbol{\theta}$, $\dot{\boldsymbol{\theta}}$ and the constant system parameters

$m_1, m_2, m_3, m_t, m_h, l, s_p, l_s, g, \mu, M_{h0}$

3.3.3 Applying Constraints to the Basic Equation of Motion

The basic equation of motion (3.22) can be used for preliminary investigations. However, it does not take into account that penetration of panels is not allowed. Furthermore, locked hinge lines cannot be simulated. In order to take these problems into consideration constraints must be applied.

Although many more restrictions are possible, only few were considered, because only the one specific initial value problem $\boldsymbol{\theta}(t = 0) = [\pi/2, -\pi/2, \pi/2]^T$ shall be investigated. The following table gives an overview of the basic constraints that were considered.

Restriction	Formulation	Description
R_1	$\theta_1 < \pi/2$	panel 1 shall not penetrate the satellite
R_2	$\theta_1 = 0$	hinge line H_1 is latched
R_3	$\theta_2 = \theta_1$	hinge line H_2 is latched
R_4	$\theta_2 > -\arccos(-1/2\cos\theta_1)$	panel 2 shall not penetrate the satellite
R_5	$\theta_3 < \arccos(-1/2\cos\theta_1 - \cos\theta_2)$	panel 3 shall not penetrate the satellite
R_6	$\theta_3 = \theta_2$	hinge line H_3 is latched
R_7	$\theta_3 > -\arccos(-1/2\cos\theta_1 - \cos\theta_2)$	panel 3 shall not penetrate the satellite
R_8	$\theta_3 < \pi + \theta_2$	panel 3 shall not penetrate panel 2

Table 3.3: Summary of the Basic Restrictions

It can be seen in table 3.3 that the constraints are holonomic[2] as well as non-holonomic[3], but all are scleronomous[4]. Figure 3.12 serves an graphical overview of the basic constraints. Here the difference between the holonomic and non-holonomic constraints can be seen very clearly: In the case of holonomic constraints two boundaries ensure the restriction. In the case of non-holonomic constraints there is only one border, which represents the greater or smaller sign, respectively.

Non-holonomic constraint conditions cannot be easily solved. A continous monitoring of the variables and correction of the equation must be carried out. If a non-holonomic constraint

[2]Constraints are called holonomic if they can be describe in the form of $f_i(\boldsymbol{x}, t) = 0$, where $\boldsymbol{x}$ is the vector of the unconstrained variables and f_i are the constraint functions.

[3]Constraints are called non-holonomic if they cannot be describe in the form of $f_i(\boldsymbol{x}, t) = 0$, e.g. $f_i(\boldsymbol{x}, t) > 0$ or $f_i(\boldsymbol{x}, \dot{\boldsymbol{x}}, t) = 0$.

[4]Constraints are called scleronomous if they are not an explicit function of time, e.g. $f_i(\boldsymbol{x}(t)) = 0$.

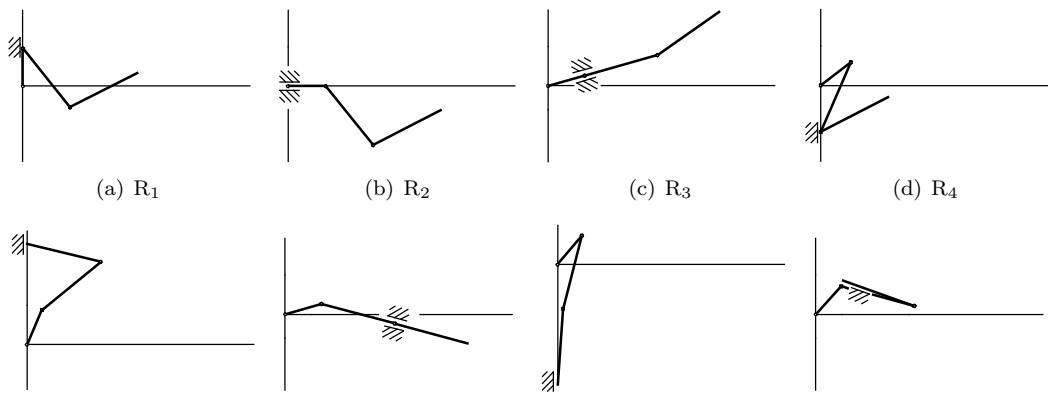

(a) R_1 (b) R_2 (c) R_3 (d) R_4

(e) R_5 (f) R_6 (g) R_7 (h) R_8

Figure 3.12: Graphical Description of the Basic Restrictions

condition is violated the case of the boundary condition can be applied and thus we have a holonomic description again. Holonomic constraint conditions like R_2, R_3 and R_6 can be easily solved by applying a constraint matrix to the basic system of equations.

Handling of Holonomic Constraint Conditions

In this specific problem of deployment of a panel array a holonomic constraint condition can be described as $\theta_i = \theta_i(\boldsymbol{\phi})$, where $\boldsymbol{\phi}$ is the vector of the generalized variables. Depending on the restrictions (and thus the degrees of freedom) the dimension of $\boldsymbol{\phi}$ can vary from 0 to 3.

For a complete formulation of the basic equation of motion with the new generalized variables, their derivatives with respect to time are necessary,

$$\dot{\boldsymbol{\theta}} = \frac{\partial \boldsymbol{\theta}}{\partial t} = \frac{\partial \boldsymbol{\theta}}{\partial \boldsymbol{\phi}} \frac{\partial \boldsymbol{\phi}}{\partial t} = \boldsymbol{J}\, \dot{\boldsymbol{\phi}} \tag{3.23}$$

In this equation $\boldsymbol{J}$ is the Jacobian matrix. The second derivative of $\boldsymbol{\theta}$ with respect to time is

$$\ddot{\boldsymbol{\theta}} = \frac{\partial \dot{\boldsymbol{\theta}}}{\partial t} = \frac{\partial \boldsymbol{J}}{\partial \boldsymbol{t}}\, \dot{\boldsymbol{\phi}} + \boldsymbol{J}\, \frac{\partial \dot{\boldsymbol{\phi}}}{\partial \boldsymbol{t}} = \dot{\boldsymbol{J}}\, \dot{\boldsymbol{\phi}} + \boldsymbol{J}\, \ddot{\boldsymbol{\phi}} \tag{3.24}$$

The quantity $\dot{\boldsymbol{J}}$ could be written as $(\partial \boldsymbol{J}/\partial \boldsymbol{\phi})\dot{\boldsymbol{\phi}}$ but this would mean introducing a rank 3 tensor. Instead one can find a matrix expression:

$$\dot{\boldsymbol{J}} = \frac{\partial \boldsymbol{J}}{\partial \boldsymbol{\phi}}\, \dot{\boldsymbol{\phi}} = \frac{\partial (\boldsymbol{J}\, \dot{\boldsymbol{\phi}})}{\partial \boldsymbol{\phi}} = \frac{\partial \dot{\boldsymbol{\phi}}}{\partial \boldsymbol{\phi}} \tag{3.25}$$

While applying constrains on the basic system, new forces (or moments respectively) appear. The vector of these constraint forces $\boldsymbol{Q_c}$ must be added to the basic system of equations,

$$\boldsymbol{M}\, \ddot{\boldsymbol{\theta}} = \boldsymbol{Q} + \boldsymbol{Q_c} \tag{3.26}$$

In this equation $\boldsymbol{M}$, $\ddot{\boldsymbol{\theta}}$ and $\boldsymbol{Q}$ are now dependent on $\boldsymbol{\phi}$, $\dot{\boldsymbol{\phi}}$ and $\ddot{\boldsymbol{\phi}}$. The principle of virtual work however requires that the virtual work of $\boldsymbol{Q_r}$ due to an arbitrary virtual displacement of $\boldsymbol{\theta}$ must be zero.

$$[\delta(\boldsymbol{\theta})]^T \boldsymbol{Q_c} = 0 \qquad , \forall\, \delta(\boldsymbol{\theta})$$

The virtual displacement can be expressed by the generalized variables

$$\delta(\boldsymbol{\theta}) = \frac{\partial \boldsymbol{\theta}}{\partial \boldsymbol{\phi}}\, \delta(\boldsymbol{\phi}) = \boldsymbol{J}\, \delta(\boldsymbol{\phi})$$

and the previous equation can be written as

$$[\delta(\boldsymbol{\phi})]^T \boldsymbol{J}^T \boldsymbol{Q_c} = 0 \qquad ,\forall\, \delta(\boldsymbol{\phi})$$

or as

$$\boldsymbol{J}^T \boldsymbol{Q_c} = \boldsymbol{0}.$$

If one premultiplies equation (3.26) with $\boldsymbol{J}^T$, replaces the dependent by the generalized variables and takes the previous equation into account, one finally receives the constrained equation of motion

$$\boxed{\boldsymbol{J}^T \boldsymbol{M}\, \boldsymbol{J}\, \ddot{\boldsymbol{\phi}} = \boldsymbol{J}^T \boldsymbol{Q} - \boldsymbol{J}^T \boldsymbol{M}\, \dot{\boldsymbol{J}}\, \dot{\boldsymbol{\phi}}} \quad \text{Constrained Equation of Motion} \tag{3.27}$$

An Example of Applying Holonomic Constraint Conditions

In order to demonstrate how to apply holonomic constraints on the basic equation of motion (3.22) the conditions R_2 and R_6 (ref. table 3.3 and figure 3.12) shall be set. Physically, this means that the first and the third hinge line are locked. Thus we have only one degree of freedom left, which means that the vector of the generalized variables is

$$\boldsymbol{\phi} = [\phi_1].$$

The dependent variables are now described by ϕ_1.

$$\boldsymbol{\theta} = [0, \phi_1, \phi_1]^T$$

The Jacobian matrix and it derivative are

$$\boldsymbol{J} = \begin{bmatrix} \frac{\partial \theta_1}{\partial \phi_1} & \frac{\partial \theta_2}{\partial \phi_1} & \frac{\partial \theta_3}{\partial \phi_1} \end{bmatrix}^T = \begin{bmatrix} 0 & 1 & 1 \end{bmatrix}^T$$
$$\dot{\boldsymbol{J}} = \begin{bmatrix} 0 & 0 & 0 \end{bmatrix}^T$$

and therefore the derivatives of θ are

$$\dot{\boldsymbol{\theta}} = \begin{bmatrix} 0 & \dot{\phi}_1 & \dot{\phi}_1 \end{bmatrix}^T$$
$$\ddot{\boldsymbol{\theta}} = \begin{bmatrix} 0 & \ddot{\phi}_1 & \ddot{\phi}_1 \end{bmatrix}^T.$$

The constraint equation of motion (3.27) can then be written as

$$(M_{22} + M_{23} + M_{32} + M_{33})\ddot{\phi}_1 = Q_2 + Q_3.$$

Handling of Non-holonomic Constraint Conditions

As it will be shown later, the equations of motion are solved (integrated) iteratively. At each time the second derivative of θ can be determined. Provided that the old values of θ do not violate any restrictions, the new values for θ and $\dot{\theta}$ can be calculated using the simple Euler formula:

$$\boldsymbol{\theta_{new}} = \boldsymbol{\theta_{old}} + \dot{\boldsymbol{\theta}}_{\boldsymbol{old}}\, \Delta t + \frac{1}{2}\, \ddot{\boldsymbol{\theta}}\, \Delta t^2.$$

If $\boldsymbol{\theta_{new}}$ now violates one or more non-holonomic constraint conditions the integration step must be repeated using another equation of motion. The new equation contains holonomic constraints which represent the boundary of the corresponding non-holonomic restrictions. The newly calculated values of θ now meet all non-holonomic restrictions and the iteration can be continued with the previous equation of motion.

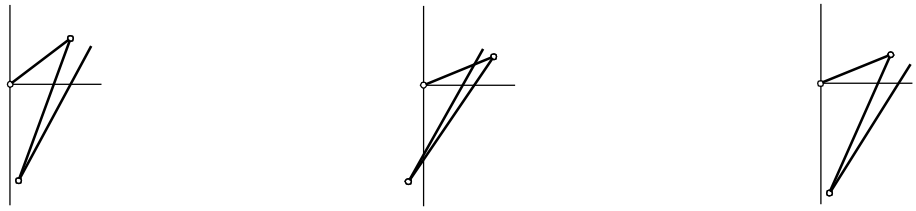

(a) θ_{old}: no restrictions violated

(b) first calculation of θ_{new} using the unconstrained equation of motion: R_4 and R_8 are violated

(c) second calculation of θ_{new} using holonomic boundary constraint conditions: no restrictions are violated

Figure 3.13: Example of two Non-holonomic Restrictions Being Violated and its Handling

An Example of Applying Non-holonomic Constraint Conditions

Assuming no hinge lines are latched we have the relationship

$$\boldsymbol{\theta} = \begin{bmatrix}\phi_1 & \phi_2 & \phi_3\end{bmatrix}^T$$

and thus

$$\boldsymbol{J} = \boldsymbol{E}(\mathbf{3})$$
$$\dot{\boldsymbol{J}} = \mathbf{0}(\mathbf{3})$$

which means that the constrained equation of motion is the same as the basic one:

$$\boldsymbol{M}\,\ddot{\boldsymbol{\phi}} = \boldsymbol{Q}$$

During the integration the following situation may occur. In figure 3.13-a the panels with the angles θ_{old} is drawn. Using the same equation of motion after the next iteration step the panels would have the configuration as shown in figure 3.13-b. The restrictions R_4 and R_8 would be violated at the same time. That means that the integration step must be repeated using the boundary conditions.

The boundary condition of R_4 can be written as

$$\theta_2 = -\arccos(\epsilon_1 - 1/2\cos\theta_1).$$

with the (very small) positive constant ϵ_1. The boundary condition of R_8 is

$$\theta_3 = \pi + \theta_2 - \epsilon_2 = \pi - \arccos(\epsilon_1 - 1/2\cos\theta_1) - \epsilon_2.$$

where ϵ_2 is another (very small) positive constant. These two formulations give rise to two physical constraints. First, the lower joint between panel 2 and 3 will move on a straight line parallel to the y-axis or the wall, respectively. Second, panel 3 will have the same separation angle to panel 2. This all means that the system consists of one degree of freedom.

The necessary expressions in equation (3.27) are found using the equations of the subsection on page 24.

$$\boldsymbol{\phi} = [\phi_1]$$

$$\boldsymbol{\theta} = \begin{bmatrix} \phi_1 \\ -\arccos(\epsilon_1 - 1/2\cos\phi_1) \\ \pi - \arccos(\epsilon_1 - 1/2\cos\phi_1) - \epsilon_2 \end{bmatrix}$$

$$\boldsymbol{J} = \begin{bmatrix} 1 \\ \frac{1}{2}\sin(\phi_1)/\sqrt{1-(\epsilon_1 - 1/2\cos\phi_1)^2} \\ \frac{1}{2}\sin(\phi_1)/\sqrt{1-(\epsilon_1 - 1/2\cos\phi_1)^2} \end{bmatrix}$$

$$\dot{\boldsymbol{\theta}} = \boldsymbol{J}\,\dot{\boldsymbol{\phi}}$$

$$\dot{\boldsymbol{J}} = \begin{bmatrix} 0 \\ \frac{1}{2}\frac{\dot{\phi}_1\cos\phi_1}{\sqrt{1-(\epsilon_1-1/2\cos\phi_1)^2}} + \frac{1}{4}\frac{\dot{\phi}_1\sin^2\phi_1(-1/2\cos\phi_1+\epsilon_1)}{(1-(\epsilon_1-1/2\cos\phi_1)^2)^{3/2}} \\ \frac{1}{2}\frac{\dot{\phi}_1\cos\phi_1}{\sqrt{1-(\epsilon_1-1/2\cos\phi_1)^2}} + \frac{1}{4}\frac{\dot{\phi}_1\sin^2\phi_1(-1/2\cos\phi_1+\epsilon_1)}{(1-(\epsilon_1-1/2\cos\phi_1)^2)^{3/2}} \end{bmatrix}^T$$

With these expressions, the acceleration $\ddot{\boldsymbol{\phi}}$ can be calculated and the new values for $\dot{\boldsymbol{\phi}}$ and $\boldsymbol{\phi}$ can be found using the Euler formula. Having the new values of the generalized variables the values of $\boldsymbol{\theta_{new}}$ and $\dot{\boldsymbol{\theta}}_{\boldsymbol{new}}$ are easy to find. Thus the correct position and velocity of the panels were calculated, which is shown in figure 3.13 (c).

For the next iteration step the constraints must be abolished again. If then constraints are violated, the same procedure as described above must carried out again.

3.3.4 Latching and Impact

Introduction and Notation

As already mentioned above the hinge lines can and shall get latched. At this point, the number of degrees of freedom decreases by one and the describing equation of motion can be found by applying constraints to the basic equation. However, during the time of latching there are impacts which cause changes in the angular velocities.

In order to simplify the description of the processes the following nomenclature for the constrained equations and the latching is used.

Every constrained equation of motion has its own number which is stored in the variable eq. As constraint conditions can either be fulfilled or not, a similar-binary system was used:

$$eq = \sum_{i=1}^{8} \begin{cases} 0 & \text{if } \mathrm{R}_i \text{ is true} \\ 2^i & \text{if } \mathrm{R}_i \text{ is false} \end{cases} \tag{3.28}$$

By this the basic equation of motion is represented by $eq = 0$.

A latching process is described by the value of la. Figure 3.14 shows the definition of la and all possible latching sequences. In this figure all non-holonomic constraints (penetrating) are neglected.

One can see that there are only six different latching sequences and 12 different latching processes.

An arbitrary latching process is uniquely determined by the restriction of angular velocities after the latching ($\dot{\boldsymbol{\theta}}^a = [\dot{\theta}_1^a,\ \dot{\theta}_2^a,\ \dot{\theta}_3^a]^T$), and the existence of angular impacts in the hinge lines during the latching process. In fig. 3.15-b all possible linear and angular impacts in the hinge lines are shown. Table 3.4 lists all latching processes with its determinations/restrictions. It can be seen that case 4 and 6, case 5 and 8 and case 7 and 9 are the same, respectively. Cases 10-12 have the simple solutions $\dot{\boldsymbol{\theta}}^a = [0, 0, 0]^T$. Thus only 6 cases must be considered.

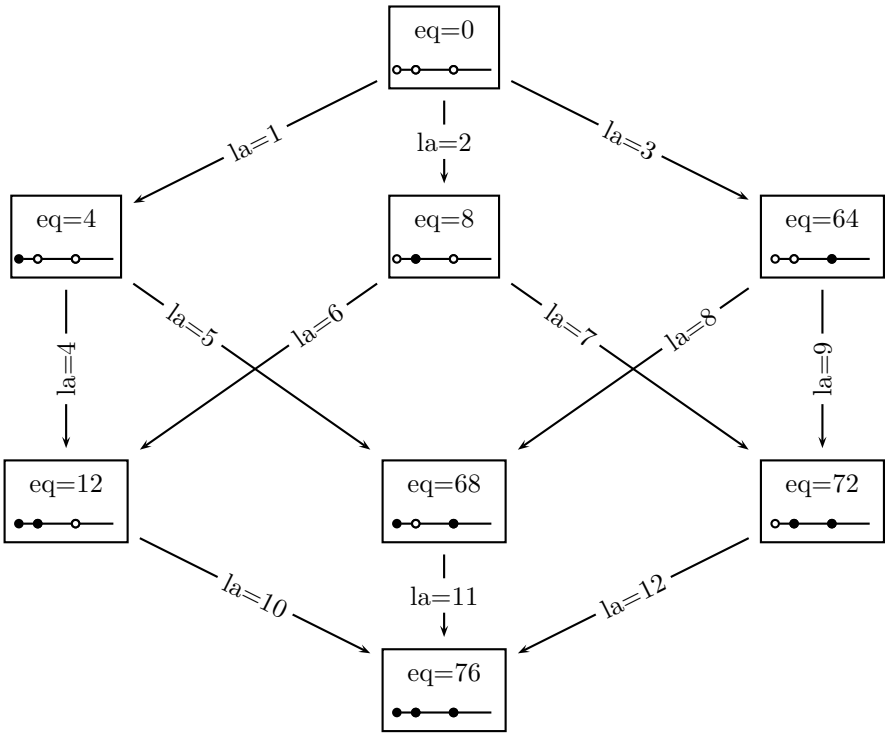

Figure 3.14: The six Possible Latching Sequences, filled circles symbolize locked hinge lines

Angular Velocities after Latching

The physical background for each latching process can be summarized in two equations, of which both describe the relationship between impulse and momentum,

$$\begin{aligned}
\Delta \boldsymbol{p}_i &= \boldsymbol{p}_i^a - \boldsymbol{p}_i^b && \text{definition} \\
&= \int_{t_b}^{t_a} \sum_k \boldsymbol{F}_k dt = \sum_k (\boldsymbol{S_F})_k && \text{load term} \\
&= m_i \left(\dot{\boldsymbol{x}}_i^a - \dot{\boldsymbol{x}}_i^b \right) && \text{kinematic term}
\end{aligned}$$

$$\begin{aligned}
\Delta L_i &= L_i^a - L_i^b && \text{definition} \\
&= \int_{t_b}^{t_a} \sum_k \mathbf{M}_k dt = \sum_k (S_M)_k + \sum_k \left[\boldsymbol{x}_{\mathrm{H}_k} \times (\boldsymbol{S_F})_k \right]_{z-\mathrm{coord}} && \text{load term} \\
&= I_i \left(\dot{\theta}_i^a - \dot{\theta}_i^b \right) + \left[\boldsymbol{x}_i \times m_i \left(\dot{\boldsymbol{x}}_i^a - \dot{\boldsymbol{x}}_i^b \right) \right]_{z-\mathrm{coord}} && \text{kinematic term}
\end{aligned}$$

The first equation (2 components) states that the change of the linear momentum of panel i, which is the panel mass m_i times the difference of the velocity of the panel's centre $\dot{\boldsymbol{x}}_i^a - \dot{\boldsymbol{x}}_i^b$, is equal to the sum of all linear impulse $\boldsymbol{S_F}$ at the k corresponding hinge lines.

The second equation shows the relationship between the change of the angular momentum and the angular impulse. The angular momentum is composed of an angular $(I_i \dot{\theta}_i)$ and a linear $([\boldsymbol{x}_i \times m_i \dot{\boldsymbol{x}}_i]_z)$ component. The sum of all angular impulses consists of angular (S_M) and linear $(\boldsymbol{S_F})$ impulses at the k corresponding hinge lines H_k. $\boldsymbol{x}_{\mathrm{H}_k}$ is the position vector of hinge line H_k.

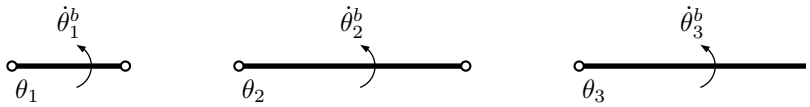

(a) angular velocities before latching

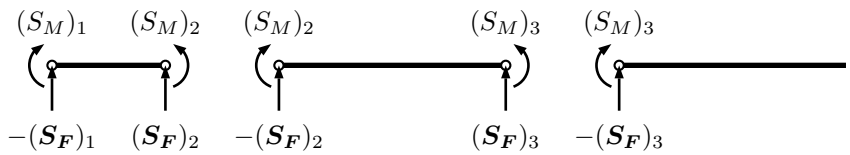

(b) possible impulse loads at the hinge lines due to latching; the linear impulses $\boldsymbol{S_F}$ are drawn perpendicular but in reality they have an arbitrary direction

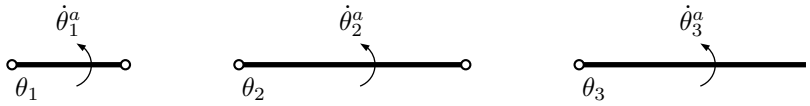

(c) angular velocities after latching

Figure 3.15: Description of an Arbitrary Latching Process

case / latching process	angular velocities after latching			angular impulses		
la	$\dot{\theta}_1^a$	$\dot{\theta}_2^a$	$\dot{\theta}_3^a$	$(S_M)_1$	$(S_M)_2$	$(S_M)_3$
1	0				0	0
2		$\dot{\theta}_{1a}$		0		0
3			$\dot{\theta}_{2a}$	0	0	
4	0	0				0
5	0		$\dot{\theta}_{2a}$		0	
6	0	0				0
7		$\dot{\theta}_{1a}$	$\dot{\theta}_{1a}$	0		
8	0		$\dot{\theta}_{2a}$		0	
9		$\dot{\theta}_{1a}$	$\dot{\theta}_{1a}$	0		
10	0	0	0			
11	0	0	0			
12	0	0	0			

Table 3.4: Description of an Arbitrary Latching Process: angular velocities after latching and angular impulses during latching

The vector of linear momentum is introduced as

$$\begin{aligned}\boldsymbol{p} &= [p_{1x}, p_{1y}, p_{2x}, p_{2y}, p_{3x}, p_{3y}]^T \\ &= \boldsymbol{m_p}\,\dot{\boldsymbol{x}} = \boldsymbol{m_p}\,\boldsymbol{C_4}\,\dot{\boldsymbol{\theta}}.\end{aligned}$$

The vector of angular momentum $\boldsymbol{L} = [L_1, L_2, L_3]^T$ around the coordinate origin is (written in Einstein's summation convention)

$$L_i = I_{ij}\,\dot{\theta}_j + x_k\,\delta_{kl}^{(i)}\,p_l \qquad\qquad i,j = 1\ldots3;\;\; k,l = 1..6$$

with $\delta_{kl}^{(i)}$ as a modified Kronecker matrix which replaces the cross product by a matrix multipli-

cation

$$\delta_{kl}^{(i)} = \begin{cases} 1 & \text{if } k = 2i-1 \text{ and } l = 2i \\ -1 & \text{if } k = 2i \text{ and } l = 2i-1 \\ 0 & \text{otherwise} \end{cases}$$

The vector of angular momentum can be simplified

$$\begin{aligned} L_i &= I_{ij}\,\dot{\theta}_j + (C_2)_{kl}\,(C_3)_{lm}\,\delta_{mn}^{(i)}\,(m_p)_{np}\,(C_4)_{pj}\,\dot{\theta}_j \\ &= (C_{27})_{ij}\,\dot{\theta}_j \\ \boldsymbol{L} &= \boldsymbol{C_{27}}\,\dot{\boldsymbol{\theta}} \end{aligned}$$

The change of the linear momentum

$$\begin{aligned} \Delta\boldsymbol{p} &= \boldsymbol{p}^a - \boldsymbol{p}^b \\ &= \boldsymbol{m_p}\,\boldsymbol{C_4}\,\left(\dot{\boldsymbol{\theta}}^a - \dot{\boldsymbol{\theta}}^b\right) \end{aligned}$$

must be the same as the sum of the corresponding linear impulses (ref. figure 3.15-b)

$$\begin{aligned} \Delta\boldsymbol{p} &= \begin{bmatrix} -1 & 0 & 1 & 0 & 0 & 0 \\ 0 & -1 & 0 & 1 & 0 & 0 \\ 0 & 0 & -1 & 0 & 1 & 0 \\ 0 & 0 & 0 & -1 & 0 & 1 \\ 0 & 0 & 0 & 0 & -1 & 0 \\ 0 & 0 & 0 & 0 & 0 & -1 \end{bmatrix} \begin{bmatrix} [(S_F)_1]_x \\ [(S_F)_1]_y \\ [(S_F)_2]_x \\ [(S_F)_2]_y \\ [(S_F)_3]_x \\ [(S_F)_3]_y \end{bmatrix} \\ &= \boldsymbol{C_{28}}\,\boldsymbol{S_F}. \end{aligned}$$

The vector of the linear impulses at the hinge lines is then

$$\boldsymbol{S_F} = \boldsymbol{C_{28}}^{-1}\,\boldsymbol{m_p}\,\boldsymbol{C_4}\,\left(\dot{\boldsymbol{\theta}}^a - \dot{\boldsymbol{\theta}}^b\right) \tag{3.29}$$

The change of the angular momentum

$$\begin{aligned} \Delta\boldsymbol{L} &= \boldsymbol{L}^a - \boldsymbol{L}^b \\ &= \boldsymbol{C_{27}}\,\left(\dot{\boldsymbol{\theta}}^a - \dot{\boldsymbol{\theta}}^b\right) \end{aligned}$$

must be the same as the corresponding angular impacts. With the following definitions

$$\boldsymbol{C_{29}} = \begin{bmatrix} -1 & 1 & 0 \\ 0 & -1 & 1 \\ 0 & 0 & -1 \end{bmatrix}$$

$$\boldsymbol{S_M} = \begin{bmatrix} (S_M)_1 & (S_M)_2 & (S_M)_3 \end{bmatrix}^T \qquad \text{vector of the angular impacts}$$

$$\boldsymbol{x_H} = \begin{bmatrix} 0 \\ 0 \\ (l/2 + s_p)\cos\theta_1 \\ (l/2 + s_p)\sin\theta_1 \\ (l/2 + s_p)\cos\theta_1 + (l + s_p)\cos\theta_2 \\ (l/2 + s_p)\sin\theta_1 + (l + s_p)\sin\theta_2 \end{bmatrix} \qquad \text{position vector of the hinge lines}$$

$$\delta_{kl}^{(4)} = 0 \qquad \text{the above introduced modified Kronecker matrix does not exist for } i = 4$$

the change of the angular momentum due to the impulses can be written as

$$\Delta L_i = (C_{29})_{ij}\,(S_M)_j + (x_H)_k\,(\delta_{kl}^{(i+1)} - \delta_{kl}^{(i)})\,(S_F)_l \qquad \text{or in matrix notation}$$

$$\Delta\boldsymbol{L} = \boldsymbol{C_{29}}\,\boldsymbol{S_M} + \boldsymbol{C_{30}}\,\boldsymbol{S_F}.$$

Substituting $\boldsymbol{S_F}$ with the expression from (3.29), the expression for the change of angular momentum is

$$\Delta \boldsymbol{L} = \boldsymbol{C_{29}}\, \boldsymbol{S_M} + \boldsymbol{C_{30}}\, \boldsymbol{C_{28}}^{-1} \boldsymbol{m_p}\, \boldsymbol{C_4} \left(\dot{\boldsymbol{\theta}}^a - \dot{\boldsymbol{\theta}}^b \right).$$

Bringing both expressions of the change of the angular momentum in one equation one obtains.

$$\left(\dot{\boldsymbol{\theta}}^a - \dot{\boldsymbol{\theta}}^b \right) = (\boldsymbol{C_{27}} - \boldsymbol{C_{30}}\, \boldsymbol{C_{28}}^{-1} \boldsymbol{m_p}\, \boldsymbol{C_4})^{-1}\, \boldsymbol{C_{29}}\, \boldsymbol{S_M}$$

or

$$\boxed{\dot{\boldsymbol{\theta}}^a = \boldsymbol{B}\, \boldsymbol{S_M} + \dot{\boldsymbol{\theta}}^b} \quad \text{Basic Latching Equation} \tag{3.30}$$

Equation (3.30) gives the simple relationship between the changes of the panels' angular velocities on one side and the occurring angular impacts in the hinge lines on the other side. Matrix $\boldsymbol{B}$ shall be called the impulse matrix.

As shown in table 3.4, three of the six unknowns ($\dot{\boldsymbol{\theta}}^a$ and $\boldsymbol{S_M}$) are determined for each latching process. Thus the basic latching equation (3.30) can be solved for the remaining three unknown variables.

An Example of a Latching Process

To demonstrate the above equation the latching process $la = 2$ shall be investigated.

Before latching all hinge lines are unlocked. Then hinge line 2 gets latched. During latching there must be an angular impact at that hinge line. At the other two joints no angular impulses apply. After latching, the angular velocities of panel 1 and 2 must be the same.

The basic latching equation is now written down for the specific case of $la = 2$.

$$\begin{bmatrix} \dot{\theta}_1^a \\ \dot{\theta}_1^a \\ \dot{\theta}_3^a \end{bmatrix} = \begin{bmatrix} B_{11} & B_{12} & B_{13} \\ B_{21} & B_{22} & B_{23} \\ B_{31} & B_{32} & B_{33} \end{bmatrix} \begin{bmatrix} 0 \\ (S_M)_2 \\ 0 \end{bmatrix} + \begin{bmatrix} \dot{\theta}_1^b \\ \dot{\theta}_2^b \\ \dot{\theta}_3^b \end{bmatrix}$$

Solving for the unknown variables one obtains

$$\begin{aligned} (S_M)_2 &= \frac{\dot{\theta}_2^b - \dot{\theta}_1^b}{B_{12} - B_{22}} \\ \dot{\theta}_1^a = \dot{\theta}_2^a &= \frac{B_{12}\, \dot{\theta}_2^b - B_{22}\, \dot{\theta}_1^b}{B_{12} - B_{22}} \\ \dot{\theta}_3^a &= \frac{B_{32}\, \dot{\theta}_2^b - B_{32}\, \dot{\theta}_1^b}{B_{12} - B_{22}} + \dot{\theta}_3^b \end{aligned}$$

3.3.5 Initial Value Problem

The initial position of the array at $t = 0$ is

$$\boldsymbol{\theta}(t = 0) = \begin{bmatrix} \pi/2^- \\ -\pi/2^+ \\ \pi/2^- \end{bmatrix} \tag{3.31}$$

The minus or plus sign indicates that the angles are just a little smaller or bigger than $\pm\pi/2$, respectively. This is necessary, because otherwise the restrictions R_1, R_4 and R_5 from section 3.3.3 would be violated.

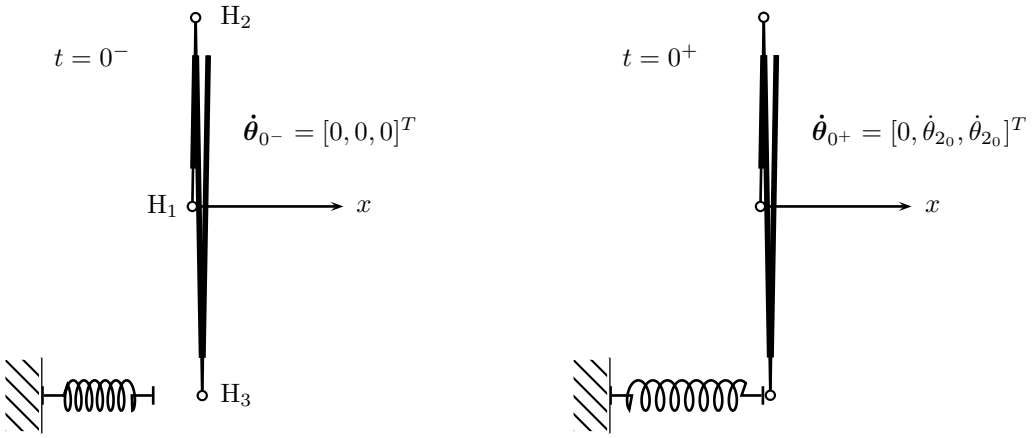

(a) Before the release: the release spring is in compressed configuration; the panels don't move; all energy is stored potentially in the spring

(b) After the release: the spring is fully expanded; panel 2 and 3 rotate with the same angular velocity around H_2; all energy is stored kinetically in the array

Figure 3.16: Idealized Release System: a Spring Pushes Panel 2 at Hinge Line H_3

In order to better control the deployment behaviour of the array, a release spring at the hinge line H_3 shall be used, as shown in figure 3.16.

The potential energy stored in the spring in the compressed configuration $E_{s,pot}$ is introduced, in order to describe that release mechanism. After the spring is released it pushes the array at the hinge line H_3. In reality it would be done some distance away from that point. It was assumed that the potential energy of the spring is transformed into kinetic energy of the array without any loss[5]. Two more simplifications were made. Firstly, without any constraints, using equation (3.22) and different amounts of impacts at H_3, it can be shown that panel 1 would always have a positive angular velocity shortly after the push. Because panel 1 already touches the stand ($\theta_1 = \pi/2^-$) the initial angular velocity of panel 1 must be zero: $\dot{\theta}_{1_0} = 0$. Secondly, panel 2 and 3 must rotate with the same velocity because both touch each other and penetration is not allowed.

The kinetic energy of the array is

$$\begin{aligned} E_{a,kin} &= \frac{1}{2}\dot{\boldsymbol{x}}^T \boldsymbol{m_p}\, \dot{\boldsymbol{x}} + \frac{1}{2}\dot{\boldsymbol{\theta}}^T \boldsymbol{I_p}\, \dot{\boldsymbol{\theta}} \\ &= \frac{1}{2}\dot{\boldsymbol{\theta}}^T \boldsymbol{C_4}^T \boldsymbol{m_p}\, \boldsymbol{C_4}\, \dot{\boldsymbol{\theta}} + \frac{1}{2}\dot{\boldsymbol{\theta}}^T \boldsymbol{I_p}\, \dot{\boldsymbol{\theta}} \\ &= \frac{1}{2}\dot{\boldsymbol{\theta}}^T \left(\boldsymbol{C_4}^T \boldsymbol{m_p}\, \boldsymbol{C_4} + \boldsymbol{I_p}\right) \dot{\boldsymbol{\theta}}. \end{aligned} \tag{3.32}$$

with $\boldsymbol{C_4}$, $\boldsymbol{m_p}$ and $\boldsymbol{I_p}$ from equation (3.7), (3.9) and (3.12), respectively.

For the case of $t = 0$ we can simplify equation (3.32) using the above assumptions.

$$E_{a,kin}(t=0) = \frac{\dot{\theta}_{2_0}^2}{48}\left[\left(8l^2 + 12ls_p + 6s_p^2\right)(m_2 + m_3) + \left(18l^2 + 18ls_p + 9s_p^2\right) m_h\right]$$

With the condition $E_{a,kin}(t=0) = E_{s,pot}$ the initial angular velocities can be calculated and the initial values are complete[6]

$$\dot{\boldsymbol{\theta}}(t=0) = \sqrt{\frac{48E_{s,pot}}{\left(8l^2 + 12ls_p + 6s_p^2\right)(m_2 + m_3) + \left(18l^2 + 18ls_p + 9s_p^2\right) m_h}} \begin{bmatrix} 0 \\ 1 \\ 1 \end{bmatrix} \tag{3.33}$$

[5] Resulting from this assumption, the position of the release spring does not affect the initial velocities.

[6] Neglecting the small masses of the hinge lines m_h would change the initial velocities by approximately 0.2%.

3.3.6 Solver for the Equation of Motion

The theoretical solution for the panel deployment has been developed in the previous sections. In this section the strategy for solving the equation(s) of motion is presented.

In mathematical terms the system is a non-linear ordinary differential equation of second order. This system could be solved using already existing routines, like `MATLAB`'s `ode23`-Solver. This would, however, require one equation of motion. Because this problem consists of many different equations of motion and because a powerful monitoring of the variables is required an original solver was programmed. The programming language was `MATLAB` because this software package already consists of many useful functions like matrix calculations. The numerical integration used Taylor series (Euler method) with the small time increment Δt:

$$\begin{aligned} \boldsymbol{\theta}(t+\Delta t) &= \boldsymbol{\theta}(t) + \dot{\boldsymbol{\theta}}(t)\Delta t + \frac{1}{2}\ddot{\boldsymbol{\theta}}(t)\Delta t^2 \\ \dot{\boldsymbol{\theta}}(t+\Delta t) &= \dot{\boldsymbol{\theta}}(t) + \ddot{\boldsymbol{\theta}}(t)\Delta t \end{aligned} \tag{3.34}$$

The Program

In figure 3.17 a flow chart of the main program is drawn. The functions that were used are explained in the following.

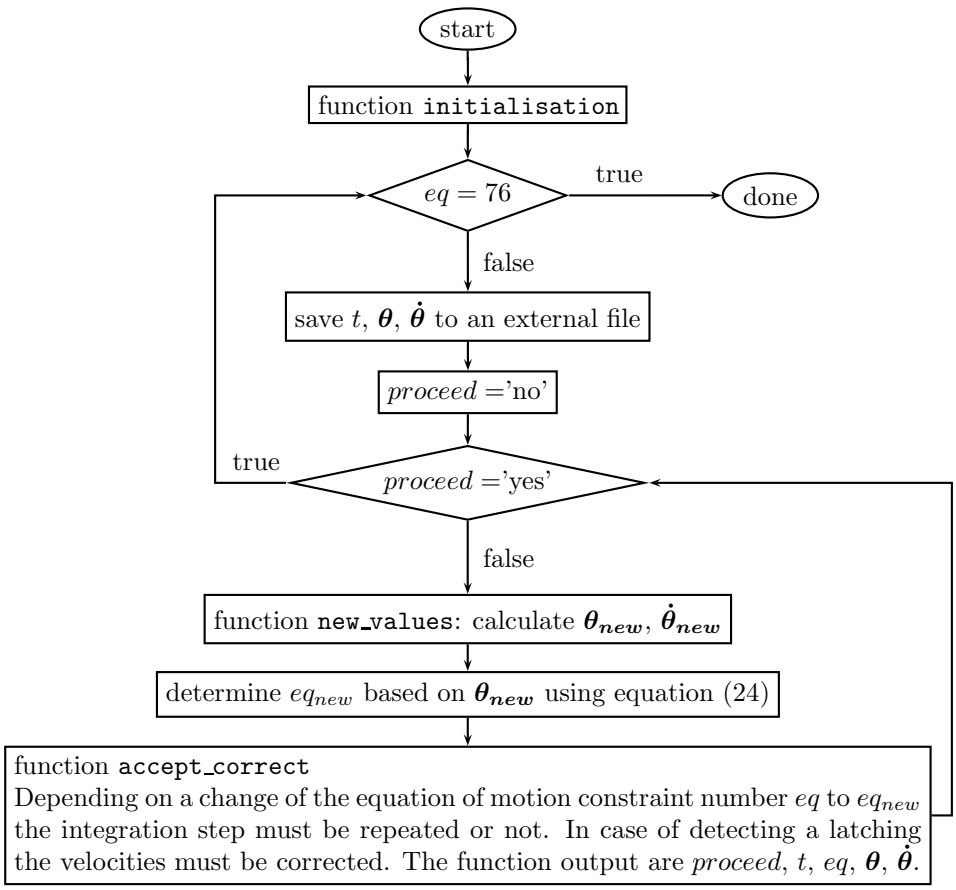

Figure 3.17: Flow Chart of the Main Program

- The function `initialisation` asks for the parameter (l, s_p, l_s, m_1, m_2, m_3, m_t, m_h, g, μ, $E_{s,pot}$). The initial values ($\boldsymbol{\theta}(t=0)$, $\dot{\boldsymbol{\theta}}(t=0)$) are calculated. The time increment Δt must be set. Finally the values of time and equation constraint number are initialized: $t = 0$, $eq = 0$.

- Next, the integration starts. It ends when all hinge lines are latched, which means that the constraint conditions R_2, R_3 and R_6 (refer table 3.3) are true. Using (3.28), for this case the equation of motion constraint number is $la = 76$.

- During every integration step the values of the angles and the velocities of the panels are saved into an external file.

- The variable *proceed* is introduced. It determines if the integration can continue to the next step. The function `accept_correct` sets the value of *proceed*. In the beginning of every integration step *proceed* is initialized with 'no'.

- The function `new_values` calculates the new values $\boldsymbol{\theta_{new}}$, $\dot{\boldsymbol{\theta}}_{\boldsymbol{new}}$. In detail the following steps are carried out:
  - setting of the generalized variables $\boldsymbol{\phi}$ and $\dot{\boldsymbol{\phi}}$ depending on eq
  - calculation of $\boldsymbol{J}$ and $\dot{\boldsymbol{J}}$ using (3.23) and (3.25)
  - calculation of $\ddot{\boldsymbol{\phi}}$ using (3.27)
  - calculation of $\ddot{\boldsymbol{\theta}}$ using (3.24)
  - calculation of $\boldsymbol{\theta_{new}}$ and $\dot{\boldsymbol{\theta}}_{\boldsymbol{new}}$ using (3.34)

- After the calculation of the new values for the panel angles and velocities it is investigated which constraints are violated now. The new equation of motion constraint number is stored in the variable eq_{new}.

- The function `accept_correct` is the most complex part. The main task of this function is to determine if the new calculated angles are permissible and thus if the iteration can continue to the next step. The determination is done comparing eq and eq_{new}.
  But firstly the set of equation of motion constraint numbers which contain only holonomic constraint conditions is defined:

$$H = \{0, 4, 8, 12, 64, 68, 72, 76\} \tag{3.35}$$

  This set summarizes all motions that don't violate any non-holonomic constraint conditions. Five different combinations of eq and eq_{new} are possible, as follows.

  - $eq \in H,\ eq = eq_{new}$
    - The new values can be accepted and the next iteration step can be lead through.
    - $\boldsymbol{\theta} = \boldsymbol{\theta_{new}}$, $\dot{\boldsymbol{\theta}} = \dot{\boldsymbol{\theta}}_{\boldsymbol{new}}$, $t = t + \Delta t$, $eq = eq_{new}$, $proceed =$ 'yes'
  - $eq \in H,\ eq \neq eq_{new},\ eq_{new} \in H$
    - A latching has happened. The velocities must be corrected using the latching equation (3.30) to $\dot{\boldsymbol{\theta}}^{\boldsymbol{la}}_{\boldsymbol{new}}$
    - $\boldsymbol{\theta} = \boldsymbol{\theta_{new}}$, $\dot{\boldsymbol{\theta}} = \dot{\boldsymbol{\theta}}^{\boldsymbol{la}}_{\boldsymbol{new}}$, $t = t + \Delta t$, $eq = eq_{new}$, $proceed =$ 'yes'
  - $eq \in H,\ eq \neq eq_{new},\ eq_{new} \notin H$
    - The new values of the panel angles violate at least one non-holonomic constraint condition. The iteration step must be repeated using a constraint equation of motion as described in section 3.3.3. The new carried out iteration step uses the old values of angles, velocities and time.
    - ($\boldsymbol{\theta} = \boldsymbol{\theta}$, $\dot{\boldsymbol{\theta}} = \dot{\boldsymbol{\theta}}$, $t = t$), $eq = eq_{new}$, $proceed =$ 'no'

- $eq \notin H,\ eq = eq_{new}$
  - Due to the definition of non-holonomic constraint equation of motions (section 3.3.3) this case can never occur.
- $eq \notin H,\ eq \neq eq_{new},\ eq_{new} \in H$
  - In a previous calculation of the integration step a violation of the non-holonomic restrictions had occurred. Now, having used a non-holonomic constrained equation of motion, the angles are acceptable. The integration can continue.
  - $\boldsymbol{\theta} = \boldsymbol{\theta_{new}}$, $\dot{\boldsymbol{\theta}} = \dot{\boldsymbol{\theta}}_{\boldsymbol{new}}$, $t = t + \Delta t$, $eq = eq_{new}$, $proceed =$ 'yes'
- $eq \notin H,\ eq \neq eq_{new},\ eq_{new} \notin H$
  - Using a non-holonomic constrained equation of motion, the new angles violate one or more different non-holonomic restrictions. The integration step must be carried out one more time. The now applied constraint equation of motion number eq^*_{new} must consist of all in this step arisen non-holonomic restrictions.
  - $(\boldsymbol{\theta} = \boldsymbol{\theta}$, $\dot{\boldsymbol{\theta}} = \dot{\boldsymbol{\theta}}$, $t = t)$, $eq = eq^*_{new}$, $proceed =$ 'no'

- In some cases the integration would never come to a stop because the defined end ($eq = 76$) can never be reached. An example is $\boldsymbol{\theta} = [0, 0, \pi^-]^T$.

Influence of Time Increment Δt

Advanced ODE solvers use the fourth-order Runge-Kutta formula with adaptive step size control (see [14], p. 714). The Euler formula used in this case has the big advantage of its simplicity. However, the Euler method is not very accurate when compared to others, or needs smaller step sizes to achieve the same accuracy.

In order to reduce the computing time the time increment should be chosen as small as possible. Simulations were run with $\Delta t = [0.5s,\ 0.1s,\ 0.05s,\ 0.01s,\ 0.005s,\ 0.001s]$. As a reference scenario the deployment in space with the following data was investigated:

$$
\begin{aligned}
m_1 &= 1 \text{ kg} \\
m_2 &= 4.6 \text{ kg} \\
m_3 &= 4.5 \text{ kg} \\
m_h &= 62.66 \text{ g} \\
l &= 0.9 \text{ m} \\
s_p &= 0.083 \text{ m} \\
M_{h0} &= 0.2922 \text{ Nm} \\
E_{pot,0} &= 0 \text{ Nm}
\end{aligned}
$$

Table 3.5 summarizes the results from the sensitivity studies. All simulations result in the same latching sequence. The latching times don't vary very much for Δt smaller than $0.01s$.

time increment Δt	0.5	0.1	0.05	0.01	0.005	0.001	rel $\text{err}_{0.01}^{0.001}$	rel $\text{err}_{0.005}^{0.001}$
latching time of H_1	5.000	4.800	4.800	4.810	4.810	4.809	+0.02%	+0.02%
latching time of H_3	8.000	7.300	7.200	7.110	7.105	7.095	+0.21%	+0.14%
latching time of H_2	16.50	15.00	14.75	14.63	14.60	14.58	+0.32%	+0.08%
computing time[7]	0.210	0.851	1.602	7.681	15.71	100.5	201%	576%

Table 3.5: Sensitivity Study of the Time Increment Δt (in s) for Solving the Simulation

[7] in seconds; on a Pentium III, 548MHz, 392MB

Figure 3.18 illustrates the deployment calculated once with $\Delta t = 0.001$ s and then $\Delta t = 0.01$ s. On this scale very small visual differences can be seen from $t = 8$ s onwards. Panel 2 and 3 – calculated with $\Delta t = 0.01$ s – have a slightly smaller (negative) angle than in the simulation run with $\Delta t = 0.001$ s. On a similar plot with $\Delta t = 0.001$ s versus $\Delta t = 0.005$ s one would recognize no differences even in larger scales.

In order to achieve accurate results in a relative short computing time the time step was set to

$$\Delta t = 0.005 \text{ s}. \tag{3.36}$$

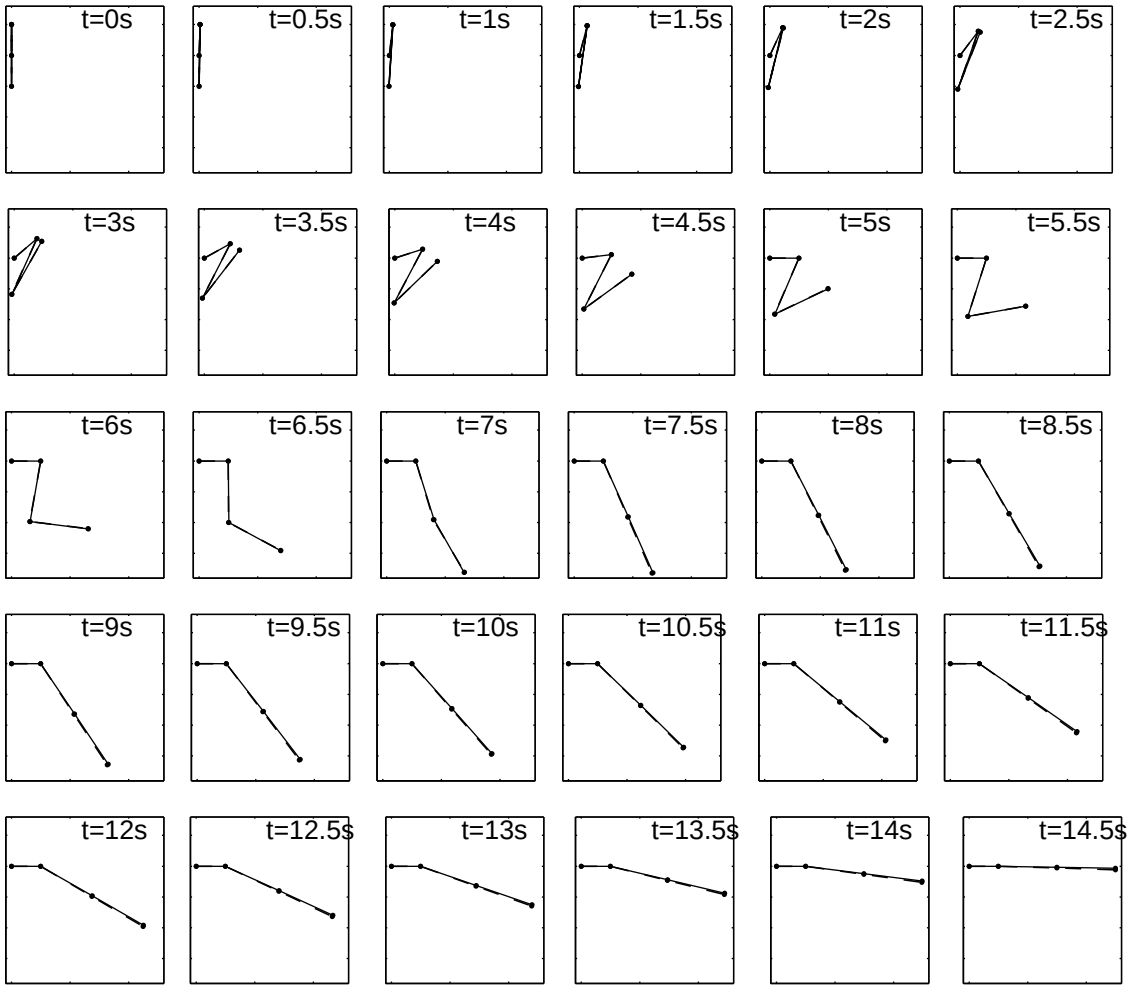

Figure 3.18: The Influence of the Time Increment Δt on the Solution of the Simulation; solid line: $\Delta t = 0.001$ s; dashed line: $\Delta t = 0.01$ s

3.4 Experimental Determination of Simulation Parameters

In section 3.3 a simulation of the array deployment (equations to mathematically describe the motion and latching sequence; a program to solve the equations and receive the positions of the panels at each point of time) was derived. Still there are two parameters which must be experimentally determined to run simulations.

The tape springs in the three hinge lines will be assumed to have the same constant moment M_{h0}. Section 3.4.1 deals with the determination of the value of M_{h0}.

Another unknown parameter is the coefficient of friction μ, introduced in section 3.3.2. To get an approximate idea about the order of magnitude, in section 3.4.2 some experiments were run.

3.4.1 Moment in the Hinge Lines

Two adjacent panels are connected by four tape springs. Fig 3.19 illustrates the hinge line H_1 which connects the stand or the spacecraft, respectively with the yoke. The tape springs have an angle to the x-axis. The advantage of this construction is that less space is required in the folded configuration. However, as the rotation axis is parallel to the z-axis the tape springs' moment consist not only of a bending portion but also of a torsional portion. Values for the bending moment of Tape Spring Rolamite (TSR) hinges can be found in [13], chapter 3. Typical values for a pair of tape springs range from 100 Nmm to 300 Nmm.

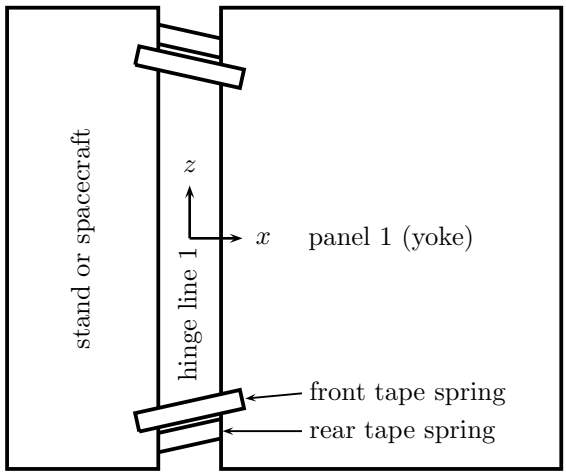

Figure 3.19: Detailed View of Hinge Line H_1

In order to measure the moment in one hinge line, the one-rail suspension system was used. Panel 2 was fixed so that $\theta_2 = 0$. Panel 3 was moved until it had an excursion of $\theta_3 \approx \pi/3$ and afterwards it was fixed, too. Now an entirely vertical suspension string was attached to the centre of panel 3. On the upper end of that suspension string a second string was added. At the bottom end a small mass was attached, which could be used as a plumb line. Then panel 3 was released again.

Figure B.1 shows panel 3 in the experimental set-up. Because of the moment in the hinge line the panel moves out of the position of the plumb line until the restoring force of the suspension equalizes the moment.

Two different determinations of the moment were carried out. Firstly, the deflection of the plumb-bob line of panel 3's centre s_F was measured (figure 3.20). Secondly the restoring force F, cf. figure 3.21, was measured.

Measurement of Deflection of the Plumb Bob Line

In figure 3.20 the deflection s_F is a result of the moment in the hinge line M_{h0}. The suspension string compensates on the one hand the weight of panel 3 (z-direction), and on the other hand the hinge moment (y^*-direction, see fig. 3.20-b):

$$F_{susp,z} = m_3 g$$
$$F_{susp,y} l_F = M_{h0}$$

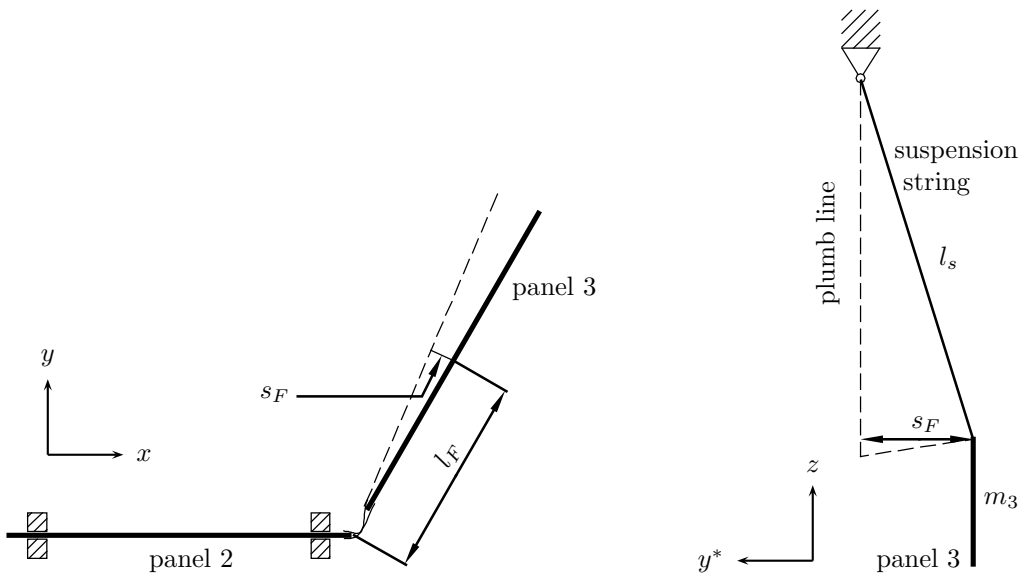

(a) top view: panel 3 has deflection of the plumb-bob line

(b) view along the length of panel 3

Figure 3.20: The First Experimental Method to Determine the Moment in the Hinge Line: Measuring the Deflection of the Plumb-Bob Line s_F

where l_F is the lever arm. Both force components of the suspension string are connected by the relation

$$\frac{F_{susp,z}}{F_{susp,y}} = \frac{\sqrt{l_s^2 - s_F^2}}{s_F}.$$

The moment of the hinge line can be calculated by

$$M_{h0} = \frac{s_F}{\sqrt{l_s^2 - s_F^2}} l_F m_3 g \tag{3.37}$$

With the input values

$$\begin{aligned} m_3 &= 2.25 \text{ kg} \pm 0.1 \text{ kg} \\ g &= 9.81 \text{ kg/m}^2 \\ l_F &= 520 \text{ mm} \pm 5 \text{ mm} \\ s_F &= 51 \text{ mm} \pm 1 \text{ mm} \\ l_s &= 1880 \text{ mm} \pm 7 \text{ mm} \end{aligned}$$

the value of the moment in the hinge line is

$$M_{h0} = 0.3115 \text{ Nm} \pm 0.0241 \text{ Nm} \tag{3.38}$$

Measurement of the Restoring Force

In contrast to section 3.4.1 now the deflection of the plumb-bob line must be zero (see figure 3.21). To achieve this, the restoring force F was applied. Figure B.2 on page 88 shows the experimental set-up for this method. The force is generated by a heavy stand and transmitted via the bending beam and a string to the panel 3.

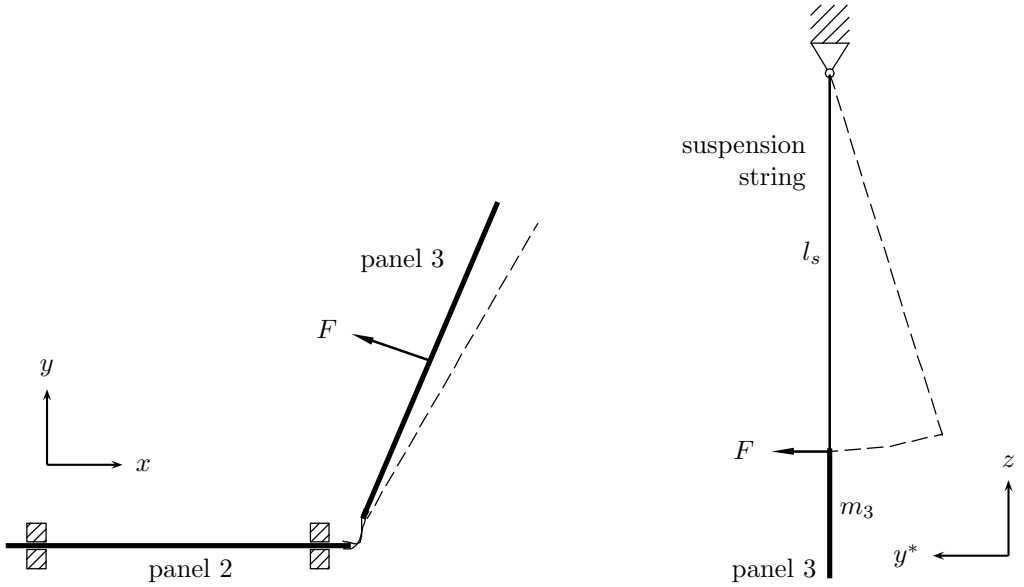

(a) top view: by applying the restoring force F the panel's centre is on the plumb line

(b) view along the length of panel 3

Figure 3.21: The Second Experimental Method to Determine the Moment in the Hinge Line: Measuring the Restoring Force F

The restoring force is measured using the bending beam with strain gauges. After calibrating this equipment the force was measured several times and the average was calculated from

$$\begin{aligned} F &= \bar{F} \pm \Delta F \\ &= 0.5247 \text{ N} \pm 0.0131 \text{ N} \end{aligned}$$

Using the length of lever arm l_F from the previous section the moment can be derived

$$M_{h0} = 0.2728 \text{ Nm} \pm 0.0068 \text{ Nm} \tag{3.39}$$

The Result

For a first assessment the average of the results from section 3.4.1 and 3.4.1 was used.

$$M_{h0} = 0.2922 \text{ Nm} \tag{3.40}$$

3.4.2 Coefficient of Friction

In section 3.3.2 the coefficient of friction μ was introduced in order to describe the existence of friction between trolley and rail. For preliminary simulations it was necessary to asses the order of magnitude. This experiment shall help to determine the importance of friction.

In figure 3.22 a picture of the overall test set-up is shown. A rail is mounted in such a way that it is perfectly horizontal. The trolley (and its frame) are located on the rail. A weight is attached to the bottom end of the frame. The trolley can be pulled with different velocities. The pulling force, which is equivalent to the friction force, is measured again with the bending beam with strain gauges as described in section 3.4.1. A close-up view of the trolley and the measuring equipment can be seen in figure B.3.

Two different tests were carried out. Firstly the coefficient of static friction and secondly the coefficient of kinetic friction were determined.

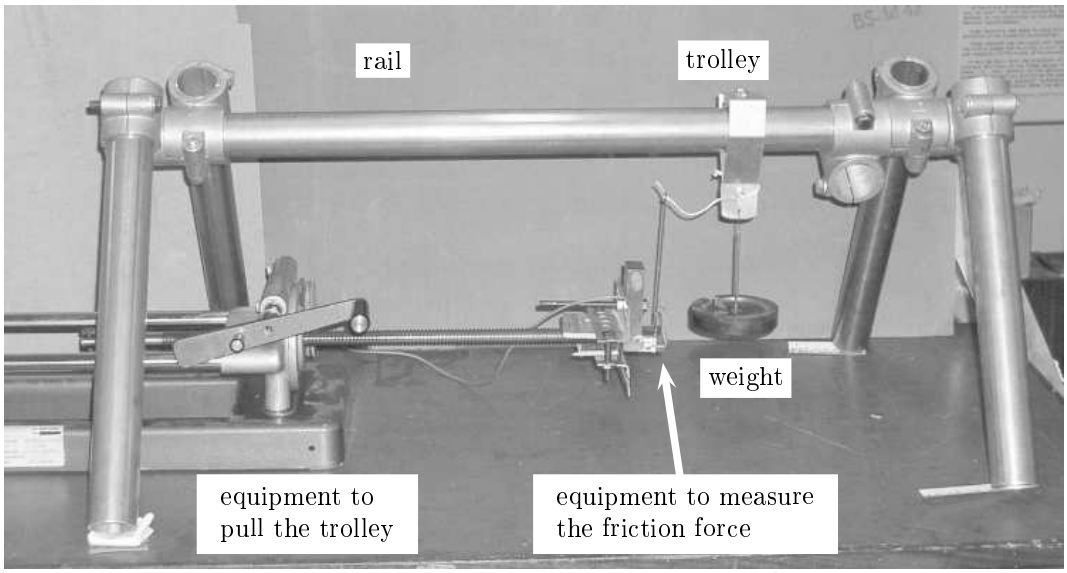

Figure 3.22: Experimental Set-up for Measuring the Friction Force in Dependence on the Normal Force

Coefficient of Static Friction

The principle of determining the coefficient of static friction was very simple. Different weights (normal forces F_n) were attached to the trolley. The trolley was pulled very slowly at speeds of

$$v_{stat} = 0.02 \ldots 0.20 \text{ mm/s}$$

The pulling force was measured using a flexible beam with strain gauges attached to its surface and recorded every 0.5 s using a data logger. Figure 3.23 shows a typical set of data points. The pulling force/force of friction rises up to a maximum until the trolley moves a little. The force jumps back to almost zero. This procedure was repeated several times. It can be seen in figure 3.23 that the value of the maximum varies a lot, which can be explained by the unevenness of the rail and by variabilities in the bearing balls and cage.

The masses of the attached weights were 2 kg, 3 kg, 4 kg, 5 kg, 6 kg and 10 kg. Adding the mass of the trolley and its frame $m_t = 0.215$ kg the normal forces were

$$F_n = (m_{\text{weight}} + m_t)g$$

Figure 3.24 shows a diagram in which the measured maximal forces of static friction F_μ are plotted against the applied normal force F_n. The maximum forces of static friction are the peaks in figure 3.23.

The regression through all the points results show an almost direct proportionality. The coefficient of static friction calculated in this manner is

$$\mu_{stat} = 0.005552 \tag{3.41}$$

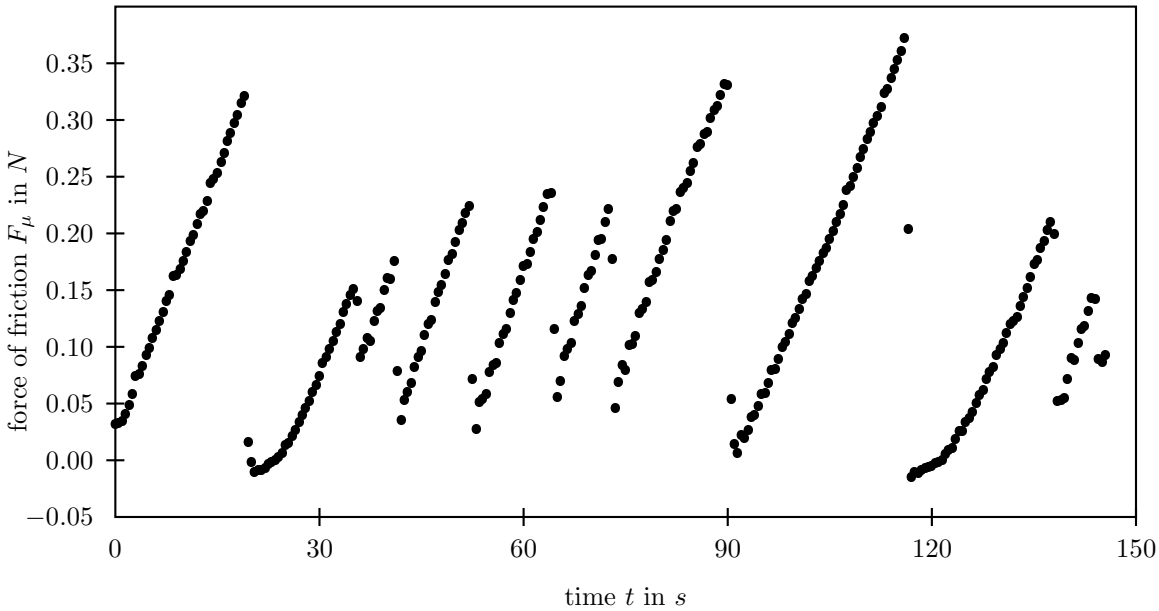

Figure 3.23: The Force of Friction vs. Time; Trolley was moved with $v_{min} = 0.02$ mm/s; Weight = 4 kg

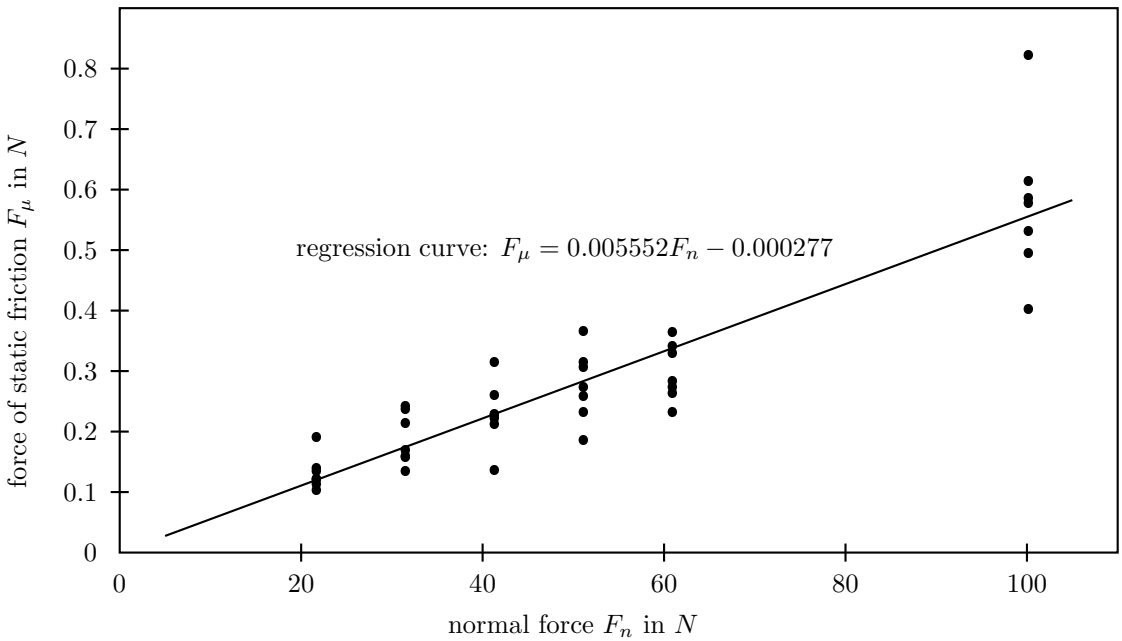

Figure 3.24: The Force of Static Friction vs. Normal Force

Coefficient of Kinetic Friction

The kinetic friction was measured similarly to the static test. The only difference was the velocity of pulling the trolley: $v_{kin} = 8.93$ mm/s. Figure 3.25 shows how the measured pulling forces change over the testing time. The very high variations seem to be a result of the variability of the bearings. Due to this fact the trolley and the weight are some times accelerated (pulled), and other times they move by their own momentum.

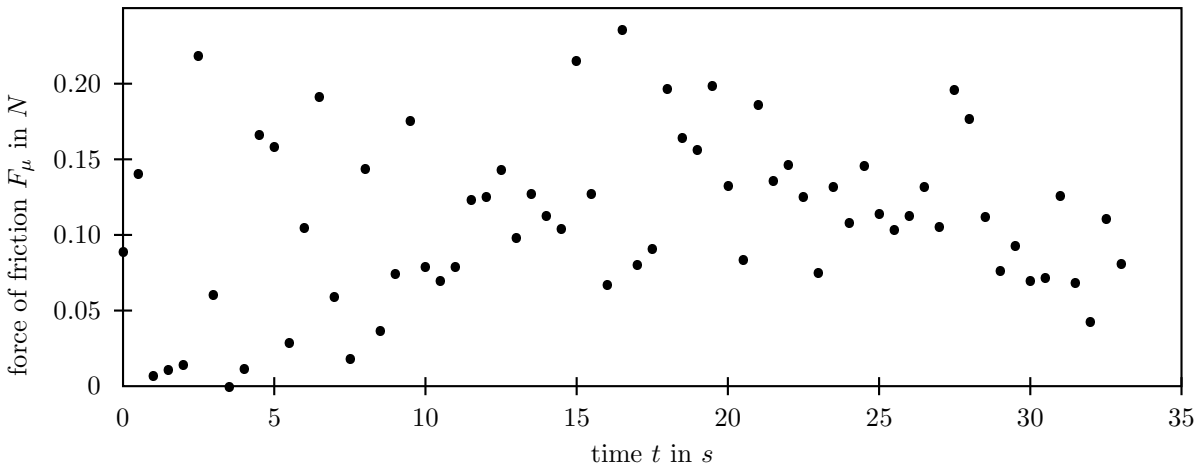

Figure 3.25: Force of Friction vs. Time; Trolley was moved with $v \approx 9$ mm/s; Weight = 4 kg

During tests with different weight masses, the average of the pulling forces as well as the maximum occurring pulling force for each test were noted. The results can be seen in figure 3.26. The coefficient of kinetic friction is then given by

$$\mu_{kin} = 0.002457 \tag{3.42}$$

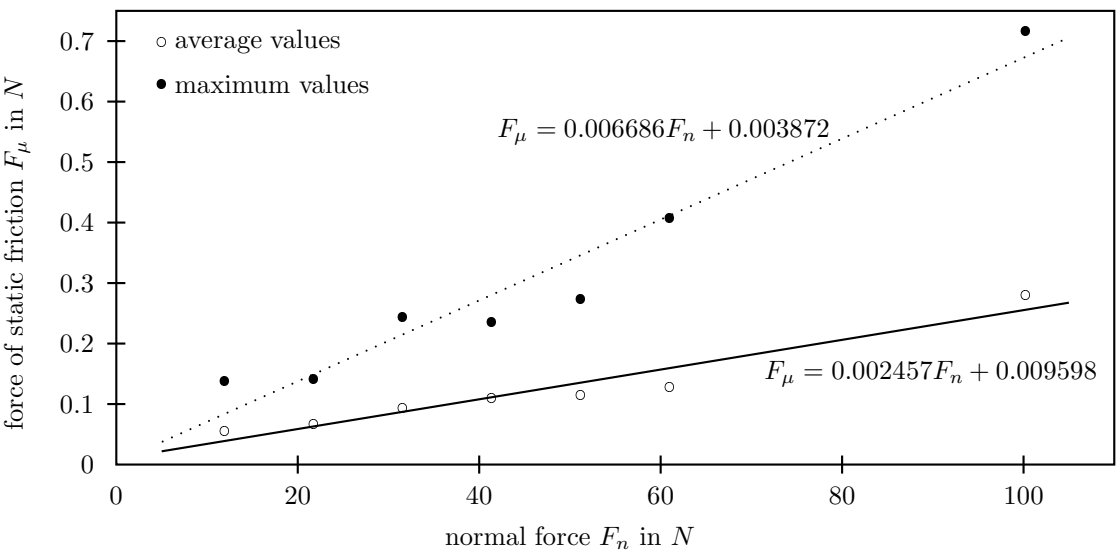

Figure 3.26: Force of Kinetic Friction vs. Normal Force

3.5 Results of the Simulation

In this section the simulation of section 3.3 is used with the parameters measured in section 3.4 to have first assessments of the deployment behaviour of this array type consisting of two and a half panels.

In the following, a summary of the simulations that were carried out and the motivation for them is given.

- Firstly, the deployment procedure of the test array in space was investigated. The aim was to get an initial feeling of how the array would behave, and which latching sequence is to be expected. Two cases were considered: First, initial kinetic energy was provided, in order to fulfil the requirements of SSTL. Second, no initial energy was provided, because this case was also investigated in the experiments.
- The next step was to predict the unfolding of the experimental array supported by the ORSS. Because the values for M_{h0} and μ from the experiments were too untrustworthy (see section 3.4), sensitivity studies on these two variables were performed.
  The results of this simulation were later on compared with results from the deployment experiment.

For this sections the following standard values of the equation parameters were used. They represent the deployment of the test array with the one-rail suspension system and an initial kinetic energy.

$$\begin{aligned} l &= 0.9 \text{ m} & s_p &= 0.083 \text{ m} & l_s &= 1.829 \text{ m} \\ m_1 &= 1.125 \text{ kg} & m_2 &= 2.25 \text{ kg} & m_3 &= 2.25 \text{ kg} \\ m_h &= 0.063 \text{ kg} & m_t &= 0.215 \text{ kg} & g &= 9.81 \text{ m/s}^2 \\ \mu &= 0.002457 & E_{s,pot} &= 0.1 \text{ J} & M_{h0} &= 0.2922 \text{ Nm} \end{aligned} \tag{3.43}$$

In some of the simulations the above basic simulation parameter were changed; any new values will be mentioned.

3.5.1 Deployment of Test Array in Space

To simulate the deployment in space with an initial push the following standard parameter must be changed.

$$g = 0\text{m/s}^2 \qquad l_s = 10^{10} \text{ m (any high value)} \qquad m_t = 0 \text{ kg} \qquad \mu = 0$$

The results are presented in figure A.1.

One can recognize that with an initial push ($E_{s,pot} = 0.1$ J) the panels' centres move very near the symmetry axis (x-axis). The maximal excursion in the y-direction is much smaller than in the case that there is no initial push ($E_{s,pot} = 0.0$ J). Furthermore the deployment time (4.160 s) is only half of the deployment time without pushing (8.265 s).

The latching sequence is the same for both cases: first hinge line H_1 gets latched, than the springs of H_3 lock. Finally panel 2 and 3 rotate together until H_2 latches.

3.5.2 Deployment of Test Array on Ground

In this section the experiment from section 3.6 is simulated. For all the simulations presented in this section no initial energy was provided, hence

$$E_{s,pot} = 0$$

Figure A.2 shows the results using the standard parameters. It must be mentioned that the constraints that prevent penetration of the stand was not used, as it did not happen in the experiment.

One can see the typical deployment behaviour. First, the whole array rotates around the root hinge H_1. The panels unfold a little until panel 1 swings back to the starting position (3 s - 4 s). Then the whole structure deploys in a more or less symmetric zig-zag shape. H_1 and H_2 get latched almost at the same time: 6.945 s and 6.990s, respectively. The deployment process finishes with the latching of H_3 at $t = 7.770$ s.

Compared with the deployment of the same array under space conditions (see fig. A.1, dashed line), one must note that the latching sequence is equal but the behaviour is different. The excursions are smaller and the latching times differ considerably.

Now, the influence of the two experimental determined simulation parameter M_{h0} and μ on the simulation results are investigated.

Sensitivity to the Moment in the Hinge Line

sensitivity case	latching times in s of H_1	H_2	H_3
$M_{h0} = 0.25$ Nm	7.770	8.240	8.390
$M_{h0} = 0.2922$ Nm	6.945	6.990	7.770
$M_{h0} = 0.35$ Nm	6.080	6.150	6.270

Table 3.6: Latching Times of the Deployment of the Test Array on Ground; Sensitivity to the Moment in the Hinge Line

The standard value of the moment in the hinge lines ($M_{h0} = 0.2922$ Nm) was increased to $M_{h0} = 0.35$ Nm and decreased to $M_{h0} = 0.25$ Nm. The results can be seen in fig. A.3. The deployment behaviour is very similar in all cases, although the latching times differ, see table 3.6. As expected, with increased moment the unfolding finishes earlier and with decreased moment the deployment lasts longer.

Sensitivity to the Coefficient of Friction

sensitivity case	latching times in s of H_1	H_2	H_3
$\mu = 0.000$	5.675	6.060	5.815
$\mu = 0.001$	6.130	6.295	6.280
$\mu = 0.002457$	6.945	6.990	7.770
$\mu = 0.003$	7.320	7.380	7.950
$\mu = 0.004$	8.400	9.845	8.685

Table 3.7: Latching Times of the Deployment of the Test Array on Ground; Sensitivity to the Coefficient of Friction

The influence of the coefficient of friction μ on the simulation is investigated in this section. Figures A.4 and A.5 show the results of decreasing and increasing the coefficient of friction, respectively. The variation of this parameter does not affect the behaviour very much, although, again the latching times vary. In further sensitivity studies the maximal possible coefficient of friction was determined to $\mu = 0.0063$. Table 3.7 gives a summary of the latching times. It can be seen that the latching sequence changes with different μ but the latchings always happen within the last $0.8s$ of the deployment.

3.6 Deployment Experiment

3.6.1 Introduction

One is interested in the position and orientation of the panels at every time of the deployment. In order to achieve this, the ends of each panel were marked with white points on a black background. A digital movie camera was fixed on a tripod in such a way that the whole deployment procedure could be recorded.

The advantage of this instrument is the high number of images per time (30 frames/s) which guarantees a smooth movie. On the other hand the resolution is quite low (720 × 576 pixel) which decreases the accuracy.

Taking a picture with a camera always involves distortion. E.g., a rectangle in reality (3D) is deformed to an arbitrary quadrangle in the resulting image (2D). The following sections deal with

- the theoretical background of mapping
- the camera calibration
- the test runs
- digitizing one test run.

3.6.2 Theoretical Background of Mapping

While taking pictures with a camera the 3D world is mapped onto a 2D image with some distortion. This distortion can, however, be described in a mathematical model. Considering a simple pin-hole camera an object in 3D is projected onto a plane. This type of projection is called a planar projective projection. The fundamental law for this mapping is

$$\frac{r}{f} = \frac{X}{Z}$$

where

r	the distance from the image point to the optical axis
f	the focal length
X	the distance from the object point to the optical axis
Z	the distance from the optical centre to projected object point

Let $\boldsymbol{x} = [x, y, z]^T$ be the vector pointing to an object in the world coordinate system and $\boldsymbol{u} = [u, v]^T$ the vector pointing to the corresponding image point in the image coordinate system. It can be shown that the relationship between the two coordinate systems is ([7], equation 2.5-47):

$$\begin{bmatrix} su \\ sv \\ s \end{bmatrix} = \begin{bmatrix} p_{11} & p_{12} & p_{13} & p_{14} \\ p_{21} & p_{22} & p_{23} & p_{24} \\ p_{31} & p_{32} & p_{33} & p_{34} \end{bmatrix} \begin{bmatrix} x \\ y \\ z \\ 1 \end{bmatrix}$$

Assuming that all object points are on a plane with a constant z-coordinate one can reduce the system of equations to:

$$\begin{bmatrix} su \\ sv \\ s \end{bmatrix} = \begin{bmatrix} p_{11} & p_{12} & p_{13} \\ p_{21} & p_{22} & p_{23} \\ p_{31} & p_{32} & p_{33} \end{bmatrix} \begin{bmatrix} x \\ y \\ 1 \end{bmatrix}$$

With the restriction that z = constant one can thus obtain the original world coordinates of an object if the image coordinates are given.

$$\begin{bmatrix} x \\ y \\ 1 \end{bmatrix} = \begin{bmatrix} q_{11} & q_{12} & q_{13} \\ q_{21} & q_{22} & q_{23} \\ q_{31} & q_{32} & 1 \end{bmatrix} \begin{bmatrix} su \\ sv \\ s \end{bmatrix}$$

By eliminating s, this can also be written as

$$\begin{aligned} x &= \frac{q_{11}u + q_{12}v + q_{13}}{q_{31}u + q_{32}v + 1} \\ y &= \frac{q_{21}u + q_{22}v + q_{23}}{q_{31}u + q_{32}v + 1} \end{aligned} \tag{3.44}$$

Equation (3.44) gives thus a transformation function from the image to the world coordinate system. The eight unknown coefficients q_{ij} can be determined by calibration of the camera.

3.6.3 Camera Calibration

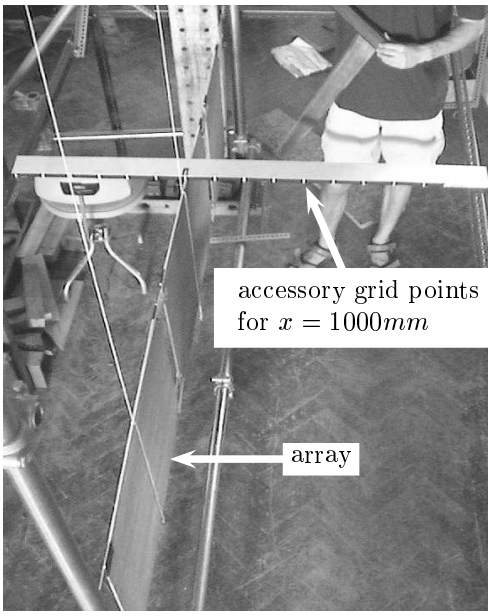

Figure 3.27: Points of the Accessory Grid for $x = 1000$

In the previous section the mapping function was derived. The calibration of the camera requires at least 4 world points to determine the unknown coefficients in equation (3.44).

Camera calibration is the name given to the process of discovering the projection matrix from an image. In this case, not a matrix but two functions of representation (see previous section) are searched for.

To find the functions of representation an accessory grid was created. This grid represented a coordinate system with

- the $x-$ axis on the upper edge of the panels
- the $z-$ axis being the symmetry axis of the first hinge line having the opposite orientation of $\boldsymbol{g}$
- the $y-$ axis being perpendicular to the $x-$ and $z-$ axis creating a right-handed coordinate system

Figure 3.27 shows a photo taken during the calibration. In figure 3.28 the accessory grid is plotted.

The next step was to investigate the images.

From the video file, one frame was exported to a bitmap file (an example can be seen in figure 3.27). In this file the coordinates (in pixels) of the grid points were determined. The image of the original grid is plotted in figure 3.29. The distortion can be seen clearly, as can the existence of at least one vanishing point.

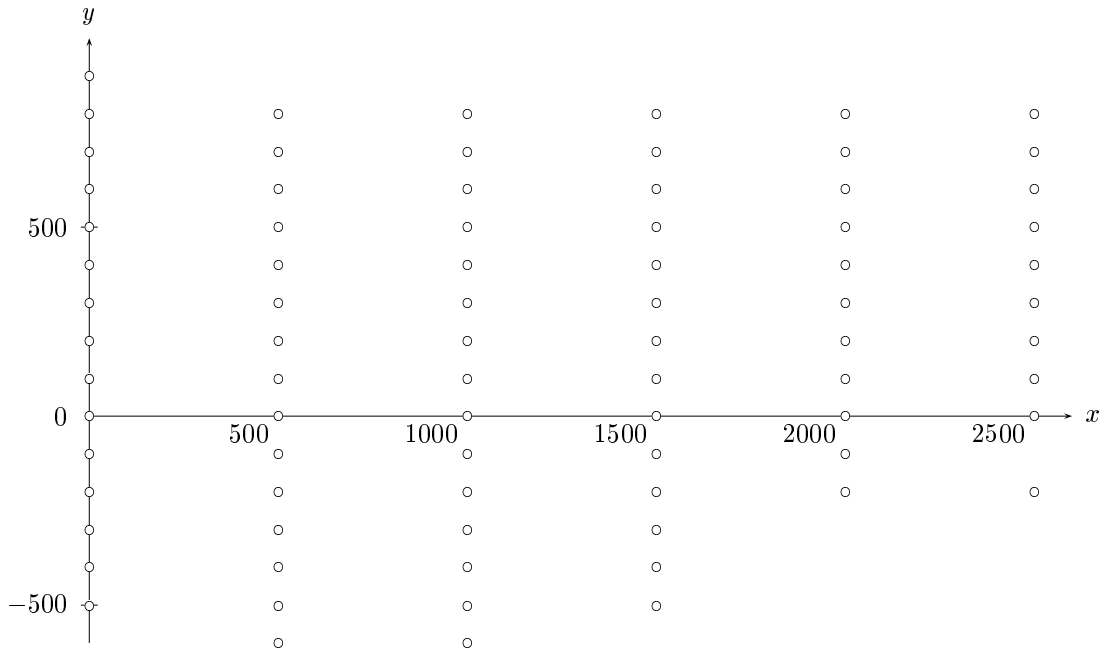

Figure 3.28: Points of the Accessory Grid in the World Coordinate System (x, y)

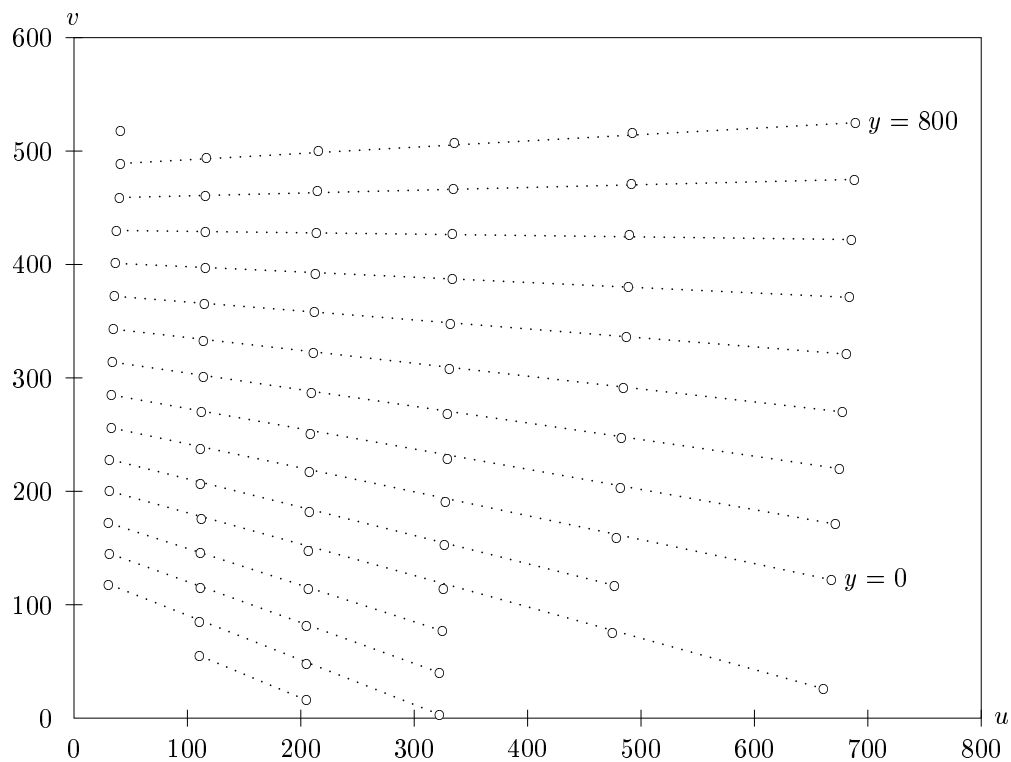

Figure 3.29: Points of the Accessory Grid in the Image Coordinate System (u, v)

Having 80 points of the grid in both coordinate systems, the coefficients q_{ij} of equation (3.44) can be determined using the method of linear least squares. In figure 3.30 equation (3.44) was used with the determined coefficients to plot the grid points in the world coordinate system using the points from the image (ref. fig. 3.29). Additionally the original points of the grid were plotted. It can be seen that equation (3.44) describes the mapping quite accurately. The deviations can be explained by positioning the (real) 'vertical' grid points not exactly perpendicular to the x-axis.

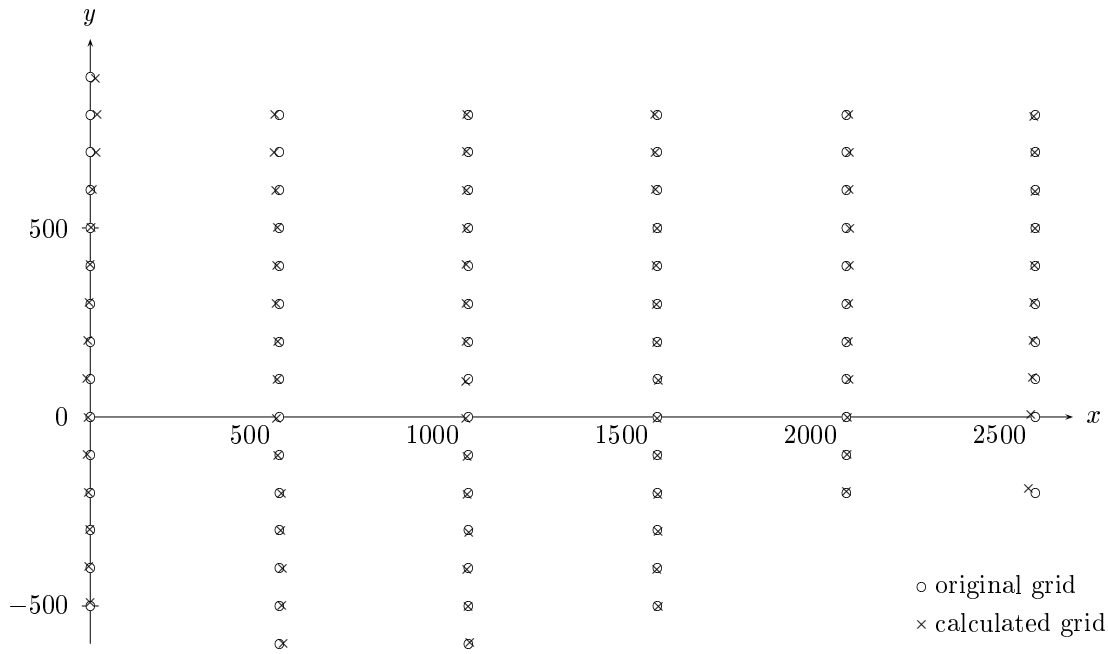

Figure 3.30: Points of the Accessory Grid in the World Coordinate System (x, y) — Circles symbolize the Original (true) Points, Crosses symbolize the Points Calculated by using the Belonging Bitmap Image

3.6.4 Test Runs

After the calibration of the camera, the test runs were carried out, according to the following *modus operandi*. The panels were folded to the initial position $\boldsymbol{\theta} = [\pi/2,\ -pi/2,\ pi/2]^T$. No initial energy was provided so that the initial velocities were all zero. The deployment times that where measured are presented in table 3.8.

run	1	2	3	4	5	6	7	aver.	relsdv
t [s]	9.008	8.474	6.973	7.060	7.060	8.141	8.374	7.870	8.69%

Table 3.8: The Deployment Times of the Test Runs

It can be seen that the relative standard deviation is quite high (8.69%). This deviation can be explained that the release system was a very primitive one and thus the intial conditions varied a little. But note that even small initial variations can cause big changes in the whole deployment.

3.6.5 Digitizing one Test Run

In order to compare the simulation with the reality, one test run had to be digitized. Run 6 was chosen to be further investigated because its deployment time was nearest to the average (see table 3.8).

The single steps to gain digitized values of the panel deployment were:

- Recording the deployment with a semi-digital movie camera.
- Capturing the video from the digital video cassette (analogue) to an uncompressed Audio Video Interlaced (AVI) - file.
- Cutting the video to the beginning and the end of the deployment.
- Exporting every frame of the video to a bitmap (BMP) file. In this case the edited video had 244 frames (30 frames/s).
- Loading every bmp-file into the program `Grafula3`[8]. After defining the axis, as shown in figure 3.29, the 6 reference points of the panels were selected, marked (see figure 3.31) and exported as data points in image coordinates (u,v).
- Transforming the 244×6 data points into the world coordinate system using (3.44)
- Calculating the angles of each panel.

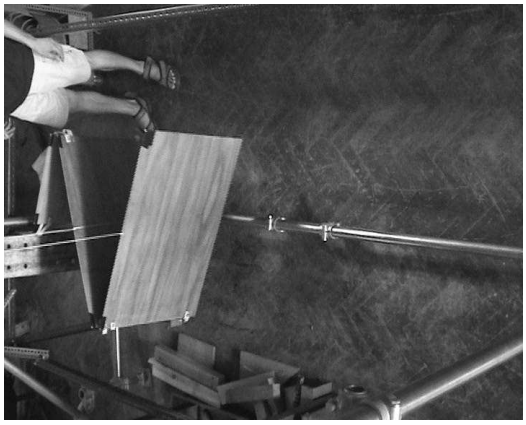

(a) the six reference points at each end of the three panels can hardly be seen

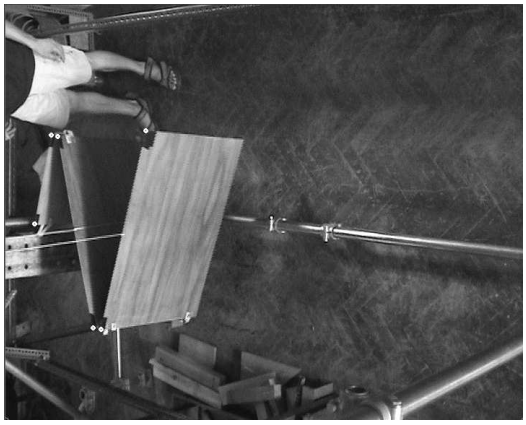

(b) the six reference points are marked and the image coordinates are exported

Figure 3.31: Example Frame 135 of the Test Run 6

The above described algorithm produces a digitized video of one test deployment. The frame rate of 30 frames per second guarantees a smooth movie.

In figure 3.32 the deployment of the experimental array is plotted. It can be seen that the panels first deployed to one side (0 s - 2.5 s). Afterwards panel 1 and 2 swung almost back (3 s - 4.5 s) to their initial positions. Then the panels took a zigzag-shape. The hinge lines latched almost at the same time: first H_1 (7.70 s), then H_2 (7.87 s) and finally H_3 (8.11 s). Figure 3.33 shows the relation between the panel angles and the deployment time. The deflection of θ_2 at $t = 0.3$ s is caused by errors during the digitizing process.

[8]Grafula3 v2.10 programmed by WESiK SoftHaUs is a freeware to digitize arbitrary graphs or pictures

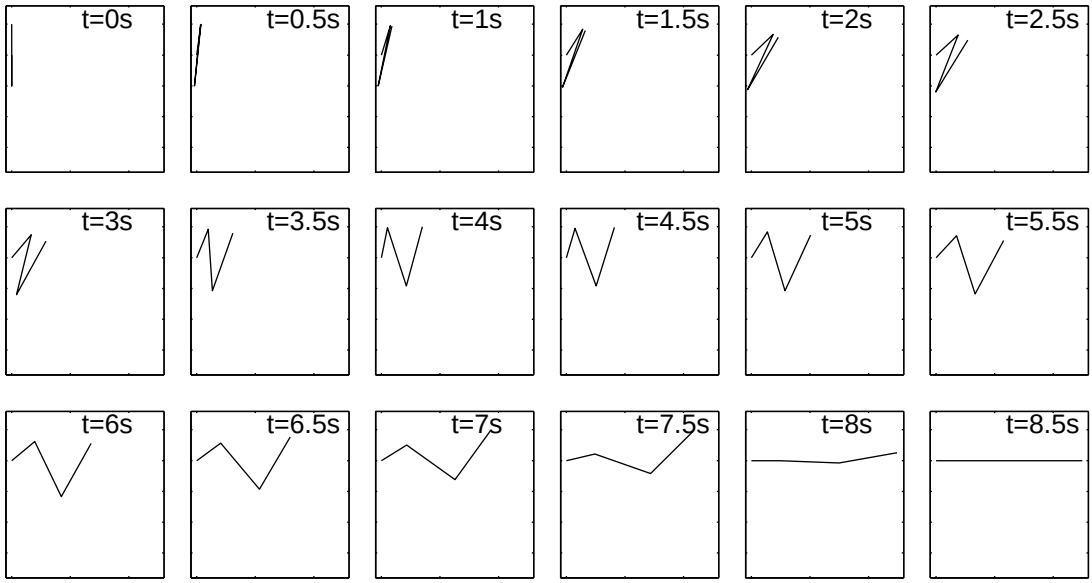

Figure 3.32: Deployment of the Test Panel — Using Digitized Experimental Data

3.6.6 Digitizing Errors

The values found above for the angles of the panels during the deployment, were achieved by selecting points out of bitmap images, transforming these coordinates into world coordinates and calculating the angles. In this section, the error of the angle calculation caused only by incorrect selection of the image points is investigated.

The error of the world coordinates is

$$\Delta x = \left|\frac{\partial}{\partial u}x(u,v)\right|\Delta u + \left|\frac{\partial}{\partial v}x(u,v)\right|\Delta v$$
$$\Delta y = \left|\frac{\partial}{\partial u}y(u,v)\right|\Delta u + \left|\frac{\partial}{\partial v}y(u,v)\right|\Delta v$$

where the maximum error of the bitmap coordinates is $\Delta u = \Delta v = 1$. The calculation of the panel angles uses two points (x_1, y_1) and (x_2, y_2).

$$\theta = \arctan\frac{y_1 - y_2}{x_1 - x_2}$$

The error of the panel angle is

$$\Delta\theta = \left|\frac{\partial}{\partial x_1}\theta(x_1\ldots y_2)\right|\Delta x_1 + \left|\frac{\partial}{\partial x_2}\theta(x_1\ldots y_2)\right|\Delta x_2 + \left|\frac{\partial}{\partial y_1}\theta(x_1\ldots y_2)\right|\Delta y_1 + \left|\frac{\partial}{\partial y_2}\theta(x_1\ldots y_2)\right|\Delta y_2.$$

In figure 3.34 the errors of the three panel angles are plotted. The errors are quite small. The highest value is less than 2°. The errors of the mapping were estimated to be maximal twice as high as the the calculated selecting errors. The total error can thus be estimated as:

$$\Delta\theta < 6°.$$

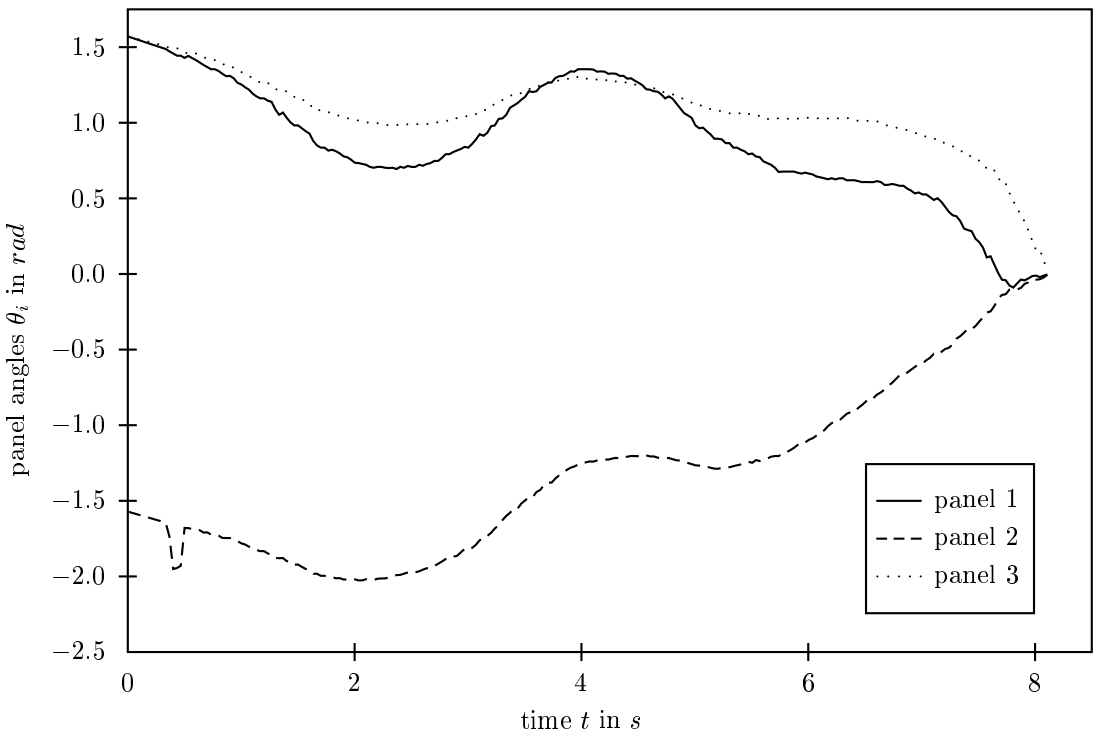

Figure 3.33: Panel Angles vs. Time during the Deployment of the Test Panel

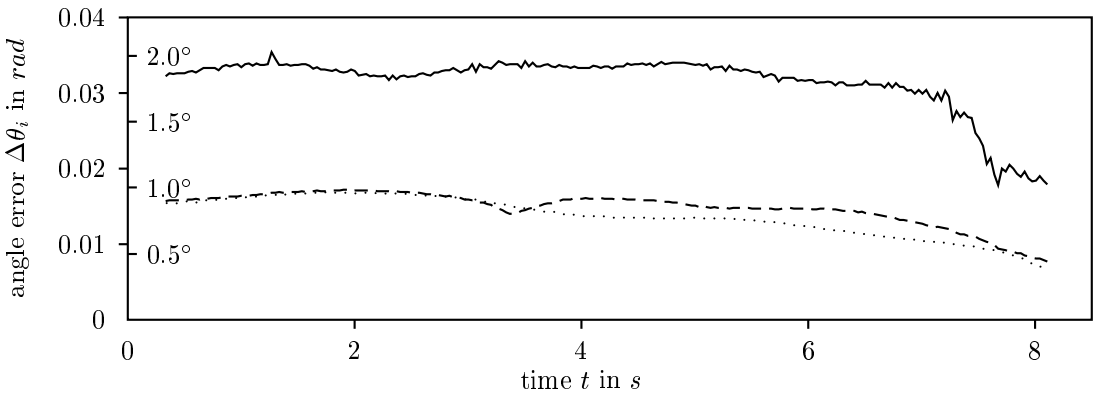

Figure 3.34: Error of the Panel Angles vs. Time during the Deployment of the Test Panel; Mapping Errors Not Taken Into Account

3.7 Comparison of Simulation and Experiment

In the previous two sections the results of the simulation and experimental measurement of the array deployment with a ORSS were presented. Now the two results are compared.

The predicted deployment time (7.770 s) is very close to the average deployment time of the experiment (7.870 s), see table 3.8. This is equivalent to a relative deviation of 1.27%.

For further comparison the test run 6 (see section 3.6.5) was used as the experiment reference.

The deployment time (8.141 s) is equivalent to a relative deviation of 4.17%. The single latching times are listed in table 3.9.

	latching times in s of		
	H_1	H_2	H_3
simulation	6.945	6.995	7.770
experiment	7.674	7.808	8.108
stddev.	-9.50%	-10.41%	-4.17%

Table 3.9: Comparison of the Latching Times of the Deployment of the Test Array on Ground

In fig. 3.35 the deployment of the test panel predicted from the simulation (solid line) is plotted versus the results from the experiment (dashed line). In the first 2.5 s both cases have a similar behaviour. In the time from 3 s to 4 s one can see that the simulation predicts a bigger swing back. The main difference afterwards is that panel 3 is predicted to move in the negative y-region, while in the experiment an almost symmetric shape was preserved.

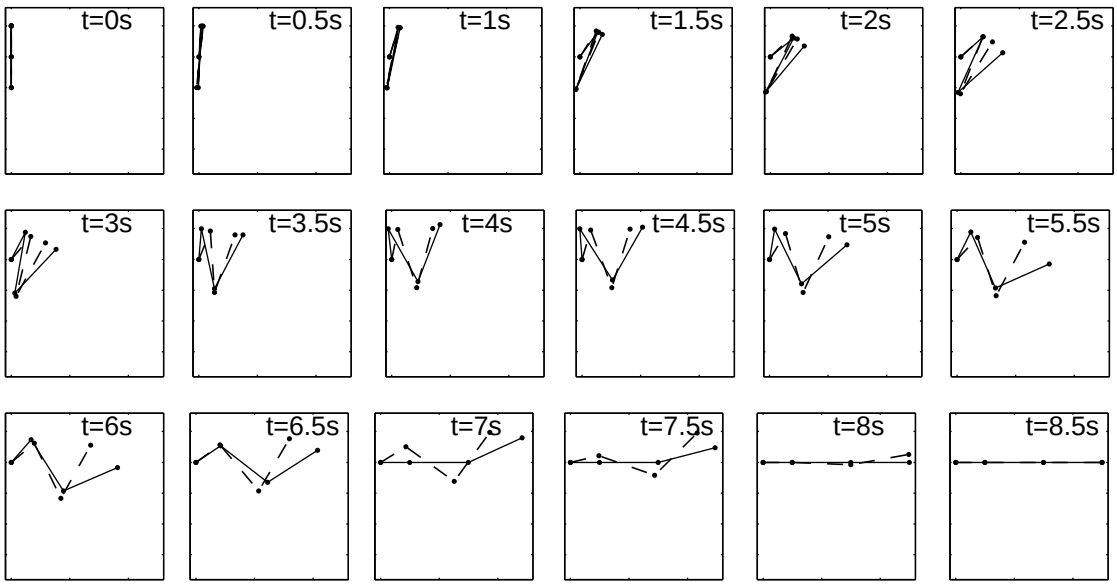

Figure 3.35: Comparison of the Deployment Results from Simulation (solid line) and Experiment (dashed line)

Because the deployment times are different, it is interesting to scale the simulation times in such a way that the deployment times match. The result is shown in fig. 3.36. It must be mentioned that the simulation results of panel 1 and panel 2 correspond very well with the experiment. The prediction for panel 3 however has some inaccuracy.

The overall result is satisfying. The main requirements were met: On one hand the deployment behaviour (latching sequence) was predicted very well, and on the other hand the predicted deployment time was within 10% of the experimental result.

Hence the simulation can be used to predict the deployment of the SSTL Array.

3.8 Simulation of SSTL Array and Conclusions

After it was proven that the simulation describes the reality quite well, simulations for the SSTL array were carried out.

Two different scenarios were investigated. First, the array was pushed with a spring release mechanism, and second, no initial energy was given to the system. For both scenarios the deployment

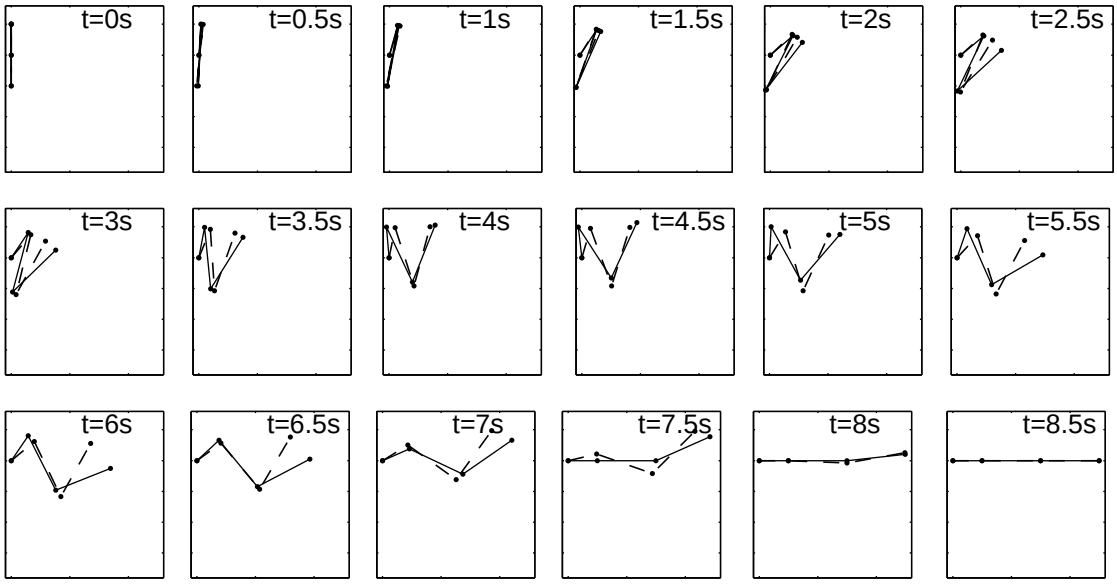

Figure 3.36: Comparison of the Deployment Results from Simulation (solid line) and Experiment (dashed line), Simulation Results Scaled in Time

in space and on earth with the one-rail suspension system were simulated. The results can be seen in figures A.6 - A.9.

With the initial energy of 0.1 J from the release spring, the deployment in space and on earth would last approximately 8 s. Both simulations are similar in the fact that the excursions are rather small. On ground the panels have a quite regular zig-zag shape throughout the deployment. All three hinge lines latch at almost the same time. In space the hinge-locking behaviour is different. First the root hinge gets latched, and 2 seconds later H_3. After one more second the deployment finishes with the latching of H_2.

The predictions for the deployment in space and on earth without initial energy vary in their overall performance. In space the whole array structure moves to the negative y-area. The maximal excursion is almost three times as high as on the ground. The deployment time on the ground is 28% higher than in space. This is especially caused by the behaviour that occurs in the first 8 seconds. One can recognize a rotation of the whole array around the root hinge without any significant deployment. This is probably caused by higher friction between trolley and rail.

Conclusions on the One-Rail Suspension System

Because of the character of the one-rail suspension system the zig-zag shape seems to be a natural configuration for the panels. Symptomatic also is the oscillating of the panels' centres around the x-axis, which is caused by the restoring pendulum forces.

It was concluded that the one-rail suspension system restricts the motion of the array too much in the direction perpendicular to the rail. It was therefore decided that it should not be used for ground tests of the SSTL array. In the next attempt, a four-rail suspension system is analysed.

Chapter 4

Four-Rail Suspension System

4.1 Description of Four-Rail Suspension System

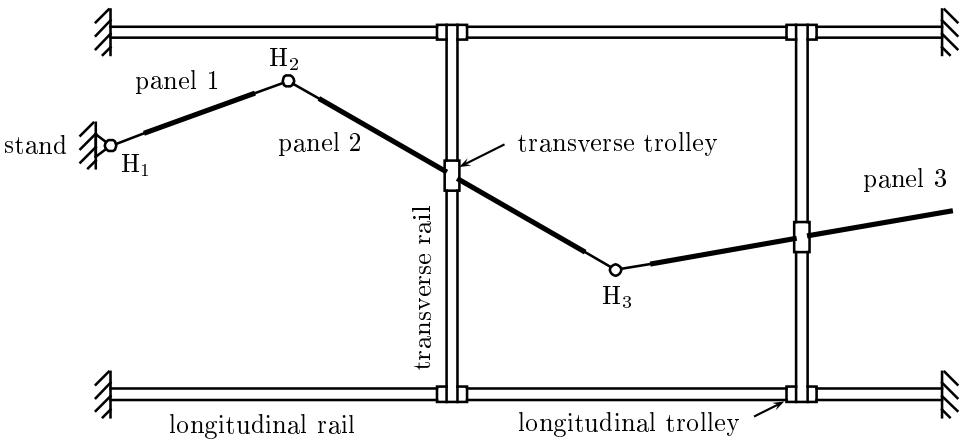

Figure 4.1: The Four-Rail Suspension System; view of the x-y plane

Using a four-rail suspension system shall ensure a space-like behaviour. The decisive difference from the one-rail suspension system is that the trolleys now have two degrees of freedom each.

In figure 4.1 the new suspension type is schematically drawn in the x-y plane.

The array is suspended at 3 points, again. Panel 1 is connected via hinge line H_1 to a stand, which represents the connection to a spacecraft. Panel 2 and 3 are both suspended on their centres of gravity and connected to one transverse trolley in each case. A transverse trolley can move on a transverse rail in the y direction. Under a transverse rail two longitudinal trolleys are fixed in such a way that they can move on two longitudinal rails in the x direction. The four-rail suspension system is supported by a scaffolding system. A spring release system shall be used in the experiments.

4.2 Description of Test Array

While for the one-rail suspension system a simple and cheap-to-produce test array was used, now the test panels shall especially meet the properties of the SSTL array. In particular, the dimensions

of the masses and of the mass moments of inertia shall be comparable and within a very small margin. This new test array shall be called SSTL Test Array. The main properties of the panels are summarized in table 4.1. It must be mentioned that the width (700 mm) is smaller than the corresponding one of the SSTL array (1000 mm).

panel	length [mm]	width [mm]	thickness [mm]	mass [kg]	moment of inertia [kg m^2]
1	500	variable	6	1	0.0208
2	1200	700	15	4.6	0.552
3	1200	700	15	4.5	0.540

Table 4.1: Properties of the Panels of the SSTL Test Array

For the panel material, Medium Density Fibre Board (MDF) was chosen. It has the necessary stiffness, is easy to machine and is available in different thicknesses. The two large panels were made of 15 mm thick MDF-plates. Assuming a density of $\rho_{MDF}^{15mm} = 0.739$ g/cm^3 the design for panel 2 can be seen in figure 4.2. Panel 3 has a very similar design, only the thickness of the outer frame was modified.

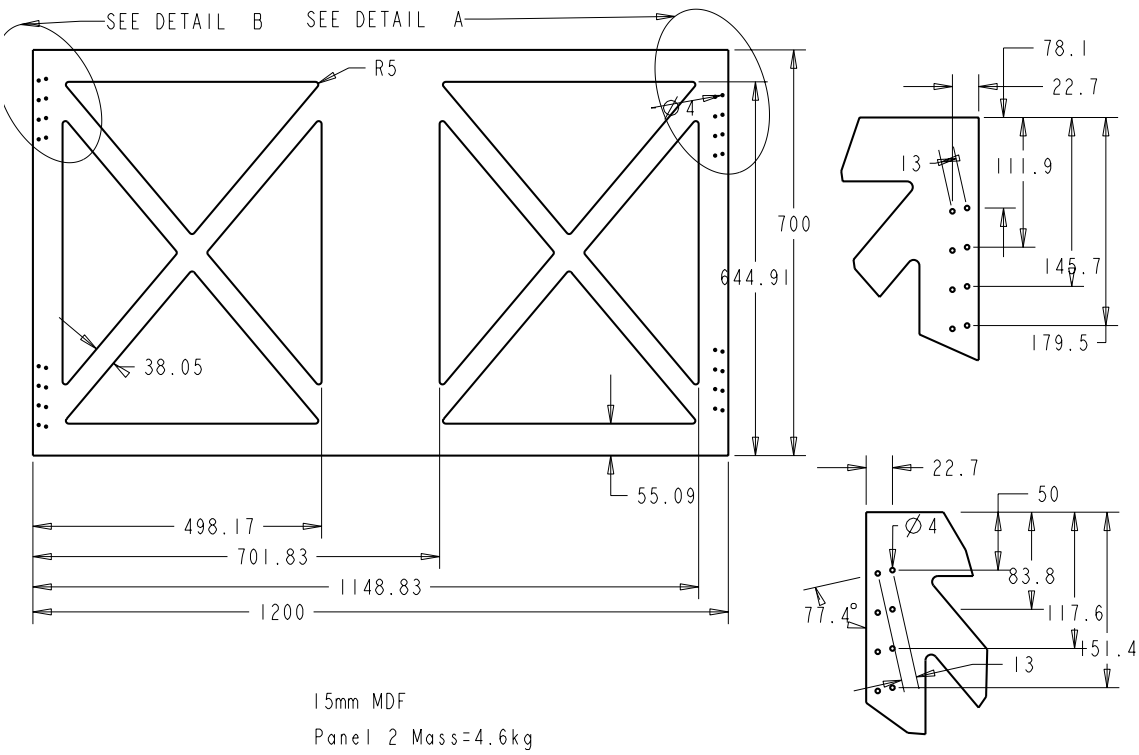

Figure 4.2: Design of Panel 2 of SSTL Test Array (prepared by A. Watt)

Panel 1 (yoke) was made of 9 mm thick MDF-plates ($\rho_{MDF}^{9mm} = 0.733$ g/cm^3). If a 15 mm thick sheet had been used, it would have been necessary to cut away a larger amount of material to maintain the mass and mass moment of inertia values. This would have decreased the stiffness to a critical state. A drawing of panel 1 can be seen in fig. 4.3.

The tape springs and the supports in the hinge lines were provided by SSTL. The mass of one tape spring and the associated supports is 15.3 g. For the connection between the stand and panel 1 only three tape springs are used, while the remaining two hinge lines are made of 4 tape spring in each case.

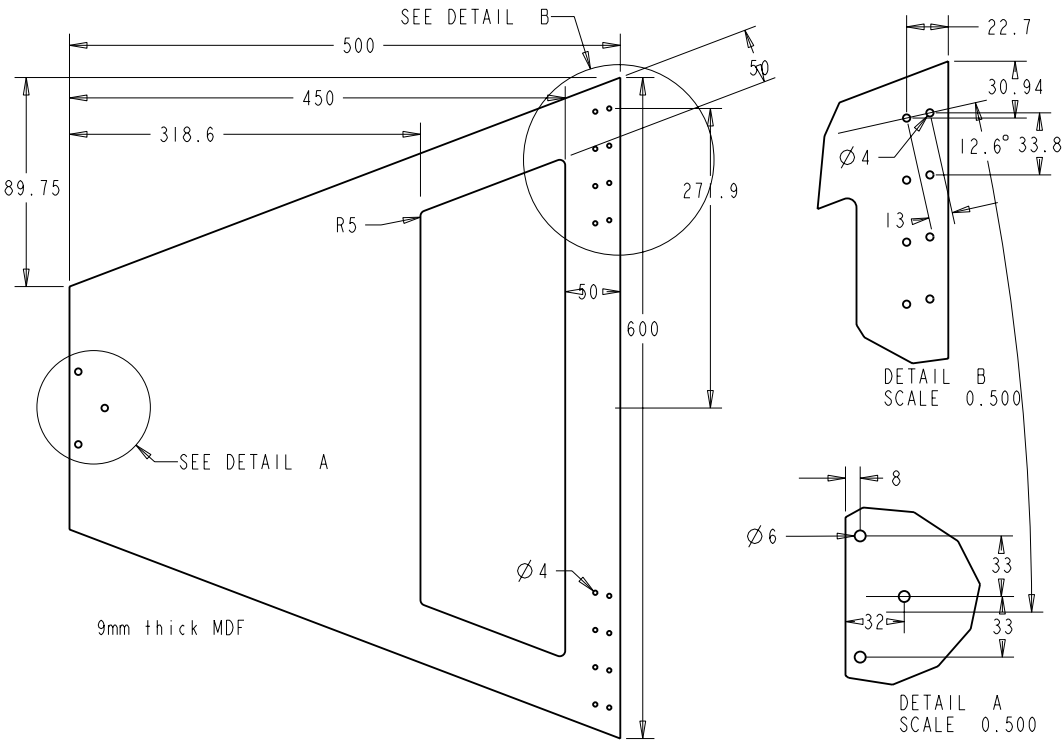

Figure 4.3: Design of Panel 1 of SSTL Test Array (prepared by A. Watt)

4.3 Simulation of Four-Rail Suspension System

4.3.1 Introduction and Notation

The deployment of the array suspended to the four-rail system can be mathematically described with the same tools as the one-rail suspension system (see 3.3). First the basic equation of motion will be derived (4.3.2) based on the results from 3.3.2. The possible constraints and their handling are the same as described in section 3.3.3. Equation (3.27) can be used again, although the physical background to latching is different. In section 4.3.3 the solution of this problem is explained. The initial value problem must also be modified slightly because the masses of the suspension system play a role, now, as described in 4.3.4

The position of the panels are described in the same way as in section 3.3 using the geometric variables $\theta_1 \dots \theta_3$ and the following parameters:

l	length of one big panel
s_p	separation distance between two panels
m_i	mass of the panel i
m_h	mass of the parts of one hinge line
M_{h0}	moment in one hinge line

The environment (space, earth) is represented by the gravity acceleration g. The initial conditions are determined by the potential energy of the release spring $E_{s,pot}$ given to the system.

The new suspension system shall be mathematically described with the following simplifications. The point of suspension on the panel shall have the same position in the x-y plane as the corresponding transverse trolley. The panels will be suspended almost directly under the trolleys.

The (very small) length of the suspension string is not crucial any more. The contact between a transverse trolley and its transverse rail is affected by friction. Friction also occurs between the longitudinal trolleys and rails. Because the material of the transverse rails can be different from that of the longitudinal rails, two different coefficients of friction must be considered. The suspension parameters are:

m_t	mass of one transverse trolley
m_r	mass of one transverse rail and the two appendant longitudinal trolleys
μ_x	coefficient of friction between longitudinal rail and longitudinal trolley
μ_y	coefficient of friction between transverse rail and transverse trolley

4.3.2 Basic Equation of Motion

The equation of motion is obtained again by using the principle of virtual work. The virtual work of the array $(\boldsymbol{W_h} + \boldsymbol{W_{\ddot{x}}} + \boldsymbol{W_{\ddot{\theta}}})$ dos not need to be re-derived as it is the same as in section 3.3.2. Additionally, the virtual work components due to

- translation of the transverse trolleys in the y-direction
- translation of the whole suspension system in the x-direction
- friction between transverse trolleys and rails (y-direction)
- friction between longitudinal trolleys and rails (x-direction)

must be considered.

Virtual Work due to Translation of Suspension System in the y-Direction

The transverse trolley is the only part of the suspension system which can move in the y-direction. With

$$\begin{aligned}\boldsymbol{x_{ty}} &= \begin{bmatrix} y_{(\text{trans. trolley 1})} \\ y_{(\text{trans. trolley 2})} \end{bmatrix} = \begin{bmatrix} 0 & 0 & 0 & 1 & 0 & 0 \\ 0 & 0 & 0 & 0 & 0 & 1 \end{bmatrix} \boldsymbol{x} \\ &= \boldsymbol{C_{16}}\, \boldsymbol{x}\end{aligned}$$

the d'Alembert force is

$$\boldsymbol{F_{\ddot{x}_{ty}}} = -m_t \boldsymbol{C_{16}}\, \ddot{\boldsymbol{x}} = -m_t \boldsymbol{C_{16}}\, (\boldsymbol{c_5} + \boldsymbol{C_4}\, \ddot{\boldsymbol{\theta}}).$$

The virtual displacement is

$$\delta(\boldsymbol{x}_{ty}) = \boldsymbol{C_{16}}\, \delta(\boldsymbol{x}) = \boldsymbol{C_{16}} \boldsymbol{C_4}.$$

Hence, one obtains for the virtual work:

$$\begin{aligned}\delta \boldsymbol{W_{ty}} &= -m_t \boldsymbol{C_4}^T \boldsymbol{C_{16}}^T \boldsymbol{C_{16}}\, (\boldsymbol{c_5} + \boldsymbol{C_4}\, \ddot{\boldsymbol{\theta}}) \\ &= -m_t (\boldsymbol{c_{31}} + \boldsymbol{C_{32}}\, \ddot{\boldsymbol{\theta}})\end{aligned} \tag{4.1}$$

Virtual Work due to Translation of Suspension System in the x-Direction

All the trolleys and the transverse rail have a translational degree of freedom in the x-direction have got. Introducing the vector of the x-positions of the trolleys/rails

$$\begin{aligned}\boldsymbol{x_{tx}} &= \begin{bmatrix} x_{(\text{trans. trolley 1})} \\ x_{(\text{trans. trolley 2})} \end{bmatrix} = \begin{bmatrix} 0 & 0 & 1 & 0 & 0 & 0 \\ 0 & 0 & 0 & 0 & 1 & 0 \end{bmatrix} \boldsymbol{x} \\ &= \boldsymbol{C_{19}}\, \boldsymbol{x}\end{aligned}$$

one can calculate the inertia forces and the virtual displacements

$$\boldsymbol{F}_{\ddot{\boldsymbol{x}}_{\boldsymbol{tx}}} = -(m_t + m_r)\boldsymbol{C_{19}}\,\ddot{\boldsymbol{x}} = -(m_t + m_r)\boldsymbol{C_{19}}\,(\boldsymbol{c_5} + \boldsymbol{C_4}\,\ddot{\boldsymbol{\theta}})$$
$$\delta(\boldsymbol{x}_{tx}) = \boldsymbol{C_{19}}\,\delta(\boldsymbol{x}) = \boldsymbol{C_{19}}\boldsymbol{C_4}.$$

The virtual work is then given by

$$\begin{aligned}\delta\boldsymbol{W_{tx}} &= -(m_t + m_r)\boldsymbol{C_4}^T\boldsymbol{C_{19}}^T\boldsymbol{C_{19}}\,(\boldsymbol{c_5} + \boldsymbol{C_4}\,\ddot{\boldsymbol{\theta}})\\ &= -(m_t + m_r)(\boldsymbol{c_{33}} + \boldsymbol{C_{34}}\,\ddot{\boldsymbol{\theta}})\end{aligned} \tag{4.2}$$

Virtual Work due to Friction between Transverse Trolley and Rail

The friction force between a transverse trolley and its transverse rail is caused by the weight of the panels and the weight of the transverse trolley. In section 3.3.2 the vertical forces in the suspension strings were calculated using a simple analysis. In equation (3.14) the forces have a component associated with accelerations in the z-direction. In the four-rail suspension system, however, there is only motion in the x-y-plane, and thus the normal forces on each transverse rail can be summarized in one vector, as follows:

$$\boldsymbol{F_{ny}} = \begin{bmatrix} F_{n,\text{trans.rail1}} \\ F_{n,\text{trans.rail2}} \end{bmatrix} = \begin{bmatrix} m_2 + 4/9\,m_1 + m_t \\ m_3 - 1/9\,m_1 + m_t \end{bmatrix} g$$

The resulting friction force is

$$\boldsymbol{F_{\mu y}} = \mu_y \begin{bmatrix} -\text{sign}(\dot{x}_4) & 0 \\ 0 & -\text{sign}(\dot{x}_6) \end{bmatrix} \boldsymbol{F_{ny}}$$

Corresponding to $\boldsymbol{F_{\mu y}}$, the virtual displacement is $\delta(\boldsymbol{x}_{ty})$ which has already been introduced in section 4.3.2. The virtual work is

$$\begin{aligned}\delta\boldsymbol{W_{\mu y}} &= [\delta(\boldsymbol{x}_{ty})]^T\boldsymbol{F_{\mu y}}\\ &= \boldsymbol{C_4}^T\boldsymbol{C_{16}}^T\mu_y\,g\begin{bmatrix} -\text{sign}(\dot{x}_4) & 0 \\ 0 & -\text{sign}(\dot{x}_6) \end{bmatrix}\begin{bmatrix} m_2 + 4/9\,m_1 + m_t \\ m_3 - 1/9\,m_1 + m_t \end{bmatrix}\\ &= \mu_y\boldsymbol{c_{35}}\end{aligned} \tag{4.3}$$

Virtual Work due to Friction between Longitudinal Trolley and Rail

There are two contacts between two longitudinal trolleys and the associated longitudinal rail. However, because of the linear relationship between the friction force and normal force, the two contacts can be handled like one contact. By this, one can first add the normal forces and multiply afterwards the result with μ, instead of calculating first the two friction forces and adding both to the total force of friction.

The normal forces (resulting from the weight of the array, trolleys and the transverse rails) on the longitudinal rails are

$$\boldsymbol{F_{nx}} = \begin{bmatrix} F_{n,\text{long.rail},1} \\ F_{n,\text{long.rail},2} \end{bmatrix} = \begin{bmatrix} m_2 + 4/9\,m_1 + m_t + m_r \\ m_3 - 1/9\,m_1 + m_t + m_r \end{bmatrix} g.$$

Similar to the previous section the virtual work is calculated, with the exception that the virtual displacement is $\delta(\boldsymbol{x}_{tx})$

$$\begin{aligned}\delta\boldsymbol{W_{\mu x}} &= [\delta(\boldsymbol{x}_{tx})]^T\boldsymbol{F_{\mu x}}\\ &= \boldsymbol{C_4}^T\boldsymbol{C_{19}}^T\mu_x\,g\begin{bmatrix} -\text{sign}(\dot{x}_3) & 0 \\ 0 & -\text{sign}(\dot{x}_5) \end{bmatrix}\begin{bmatrix} m_2 + 4/9\,m_1 + m_t + m_r \\ m_3 - 1/9\,m_1 + m_t + m_r \end{bmatrix}\\ &= \mu_x\boldsymbol{c_{36}}\end{aligned} \tag{4.4}$$

Total Virtual Work

The sum of all virtual works delivers the basic equation of motion

$$\boxed{\boldsymbol{M}\,\ddot{\boldsymbol{\theta}} = \boldsymbol{Q}} \tag{4.5}$$

with

$\boldsymbol{M} = \boldsymbol{C_7} + \boldsymbol{I_p} + m_t \boldsymbol{C_{32}} + (m_t + m_r)\boldsymbol{C_{34}}$

being the mass matrix; dependent on $\boldsymbol{\theta}$ and the constant system parameters

$\boldsymbol{Q} = -\boldsymbol{C_1}^T \boldsymbol{M_h} - \boldsymbol{c_6} - m_t \boldsymbol{c_{31}} - (m_t + m_r)\boldsymbol{c_{33}} + \mu_y\, \boldsymbol{c_{35}} + \mu_x\, \boldsymbol{c_{36}}$

being the load vector; dependent on $\boldsymbol{\theta}$, $\dot{\boldsymbol{\theta}}$ and the constant system parameters

4.3.3 Latching and Impulse

Because the suspension system is now almost directly connected to the panels it must also be considered when setting up the latching equations.

The physical laws are the same as described in section 3.3.4. The difference from the equations for the One-Rail System are the new properties of the masses. The masses of the suspension system can be thought as concentrated at the suspension points/centre of gravity of the two big panels. The modified matrix of the panel masses is

$$\boldsymbol{m_p^*} = \boldsymbol{m_p} + \begin{bmatrix} 0 & 0 & 0 & 0 & 0 & 0 \\ 0 & 0 & 0 & 0 & 0 & 0 \\ 0 & 0 & m_r + m_t & 0 & 0 & 0 \\ 0 & 0 & 0 & m_t & 0 & 0 \\ 0 & 0 & 0 & 0 & m_r + m_t & 0 \\ 0 & 0 & 0 & 0 & 0 & m_t \end{bmatrix} \tag{4.6}$$

In analogy with section 3.3.4 the latching equation is derived by replacing $\boldsymbol{m_p}$ by $\boldsymbol{m_p^*}$:

$$\boxed{\dot{\boldsymbol{\theta}}^a = \boldsymbol{B^*}\,\boldsymbol{S_M} + \dot{\boldsymbol{\theta}}^b} \tag{4.7}$$

with

$$\boldsymbol{B^*} = (\boldsymbol{C_{37}} - \boldsymbol{C_{30}}\,\boldsymbol{C_{28}}^{-1}\boldsymbol{m_p^*}\,\boldsymbol{C_4})^{-1}\,\boldsymbol{C_{29}}$$

and

$$(C_{37})_{ij} = (I_p)_{ij} + (C_2)_{kl}\,(C_3)_{lm}\,\delta_{mn}^{(i)}\,(m_p^*)_{np}\,(C_4)_{pj}$$

4.3.4 Initial Value Problem

The only difference from the one-rail suspension system is — like in section 4.3.3 — the different moving mass. By modifying the panel mass matrix to $\boldsymbol{m_p^*}$ (see (4.6)) the initial velocities change

$$E_{a,kin}^*(t=0) = \frac{\dot{\theta}_{20}^2}{48}\left[\left(8l^2 + 12ls_p + 6s_p^2\right)(m_2 + m_3) + \left(12l^2 + 24ls_p + 12s_p^2\right)(m_r + m_t) + \left(18l^2 + 18ls_p + 9s_p^2\right) m_h\right]$$

$$\dot{\boldsymbol{\theta}}(0) = \sqrt{\frac{48E_{s,pot}/l^2/(m_2+m_3)}{8 + 12\frac{s_p}{l} + 6\frac{s_p^2}{l^2} + \left(12 + 24\frac{s_p}{l} + 12\frac{s_p^2}{l^2}\right)\frac{m_r+m_t}{m_2+m_3} + \left(18 + 18\frac{s_p}{l} + 9\frac{s_p^2}{l^2}\right)\frac{m_h}{m_2+m_3}}}\begin{bmatrix}0\\1\\1\end{bmatrix} \tag{4.8}$$

4.4 Pre-Consideration on the Dimensions

The four-rail suspension system had to be designed. Especially the length of the transverse rails had to be assessed. The length of the transverse rails have an influence on the mass and thus on the deployment.

The simulation method in section 4.3 made it possible to predict the deployment. The starting point was the simulation for the space environment. The maximal excursion in the y-direction is approximately 0.5 m. As result of this, the length of the transverse rail was set to 0.6 m. Assuming that the same type of tubes would be used for the transverse rails and that the mass of one trolley is approximately 150 g, the mass of one transverse rail including the trolleys is $m_r = 2.5$ kg. The simulation delivered two important results: the maximal y-excursion was nearly 1 m, which means that the assumption of 0.6 m was wrong. Furthermore, the deployment stops, probably because the friction forces are too large.

Further sensitivity studies proved the logical assumption that the space deployment can best be repeated if the masses of the moving parts are designed to be as light as possible, and if friction is as small as possible.

Reducing the mass of the transverse rail was the first problem analysed. It was investigated for different types of rails, for example rectangular hollow bars with the longer edge in the vertical direction. It was then decided to continue using hollow tubes because of one significant reason. The circular cross-section of a hollow tube allows a trolley to rotate around the tube axis. The panel suspension point can move out of the plumb line and makes a slight correction by a trolley necessary. A fixed trolley — like in linear guide systems — cannot rotate and as a result much higher friction can be expected.

The chosen transverse rails consisted of extra thin hollow tubes with outer diameter of 40 mm and 1 mm wall thickness, made of stainless steel. This means a reduction of the mass per length by 72% compared to the normal tubes. The deflection of the midpoint of this tube with the length of 1 m under the force of 45 N was only 2 μm and hence not critical.

Simulation with this light-weight rail were carried out and showed a good conformance with the space deployment, concerning the positions and excursion of the panel (see fig. A.10). However, the deployment time is about 15 s which is almost double that predicted for space. This is especially caused in the last part of the deployment, after the latching of H_3 at $t = 9$ s.

Possible improvements to the simulation of the friction problem are shown in the following section.

4.5 Friction Experiments on Trolley/Rail-System

The first assessments of the deployment of the array using a FRSS showed that friction is the crucial point. Studies and experiments to investigate the friction levels, in section 3.4.2, were simple, though sufficient at that point. Now the friction must be further investigated and methods to reduce it must be found.

The aim of the experiments was to

- improve the methods of determining the coefficient of friction
- find the components which have the biggest influence on the friction, and
- reduce friction by improving these crucial components

4.5.1 Description of the Experiments

Two kinds of friction need to be investigated: the kinetic friction and the maximum appearing friction (static friction).

Friction is a result of relative movement between the rail and the trolley or the bearings, respectively. The amount of friction can be changed by using another rail or by modifying the bearings.

In section 3.4.2 the coefficients of static and kinetic friction were determined. Now, in order to investigate the influence of the rail, a machined rail was used. In a second experiment, hoping to achieve an additional improvement, the shields of the ball bearings were removed and the inside was cleaned. This included the removal of the grease, which was replaced by a low-friction oil. For both experiments the static and the kinetic friction were measured.

4.5.2 Methods of Testing

Kinetic Friction Experiments

In contrast to section 3.4.2 the coefficient of kinetic friction was not determined by measuring the force of friction. Instead, the trolley was accelerated by hand for a short distance (figure B.4-a) until it was released. Then the velocity of the trolley was determined at a specific point (figure B.4-b), and the distance from that starting point to the stop (figure B.4-c) was measured.

The advantage of this method is saving time for each test run. Furthermore, friction is not measured at each point of the rail but an average value of it is obtained. A final advantage is, that it is unimportant to know the normal force, because it is not used in the calculation.

An improvement was achieved by fixing the weights directly to the trolley frame instead of using a string. This leads to the fact that the weights don't have their own degree of freedom and disturb the result.

The initial velocity is calculated by using a plate on the trolley that cuts off the light beam of a photo-electric sensor, perpendicular to the rail. The light-beam cut-off plate was painted black to avoid disturbing reflections from other light sources like daylight. The width of this plate was

$$l_c = 3.06mm \pm \Delta l_c \qquad \text{with } \Delta l_c = 0.01mm.$$

The time t_c this plate cuts off the very thin light beam was measured using an oscilloscope. The error of measuring the cut-off time is a device-reading error. The velocity of the light-beam cut-off plate and thus of the trolley at the point of the sensors is

$$v_0 = \frac{l_c}{t_c}.$$

The distance from the sensors to the point the trolley stops moving l_r is measured using a simple ruler with the error $\Delta l_r = 0.1mm$.

Assuming a constant coefficient of friction for all places on the rail, the retardation must be constant too, hence

$$a = -\frac{v_0^2}{2l_r} = -\mu g$$

The equation to calculate the coefficient of kinetic friction is then

$$\mu_{kin} = \frac{l_c^2}{2t_c^2 l_r g}; \qquad \frac{\Delta\mu_{kin}}{\mu_{kin}} = 2\frac{\Delta l_c}{l_c} + 2\frac{\Delta t_c}{t_c} + \frac{\Delta l_r}{l_r} \tag{4.9}$$

Static Friction Experiments

In order to measure the static friction the same method as described in section 3.4.2 was used. The advantage of this method is that the static force for every single ball in the bearing and on an arbitrary long distance on the rail can be found. The disadvantage, e.g. compared to the method of applying an angle to the rail, is that each test lasts quite a long time, and the pulling velocity is not exactly constant.

4.5.3 Results and Evaluation of the Kinetic Friction Experiments

The coefficient of kinetic friction of the normal rail and uncleaned bearings has already been determined in section 3.4.2. For the experiments with the machined rail and the cleaned bearings three different normal forces were applied and 10 runs carried out for each normal force. The results are summarized in table 4.2 and 4.3.

	$F_n = 27.71$ N			$F_n = 47.33$ N			$F_n = 75.68$ N		
run	t_r [ms]	l_r [cm]	$\mu_{kin}/10^3$	t_r [ms]	l_r [cm]	$\mu_{kin}/10^3$	t_r [ms]	l_r [cm]	$\mu_{kin}/10^3$
1	28.0	53.1	2.293	33.5	47.9	1.776	45.5	32.8	1.406
2	26.5	58.1	2.339	30.0	57.3	1.851	40.5	40.3	1.444
3	36.0	30.9	2.383	36.5	44.3	1.617	38.0	48.0	1.377
4	26.0	59.9	2.357	40.0	35.4	1.685	40.0	46.4	1.286
5	43.0	28.8	1.792	35.5	44.8	1.691	33.5	56.6	1.503
6	31.5	43.2	2.227	38.5	38.5	1.673	29.5	60.8	1.804
7	39.0	33.3	1.885	47.5	29.9	1.415	47.5	34.2	1.237
8	37.0	34.8	2.004	30.5	57.2	1.795	42.0	42.3	1.279
9	34.5	35.7	2.246	30.0	53.5	1.982	41.0	42.6	1.333
10	25.0	51.9	2.943	29.5	56.6	1.938	35.0	52.6	1.481
average			2.247			1.742			1.415
rel. standard deviation			14.3%			9.5%			11.5%

Table 4.2: Results of the Kinetic Friction Experiment between Machined Rail and Uncleaned Bearings

	$F_n = 27.71$ N			$F_n = 47.33$ N			$F_n = 75.68$ N		
run	t_r [ms]	l_r [cm]	$\mu_{kin}/10^3$	t_r [ms]	l_r [cm]	$\mu_{kin}/10^3$	t_r [ms]	l_r [cm]	$\mu_{kin}/10^3$
1	66	23.8	0.921	43	48.5	1.064	60	29.1	0.911
2	49	38.0	1.046	67	24.9	0.854	47	42.3	1.021
3	45	41.4	1.139	47	43.8	0.987	39	55.5	1.131
4	38	56.6	1.168	61	27.7	0.926	50	35.8	1.066
5	52	32.4	1.089	35	61.3	1.271	54	32.5	1.007
6	47	41.5	1.042	41	52.8	1.075	43	47.6	1.085
7	36	59.9	1.230	38	56.2	1.176	41	49.4	1.149
8	48	39.5	1.049	45	33.5	1.407	75	20.7	0.820
9	52	33.4	1.057	52	37.9	0.931	43	48.7	1.061
10	38	56.9	1.162	39	57.2	1.097	75	20.3	0.836
average			1.090			1.079			1.009
rel. standard deviation			8.0%			15.7%			11.5%

Table 4.3: Results of the Kinetic Friction Experiment between Machined Rail and Cleaned Bearings

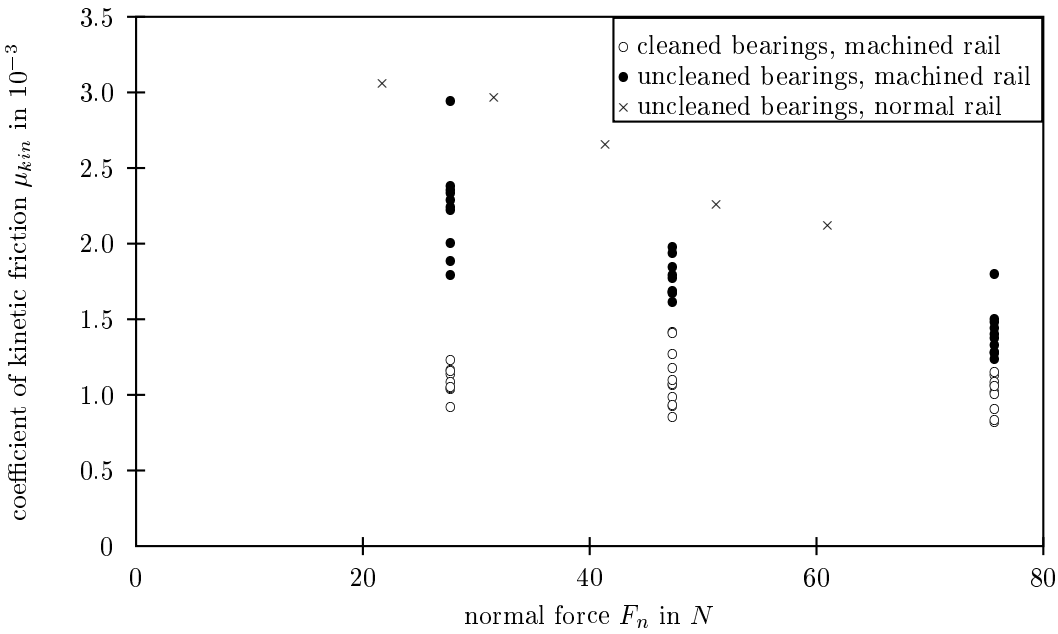

Figure 4.4: The Coefficient of Kinetic Friction for the Cases of Uncleaned/Cleaned Bearings and Normal/Machined Rail

The relative errors due to measurement as derived in (4.9) were in the range from 3.1% to 6.5%. The measurement method is therefore not too accurate. The biggest portion of the relative measurement error is caused by the too high inaccuracy of the time measurement.

In figure 4.4 the results of tables 4.2 and 4.3 are summarized and compared with results of section 3.4.2.

The following conclusions can be made:

- The usage of machined instead of normal rails decreases the kinetic friction by approximately 30%.
- The usage of cleaned instead of uncleaned bearings on a machined rail decreases the kinetic friction by 30% to 50%, depending on the normal force.
- Using cleaned bearings the coefficient of kinetic friction is constant, which means that the force of kinetic friction is directly proportional to the normal force.
- Using uncleaned bearings, the coefficient of kinetic friction increases with smaller normal forces. The model of direct proportional friction must be handled carefully.

4.5.4 Results and Evaluation of the Static Friction Experiments

The peaks of the friction force (similar to figure 3.23) were used to obtain results for the static friction. In figure 4.5 the coefficients of static friction (peak force of friction divided by normal force) are plotted. A clear difference between the cases of different rail/trolley properties like in figure 4.4 cannot be seen. In figure 4.6 the average values of the coefficients of static friction for each normal force are charted. The conclusions that can be drawn are:

- The coefficient of static friction can be reduced by cleaning the bearings and by using a machined rail.
- The coefficient of static friction increases with smaller normal forces.

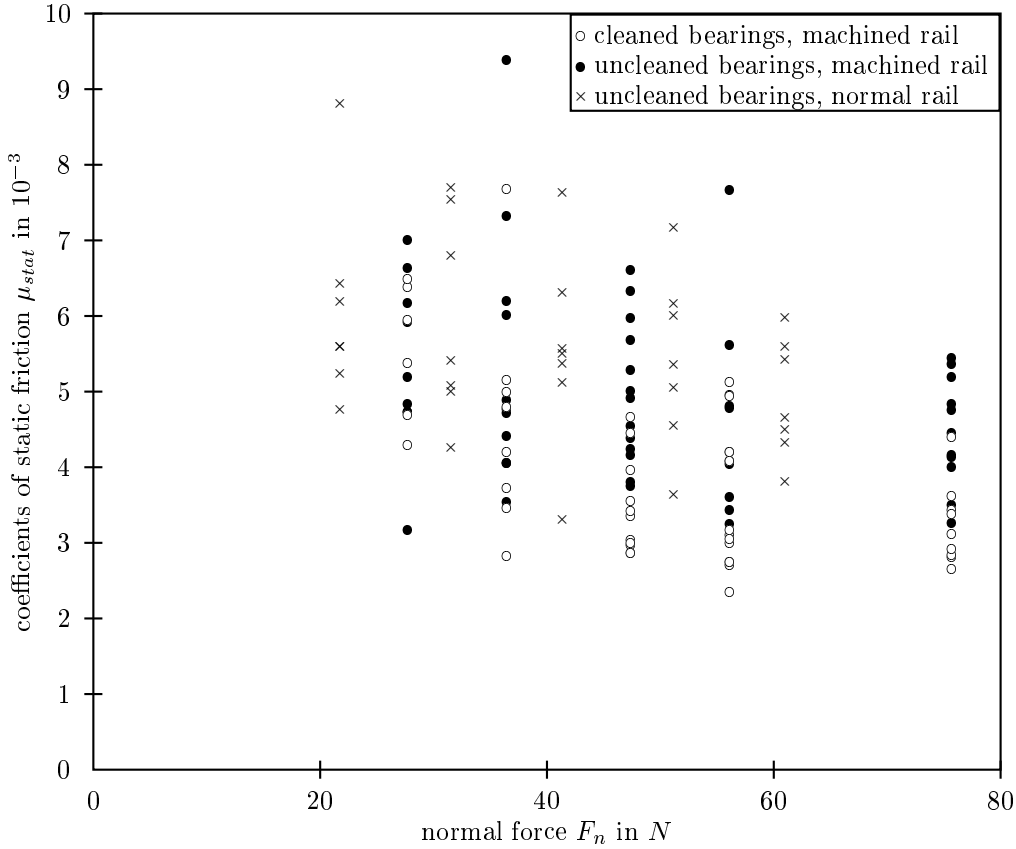

Figure 4.5: The Coefficients of Static Friction for the Cases of Uncleaned/Cleaned Bearings and Normal/Machined rail

4.5.5 Conclusions

From the results of the experiments it can be seen that the coefficient of static/kinetic friction is not constant for most cases. One would expect constant values from planar friction problems. In this specific case of contact between rotating bearings and a rail, one observation can be found: With decreasing normal forces the bearings seem to rotate less well and particular slide. Thus the coefficient of friction (force of friction divided by normal force) increases.

In order to reduce the disturbing influence of friction on motion it is recommended to clean the bearings and substitute normal tubs with machined tubes. For this case, the values of the

coefficient of static/kinetic friction can be given as a constant. It can be derived by using the mean value

$$\mu_{stat} = 3.892 \cdot 10^{-3} \tag{4.10}$$

$$\mu_{kin} = 1.009 \cdot 10^{-3} \tag{4.11}$$

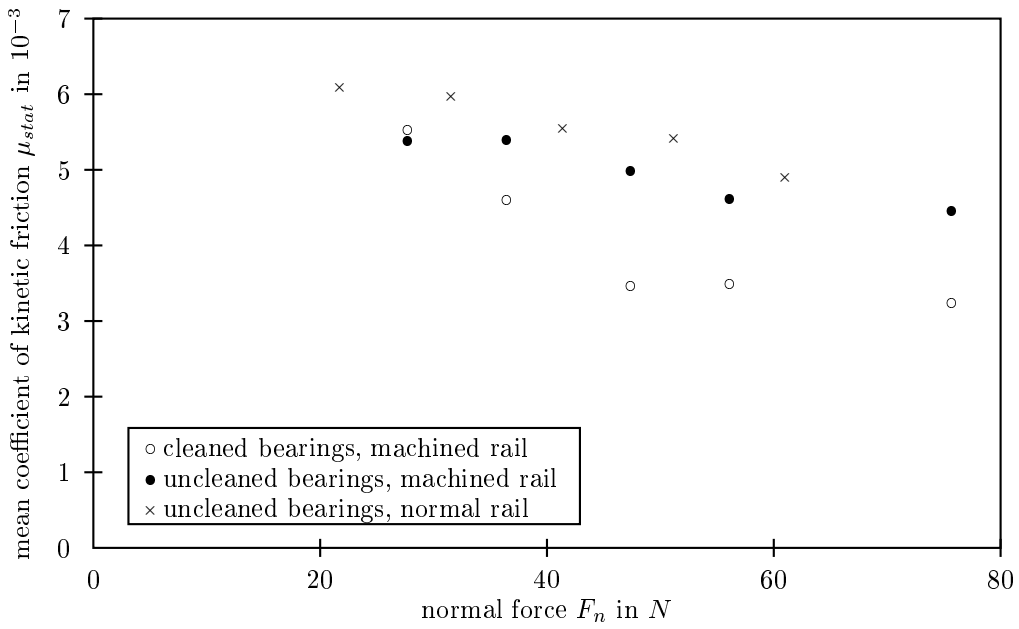

Figure 4.6: The Mean Coefficient of Static Friction for the Cases of Uncleaned/Cleaned Bearings and Normal/Machined Rail

4.6 Design of Four-Rail Suspension System

In this section, the results and statements from the two previous section were used to design the FRSS.

Transverse Rail

In order to reduce the mass of all moving parts, the transverse rail was made of an extra-thin hollow tube, as described in section 4.4. Each end of the tubes were treated with sandpaper to get a rough surface. That was necessary to glue the tubes to the longitudinal trolleys. The tubes are machined, in order to reduce friction. The following tabel gives a summary of the most important properties of one transverse rail.

length	outer diameter	wall thickness	mass
1008 mm	40 mm	1 mm	0.963 kg

Transverse Trolley

The transverse trolley had to be new-designed, because it moves on a tube with diameter 40 mm. A drawing of one transverse trolley is shown in fig. 4.7. It was made of aluminium. In order to

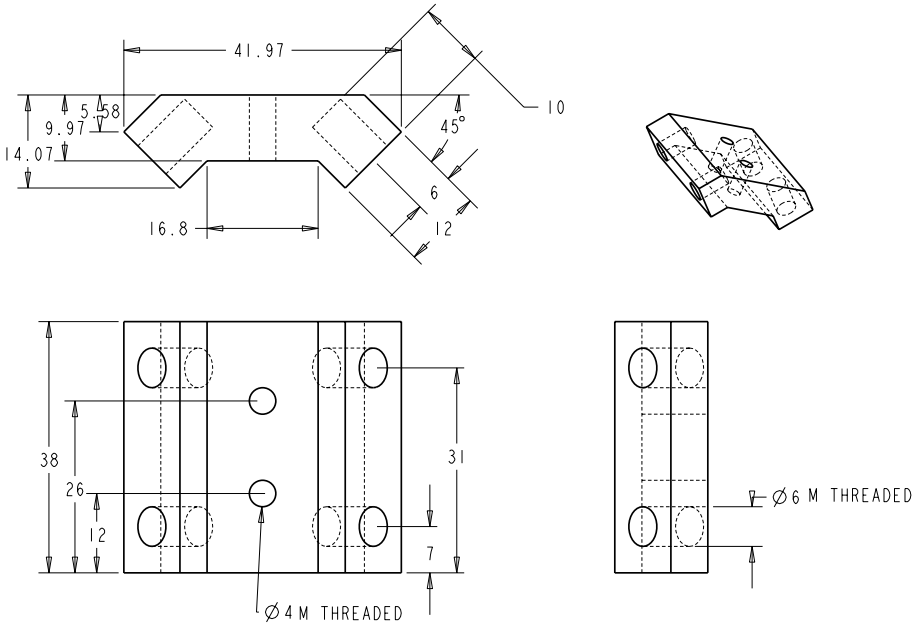

Figure 4.7: Drawing of Transverse Trolley, prepared by A. Watt

use the measured friction data, the same type of bearings as before was used. Four radial open bearings (bore diameter = 6 mm, outer diameter = 17 mm, width = 6 mm) were attached to the trolley with four bolts (M6×13). A washer was placed between trolley and bearings.

A frame was attached at the trolley again to ensure a rigid connection between trolley and panel around the tube. The frame is mounted at the trolley with to M4 bolts.

The mass of one transverse trolley, including bearings, frame, bolts and washers was

$$\begin{aligned} m_t &= m_{\text{trolley}} + m_{\text{frame}} + m_{\text{bearings}} + m_{\text{bolts and washers}} \\ &= 37\text{ g} + 45\text{ g} + 21.7\text{ g} + 31.3\text{ g} \\ &= 135\text{ g} \end{aligned} \tag{4.12}$$

Longitudinal Trolley

For the longitudinal trolleys a new design had to be created (see fig. 4.8). The trolley has to carry the transverse rails. Resulting from this, the upper surface was curved, in order to give the rail an additional support. The mass of one trolley is 42 g.

The transverse rail is connected to the longitudinal trolleys with glue (`Araldite`). The wheels of the trolley consist of the same type of bearings, see above. This leads to the mass m_r, introduced in 4.3.1:

$$\begin{aligned} m_r &= m_{\text{transverse rail}} + m_{\text{2 long. trolleys}} + m_{\text{bearings}} + m_{\text{bolts and washers}} + m_{\text{glue}} \\ &= 1275\text{ g} \end{aligned} \tag{4.13}$$

Connection between Trolley Frame and Panel

The panels are connected with the transverse trolley frame via a string. The lower end of the string is simply fixed in a hole of the panel with the means of a knot. The upper end is fixed in a

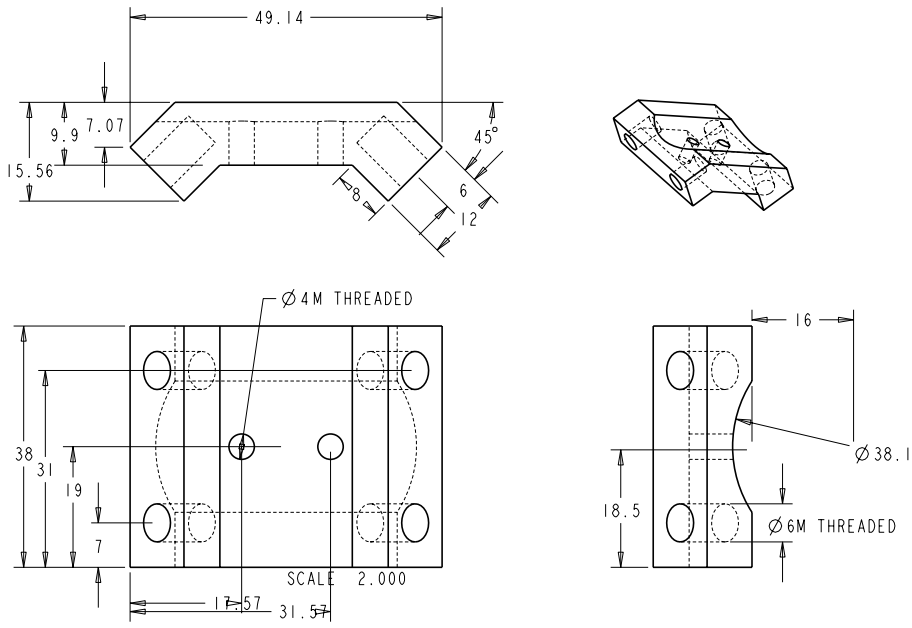

Figure 4.8: Drawing of Longitudinal Trolley, prepared by A. Watt

hole of a bolt. The bolt is movable in a nut, which again is fastened on the frame. This bolt/nut mechanism is necessary to adjust the vertical position of the panels.

Trolley/Rail Contact

The importance of low friction was recognized in 4.4. Solutions and suggestion of this issue were given in 4.5. In consequence, it was used only machined (ground) tubes. The bearings were cleaned. First the shield retaining snap wire and the shield itself were removed. With the means of high pressure air the balls and the cage of the bearing were cleaned from grease. Afterwards the balls were lubricated with oil. The difference between uncleaned and cleaned bearings can be seen in fig. 4.9.

The use of machined tubes and cleaned bearings assure low coefficients of friction

$$\mu_x = 0.001009 \tag{4.14}$$

$$\mu_y = 0.001009 \tag{4.15}$$

4.7 Prediction of Deployment/Sensitivity Studies

The values of the system parameters have been determined in section 4.2 and 4.6. Now, the deployment could be simulated. Figure A.11 repeats the behaviour in space, using the spring release system. The gound-based deployment is shown in figure A.12. One can recognize that the deployment time is greater than in space. In space the whole unfolding lasts 8.135 s, while on earth one can expect 10.915 s (+34%). The unfolding behaviour is, however, very similar. First H_1 gets latched ($t = 5.470$ s), then H_3 ($t = 7.755$ s), and finally H_2 ($t = 10.915$ s).

The values for the coefficient of friction and the moment in the hinge lines are determined with a certain inaccuracy. Sensitivity studies on these two parameters were carried out.

(a) uncleaned: grease is the reason for high friction

(b) cleaned: grease is replaced by oil

Figure 4.9: Uncleaned and Cleaned Bearing

First the influence on deployment time was investigated. In figure 4.10 the results are presented, when the friction coefficients are changed. It can be seen that with increasing friction in transverse direction (μ_y) the deployment time decreases. This can be explained by the fact that with higher transverse friction the excursions are smaller. By changing the longitudinal friction to higher values, the deployment time also increases.

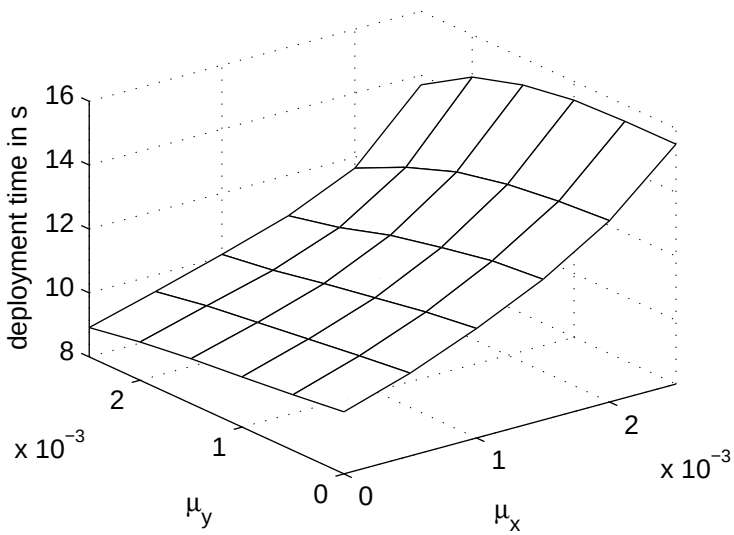

Figure 4.10: Predicted Deployement Time of SSTL Test Array on Earth, Sensitivity on Friction

The influence of the hinge-moment on the deployment time is almost linear (see figure 4.11). With increased moment the deployment time decreases, but the changes are rather small.

Second, the maximum excursion of the panel centres was inspected. One can draw three simple conclusions. The maximum excursion increases with increasing longitudinal friction μ_x, with decreasing transverse friction μ_y (see figure 4.12), and with increasing moment in the hinge-lines M_{h0} (see figure 4.13).

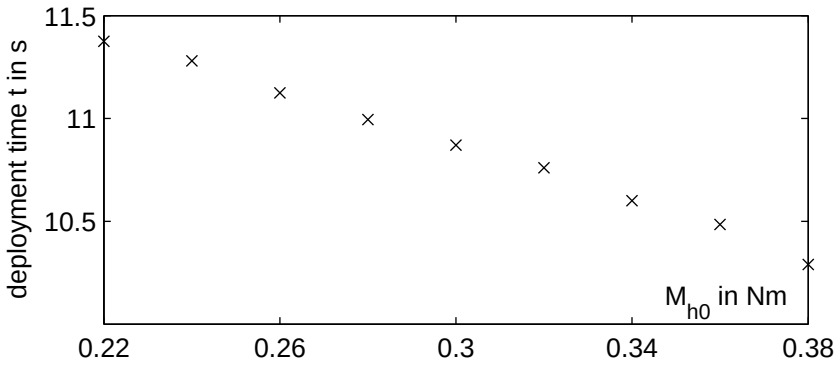

Figure 4.11: Predicted Deployement Time of SSTL Test Array on Earth, Sensitivity to Moment in Hinge-Line

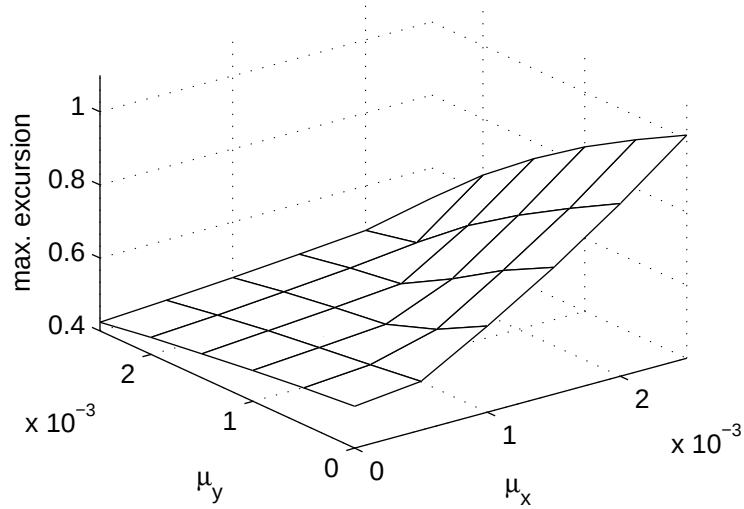

Figure 4.12: Predicted Maximum Excursion of Panel Centre of SSTL Test Array on Earth, Sensitivity to Friction

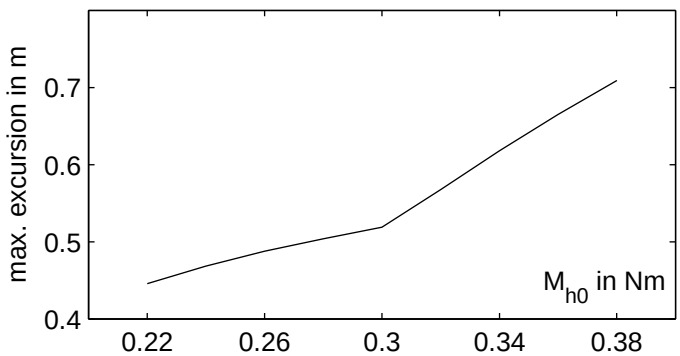

Figure 4.13: Predicted Maximum Excursion of Panel Centre of SSTL Test Array on Earth, Sensitivity to Moment in Hinge-Line

4.8 Deployment Experiment

Due to problems during deployment, the whole system had to be changed slightly.

In a first attempt, the deployment stopped after the latching of H_1. Two possible explanations were considered to be reasonable. Firstly, the moment in the panel-panel hinge lines might be too high. Secondly, there might be additional forces acting on the longitudinal trolleys due to violation of some of the assumptions about the contact with the longitudinal rails. As a result of this, the friction in the longitudinal direction may be higher.

In order to avoid an unsuccessful deployment, a higher initial energy was applied by using a longer spring. The initial energy was then $E_{s,pot} = 0.18$ Nm. Still, another problem existed which confirmed that the moment in the hinge lines may be smaller and/or the longitudinal friction higher: the deflection in transverse direction was so high that the transverse trolley touched the longitudinal rail. The solution of this problem was to reduce the number of tape springs in the root hinge to two.

The whole SSTL Test Array and the FRSS can be seen in figure 4.14.

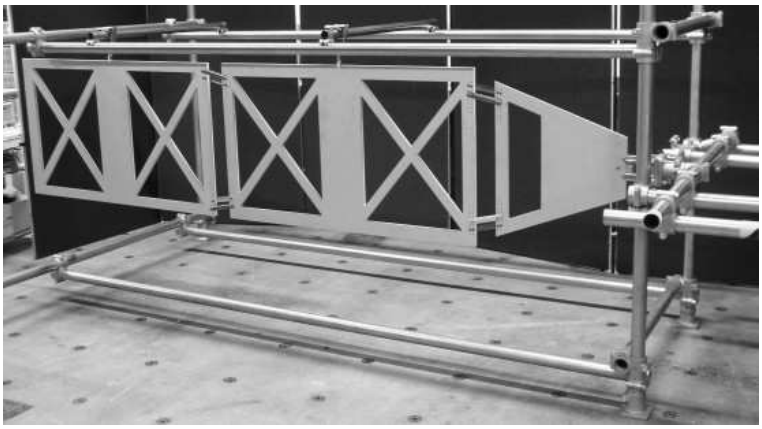

Figure 4.14: SSTL Test Array and the Four-Rail Suspension System

Description of Deployment Experiment

Before each test run, the array was folded to the initial position (see figure 4.15-a). Foam blocks were used as spacers between the panels. Panel 1 and panel 2 were held against end stops attached to the scaffold in such a way that the whole array was always set in the same initial position. Panel 2 was pressed against the Spring Pusher Mechanism (see figure 4.15-b) by means of a string. This string was tightened around the array. The deployment of the array was started by burning the string.

The deployment process was recorded with a film camera. The calibration of the camera was done in the same way as described in section 3.6.2 and 3.6.3. In total, 10 test runs were carried out. The first one showed large deviations from the others and thus was not taken into consideration.

Results of Deployment Experiment

The latching times of the test runs are summarized in figure 4.16. It can be seen that the results are repeatable. The latching sequence is always the same, and even the latching times are very similar. Only the deployment time (latching time of H_2) has a higher relative standard deviation.

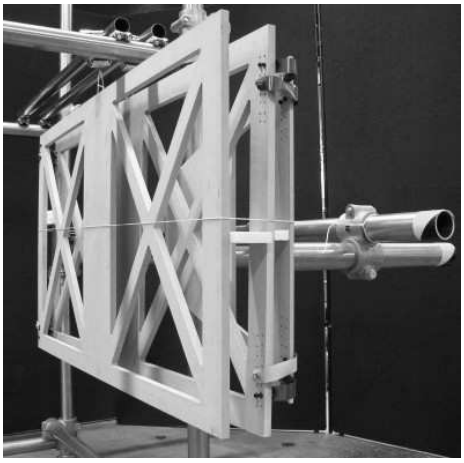

(a) SSTL Test Array in Initial Position

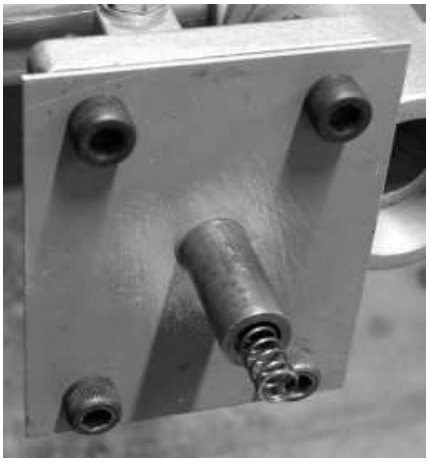

(b) Spring Pusher Mechanism

Figure 4.15: SSTL Test Array in Initial Position and the Spring Pusher Mechanism

test	latching time in s of		
run	H_1	H_3	H_2
2	6.79	10.65	12.93
3	6.89	10.75	12.23
4	7.20	11.24	11.65
5	6.73	10.87	13.56
6	6.68	10.98	12.52
7	7.19	11.52	13.17
8	6.98	11.28	12.92
9	7.06	11.16	12.77
10	6.54	10.85	14.22
average	6.90	11.03	12.89
rel stddev	3.3%	2.6%	5.8%

(a) tabular summary

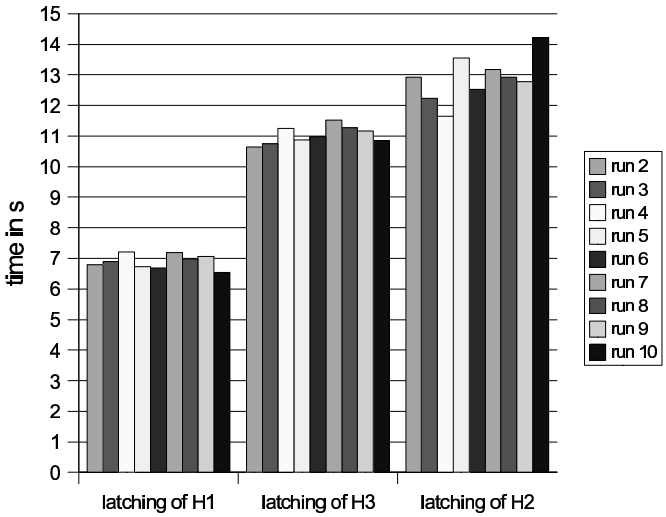

(b) chart

Figure 4.16: Latching Times of all Test Runs

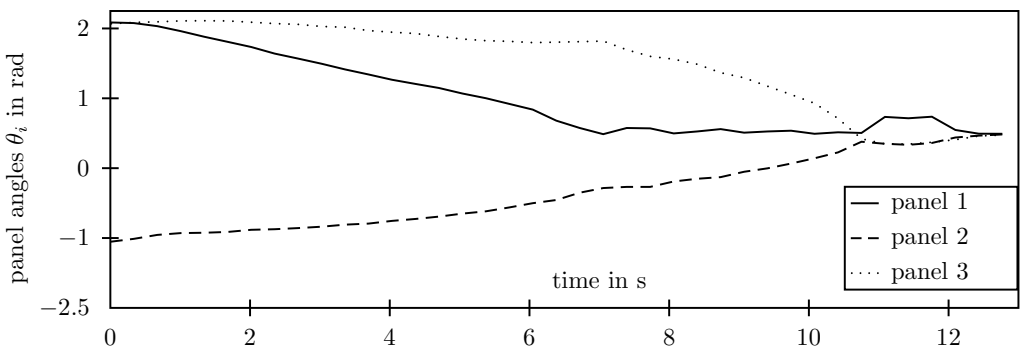

Figure 4.17: Panel Angles versus Time

Test run 3 was chosen for further investigation because it most closely represented the average behaviour. In analogy to section 3.6.5, the video was transformed into digital data. Figure 4.17 shows the panel angles versus time. It can be seen that the yoke hinge (H_1) gets unlocked at the moment when H_3 gets latched. The same incident can be observed in figure A.13 where the deployment of test run 3 is plotted.

4.9 Comparison of Simulation and Experiment

Due to the changes of the total experimental set-up, a new simulation had to be run.

The simulation was improved in the meantime. The constant moments of the hinge lines were replaced by moment-angle distributions. The moment distribution for the connection between two panels with rotated tape springs is plotted in figure 4.18. A different moment function was used for the root hinge.

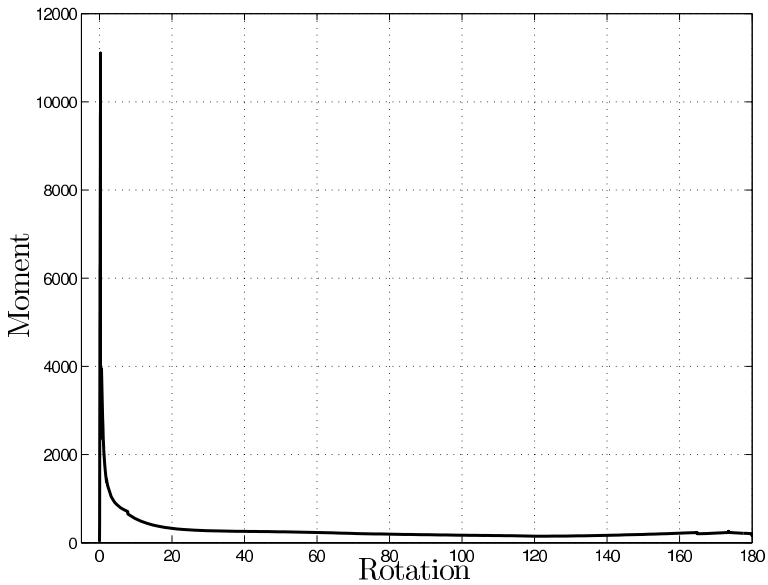

Figure 4.18: Moment (in Nmm) – Rotation (in degrees) Properties of Panel-Panel Hinge Line, Results from FE-calculation, prepared by A. Watt

The simulation with the standard parameters did not show perfect agreement. The initial motion is simulated quite well. The predicted latching time of H_1 is 6.570 s (-4.7%). The latchings of H_2 and H_3 happened within a short time (9.02 s and 9.66 s). This means that the predicted deployment time is 25% smaller than the experiment.

It was already mentioned that a reason for this difference could be incorrect values for the moment in the hinge lines and the friction. In sensitivity studies it was attempted to fit the simulation to the experiment. With 75% of the moment in the hinge lines and 125% of the longitudinal friction a simulation was run. All latching times were now within a margin of 8%. Both deployments, the experimental and the predicted, are plotted in figure 4.19.

In this figure, one can also recognize three other possible reasons for the discrepancy between experiment and simulation. First, in the experiment there is an initial rotation of panel 3. This could be caused by the fact that in reality the two transverse trolleys are pressed against each other and work like a spring. This would lead to a larger excursion of this panel 3, resulting in a longer deployment time.

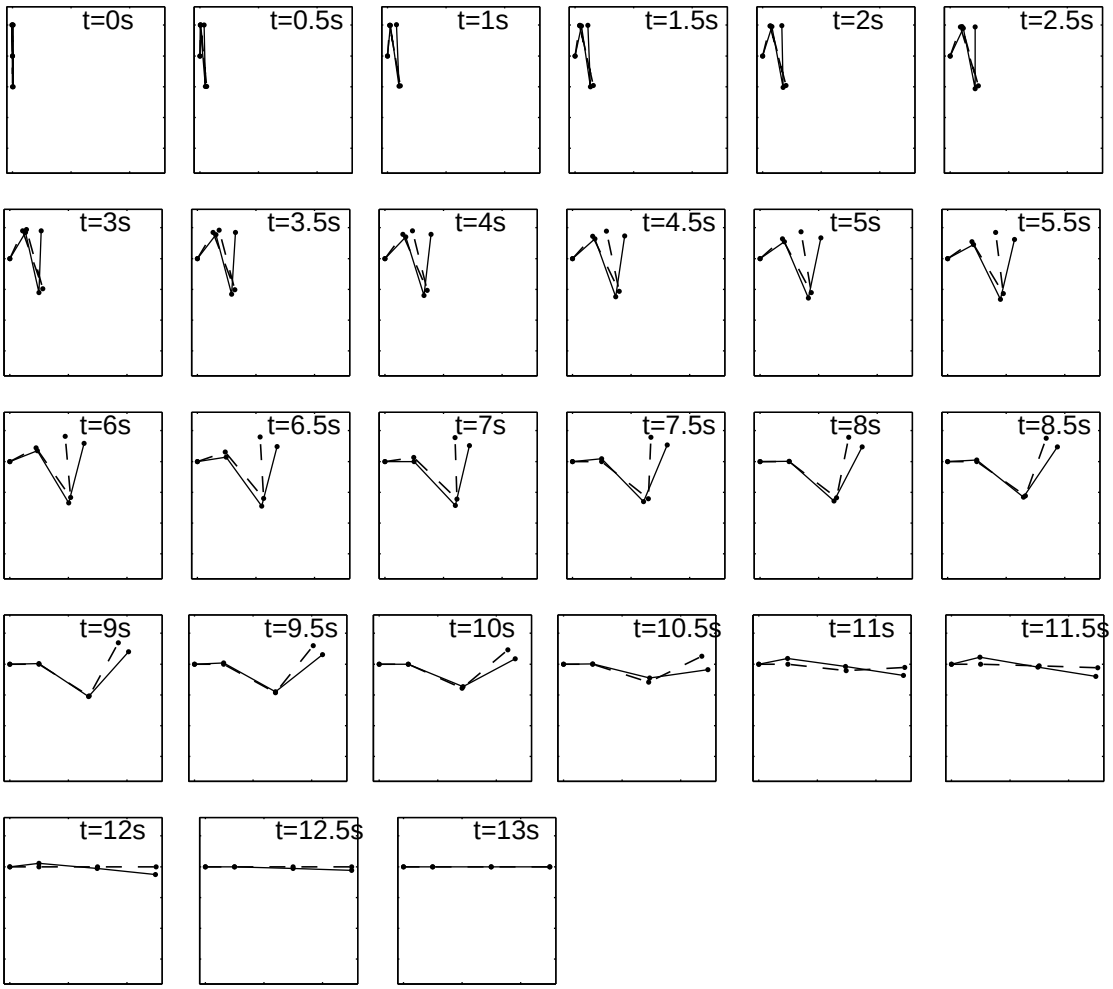

Figure 4.19: Deployment of SSTL Test Array, Test Results (solid line) versus Corrected Simulation Results (dashed line)

Second, the latching does not happen perfectly. There is a loss of energy. Furthermore the position of the panels is not constant during the latching because the tape springs can change their shape. In the simulation however, the hinge lines were assumed to be fixed joints.

Finally, it was never investigated if the tape springs in a latched hinge line buckle when latching occurs at another hinge line. In reality this happened (see figure 4.19, $t = 11$ s).

Chapter 5

Conclusions and Future Work

Summary and Conclusions

Space components very often involve deployable structures. Example are deployable solar arrays for satellites. In order to prove the functionality and behaviour in space, ground tests must be carried out. The deployment of a solar array containing two panels and one yoke, and its gravity compensation was the subject of this diploma thesis.

Due to the array's size and deployment behaviour, it was decided already at an early stage to use a mechanical suspension system to compensate gravity effects. Beside its suitability, a mechanical suspension system offers simplicity, cost-effectiveness and ease of production and availability. The deployment motion of the array takes place in a plane. Resulting from this, one can create a rail/trolley system which provides 0g environment in horizontal directions.

The initial idea was to use a single rail with two trolleys which are connected via strings to the centres of the panels. Experiments and simulations corresponded with each other and showed the same deployment behaviour: The motion is strongly restricted by pendulum restoring forces. The panel centres mainly oscillate around the position of the rail. The deployment behaviour on ground is therefore very different to the space behaviour where one expects greater excursions of the panel centres.

The deployment experiments did not deliver not very repeatable results. This was mainly caused by the simple release system. However, the relative standard deviation 8.7% of the deployment time is still acceptable. The deployment sequence was digitized by recording with a digital movie camera. Points on the panels in the image coordinate system were evaluated and transformed into world coordinates. The whole digitizing process gave the positions and orientations of the panels to every point of time. It was estimated that the maximum relative error of the panel orientation was 6%. Therefore this method is quite accurate. However, the big disadvantage is the high time exposure to obtain the data.

The simulation considered the panels and yokes as rigid bodies which are connected via joints. The tape springs were modelled with rotational springs. The friction between trolley and rail was difficult to simulate because the associated normal forces were hard to assess. With all the assumptions and with the help of the principle of virtual work, the equation of motion of the system was found. The appearance of latching and theoretical penetration of the panels had to be considered when solving the equation of motion. Therefore constraints were applied to the equation of motion. In order to solve the whole deployment motion, a complex program was written in `Matlab`. The program can output videos of the deployment or write position and orientation of the panels at every time into a file.

The simulation made further tests necessary to determine the coefficient between tube and trolley

on the one hand, and the moment in the hinge lines due to bending of the tape springs on the other hand.

The comparison with the experimental data showed that the simulation reproduces the reality quite well. The deployment behaviour was repeated very accurately. The average experimental deployment time was only 1.3% higher than the deployment time of the simulation. The latching times, however, were within a margin of 11%. Still, the use of a constant moment in the hinge lines and the not very accurate knowledge about the forces in the suspension strings – and therefore about the friction forces – are weak points in the simulation.

The use of a one-rail suspension system was found to be not suitable enough for this specific deployment problem. The motion on earth is excessively constrained by the suspension strings. However, it must be mentioned that this compensation system is very simple and contains only few moving parts. Although the kinematic constraints are large, the dynamic interference is small.

In a second and final attempt, a mechanical suspension system was used consisting of four rails. Two transverse rails move on two longitudinal rails. On each transverse rail one trolley can move perpendicular to the direction of the transverse rails. This system offers an almost unrestricted ability for the test article to move. In contrast to the one-rail suspension system, no kinematic restrictions appear, however the dynamic interference in greater.

Because of the greater moving mass of the suspension system, the deployment behaviour differs with respect to time very much from the space behaviour. This problem was solved on one side by designing light-weight tubes as transverse rails. The other side of the solution was to investigate the friction problem in greater detail. It was decided to clean the bearing of the trolleys and to use machined tubes. With these methods friction could be reduced by a factor of 2.

The simulation of the FRSS was realized by copying parts of the ORSS and modifying special parts. Sensitivity studies showed that the uncertain values of friction and moment in the hinge lines have a big influence of the deployment behaviour (deployment time and maximum excursions).

Deployment experiments were carried out in order to compare the simulation with the reality. A new experimental array was produced for this purpose. The properties of this array were very similar to the current specifications of the SSTL array. The experiments delivered very repeatable results, considering the latching times.

The experimental deployment behaviour is similar to the predictions. However, the simulation did not give a latching time within 10% of the measurement. The deployment time predicted from the simulation is 25% smaller than the experimental result. It was assumed that the values for the coefficients of friction and the moment in the hinge lines are not accurate enough. In sensitivity studies, both parameters were changed in such a way that prediction and experiment were within a margin of 8%. Finally it is interesting to note that the experimental deployment behaviour is similar to the predicted space behaviour, with regard to the configuration of the panels.

For the deployment of a solar array containing two panels and one yoke with the total length of 3.1 m, only a mechanical suspension system is suitable. A one-rail suspension system provides sufficient freedom only in one direction and therefore restricts the motion too much. The four-rail suspension system offers freedom of movement in every horizontal direction, but it interacts with the specimen due to its own dynamic properties. However, the FRSS seems to be the most suitable for this specific problem.

Future Work

In the time frame of this *Diplomarbeit* the first steps were carried out to design and investigate gravity compensation systems. A four-rail suspension system has been proposed, designed and realized, and it has been shown to work very well. Therefore the following suggestions for future work concern only the FRSS.

First, further deployment experiments of the SSTL test array must be carried out. It would be helpful to attach weights to the panels, or to use a different number of tape springs in one hinge line to get information about the sensitivity of the system. Very simple experiments like the excursion and release of only one panel could be carried out in order to measure the moment in the hinge lines and/or the friction.

The design of the FRSS can still be improved and optimized. In section 4.4 it was found that the mass of the movable suspension parts should be as small as possible. Especially reducing the length of the transverse rails can be considered. The use of a semi-circular tube instead of a full circular tube is another idea worth investigating. Yet another possibility to reduce the mass is to use another material, like CFRP. New friction tests would then be necessary. In addition to the transverse rails, the mass of the trolleys could also be reduced. The use of perspex instead aluminium and the utilization of smaller bearings could reduce the mass by approximately 20 g per trolley.

The other crucial point of the suspension system found in section 4.4 is the friction between the trolley and the tubular rail. Reducing it would provide an even better 0g condition. Although there is a minimum limit for friction it could be reduced by using different types or sizes of bearings.

A totally different approach to achieve better deployment behaviour – compared to the one in space – is the usage of an actively controlled suspension system. An example would be a support mechanism drive. Of course the whole suspension system becomes very complicated then, but very good 0g conditions can be created. For further studies in this direction, [6] provides some ideas and proposals.

The simulations of the deployment in the FRSS can still be improved. In particular three points could be investigated more carefully. Firstly, the whole array including the tape springs were considered to be rigid structures. The idealisation that the tape springs are modelled as joints should be changed. This means considering their correct kinematic behaviour. The flexible character of the panels should also be included in the simulation. Secondly, the forces in the suspension strings were only assessed. By determining them in separate tests, the normal forces and thus the forces of friction could be calculated more accurately. Thirdly, the impacts during a latching process must be investigated in order to predict the possible unlocking of the tape springs.

Although the FRSS seems to be the most suitable, the utilisation of air bearings should be closer investigated. Also, the ORSS should not be forgotten, because with longer suspension strings it could deliver satisfying suspension properties.

Bibliography

[1] http://esapub.esrin.esa.it/bulletin/bullet82/mes82.htm.

[2] http://www.me.uwaterloo.ca/~constrct/watflex.html.

[3] Auer, F. *Combined Electromagnetic Suspension and Propulsion for Positioning with Sub-Micrometer Accuracy.* PhD thesis, Delft University of Technology, 1995.

[4] CSA Engineering, Inc. *Zero Gravity Suspension Model 60350-0.*

[5] de Luca, A. Robots with flexible links: Modeling and control. 2003.

[6] Fischer, A. *Gravity Compensation of Deployable Space Structures.* PhD thesis, University of Cambridge, 2000.

[7] Gonzales, R.C. and Woods, R.E. *Digital Image Processing.* Addison-Wesley Publishing Company, 1992.

[8] Harvey, T.J. A second generation zero spring rate support system. *AIAA/AFOSR Workshop on Microgravity Simulation in Ground Validation Testing of Large Space Structures*, 1989.

[9] Jagannathan, S., Fenn, C.F., and Johnson, B.G. Low-cost active anti-gravity suspension system. *Proceedings of the American Control Conference*, pages 3606–3611, 1995.

[10] Leipold, M., et. al. Solar sail technology development and demonstration. *Acta Astronautica*, pages 317–326, 2003.

[11] Messerschmid, E. and Bertrand, R. *Space Stations - Systems and Utilization.* Springer, 1999.

[12] Osborne, J.P. *An Interactive Microgravity Drop Tower Controlled Through the World Wide Web.* PhD thesis, Tufts University, 1998.

[13] Pellegrino, S., Kebadze, E., Lefort, T., and Watt, A.M. Low-cost hinge for deployable structures. Technical Report CUED/D-STRUCT/TR202, University of Cambridge, Department of Engineering, 2002.

[14] Press, W.H., et. al. *Numerical Recipes in C : The Art of Scientific Computing.* Cambridge University Press, second edition, 1997.

[15] Watt, A.M. *Deployable Structures with Self-Locking Hinges.* PhD thesis, University of Cambridge, 2003.

Appendix A

Deployment Diagrams

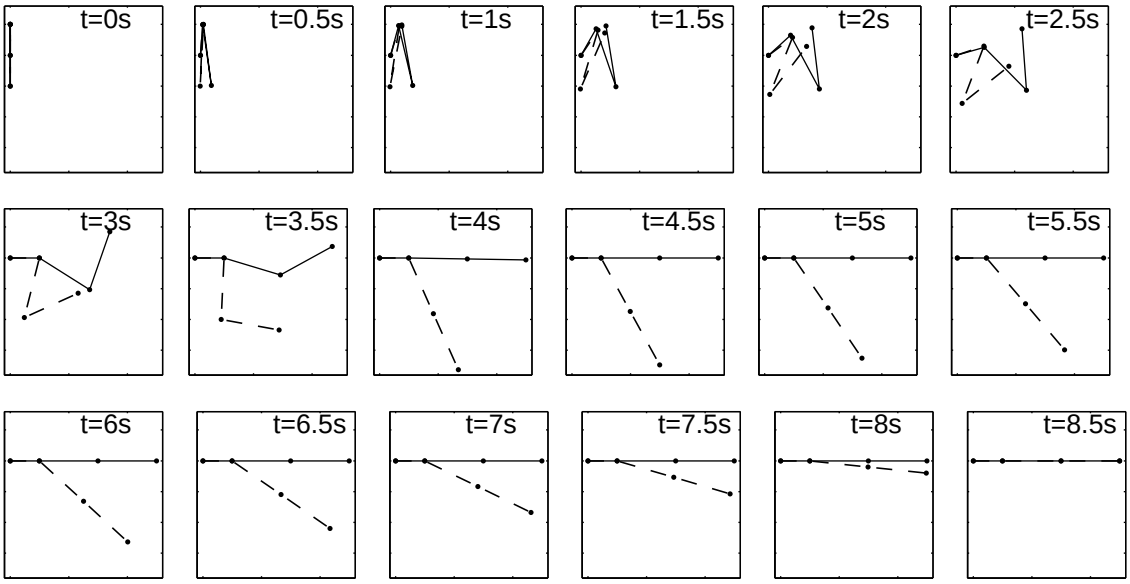

Figure A.1: Predicted Deployment of Test Array in Space With (solid line) and Without (dashed line) Initial Energy

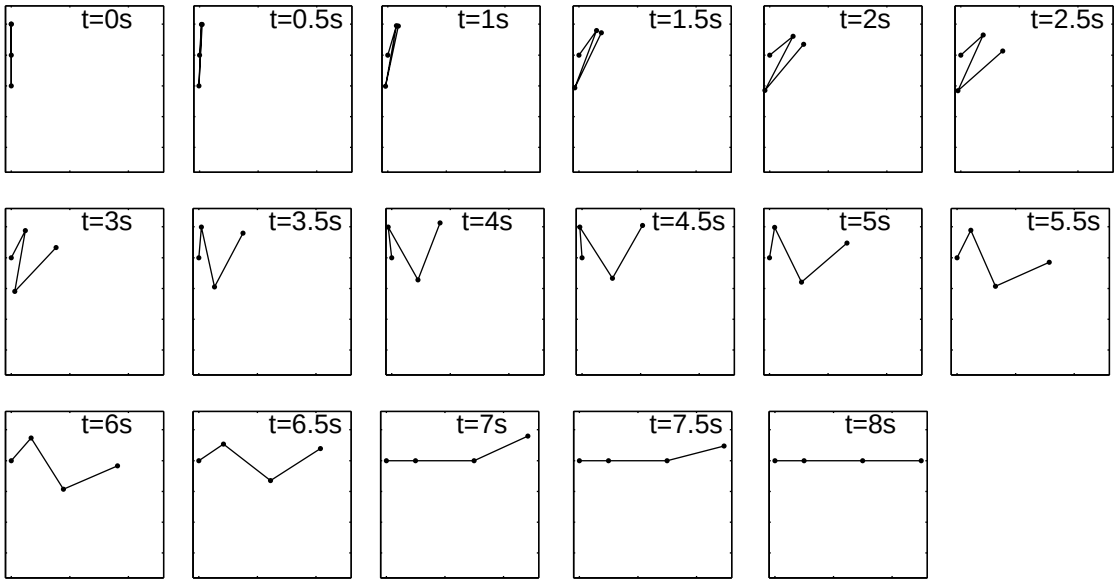

Figure A.2: Predicted Deployment of Test Panel on Ground

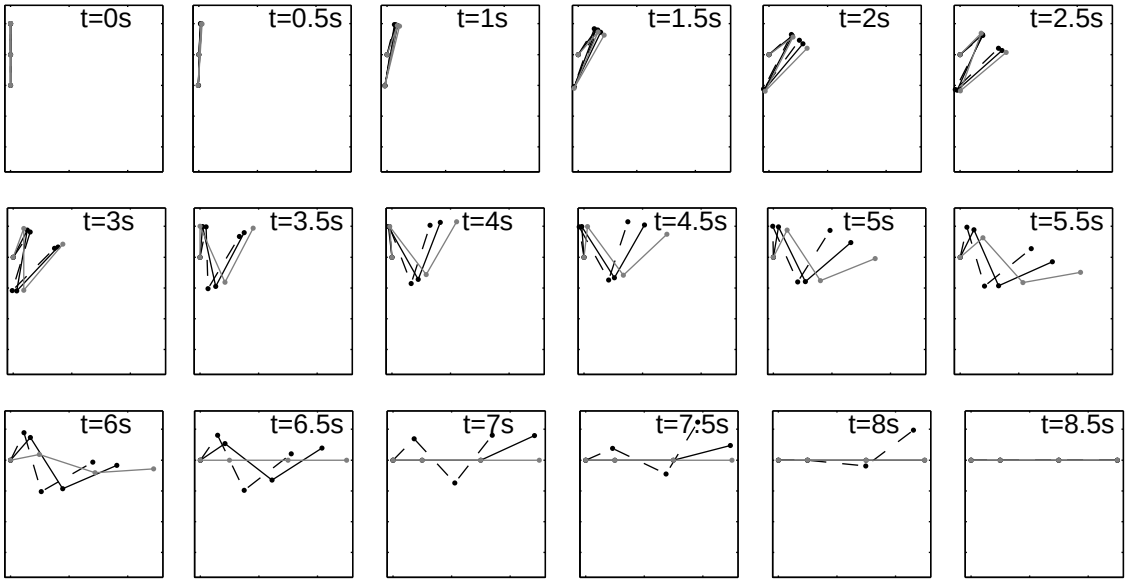

Figure A.3: Predicted Deployment of Test Panel on Ground, Sensitivity to the Moment in the Hinge Line; black solid line: standard value $M_{h0} = 0.2922Nm$, black dashed line: $M_{h0} = 0.25Nm$, grey solid line: $M_{h0} = 0.35Nm$

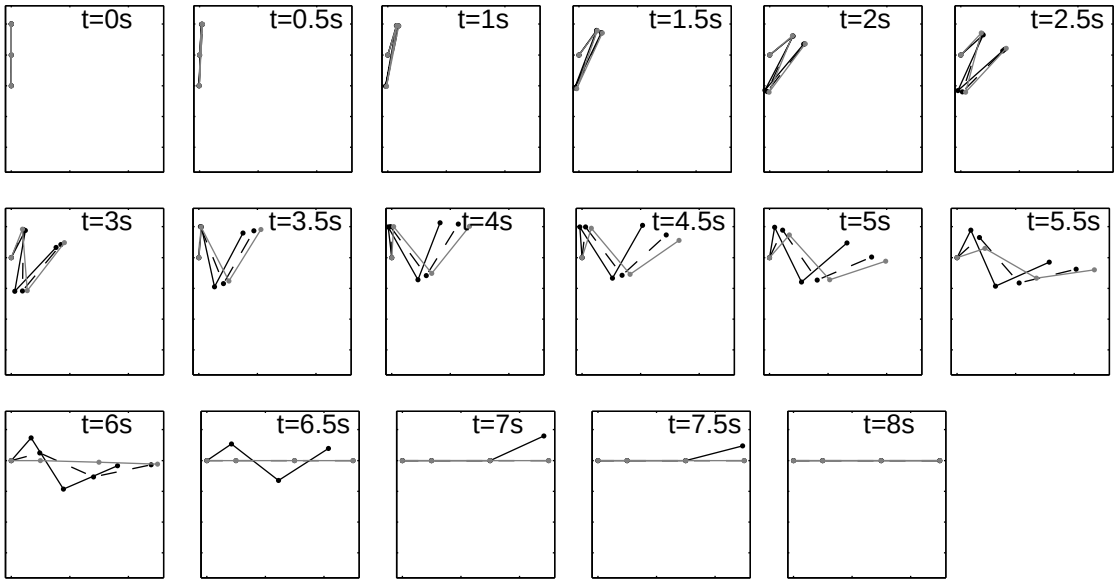

Figure A.4: Predicted Deployment of Test Panel on Ground, Sensitivity to Decreased Coefficient of Friction; black solid line: standard value $\mu = 0.002457$, black dashed line: $\mu = 0.001$, grey solid line: $\mu = 0.000$

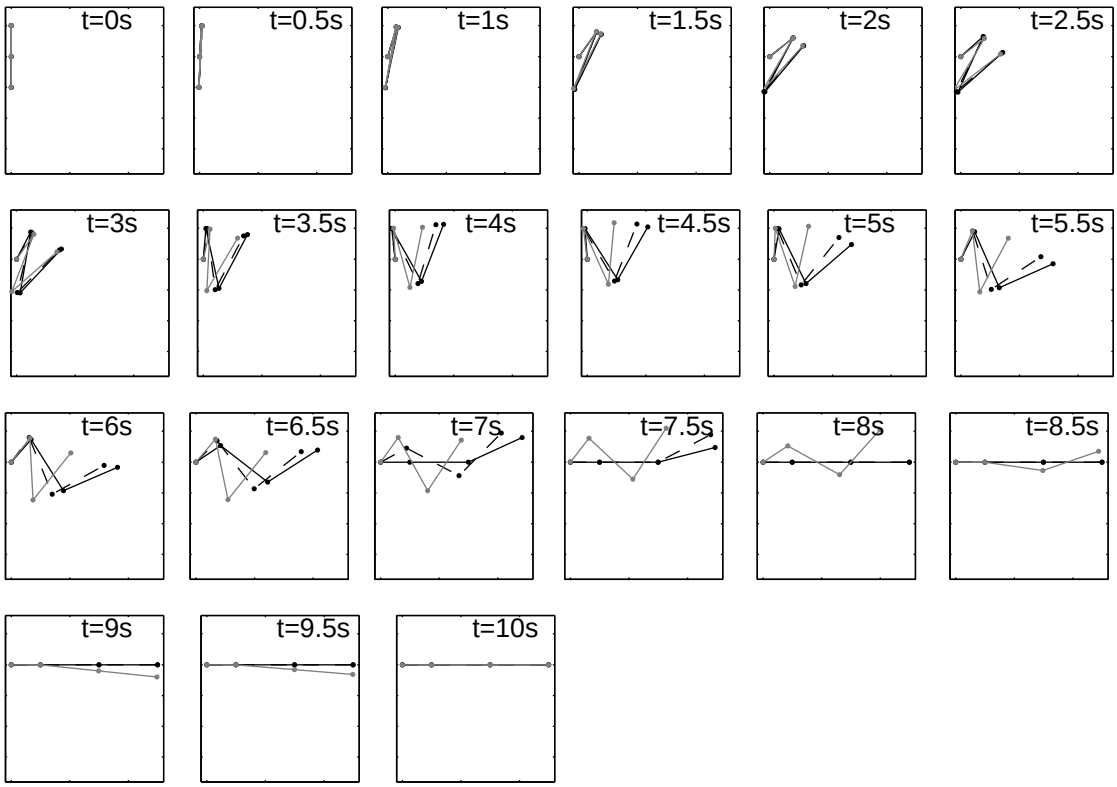

Figure A.5: Predicted Deployment of Test Panel on Ground, Sensitivity to Increased Coefficient of Friction; black solid line: standard value $\mu = 0.002457$, black dashed line: $\mu = 0.003$, grey solid line: $\mu = 0.004$

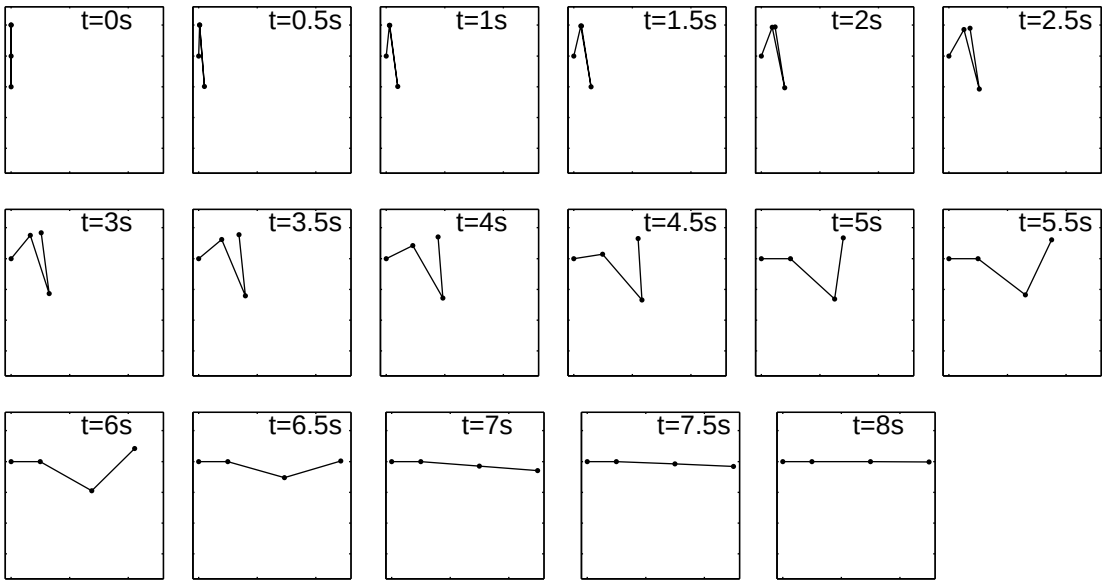

Figure A.6: Predicted Deployment of SSTL Array in Space with Initial Energy

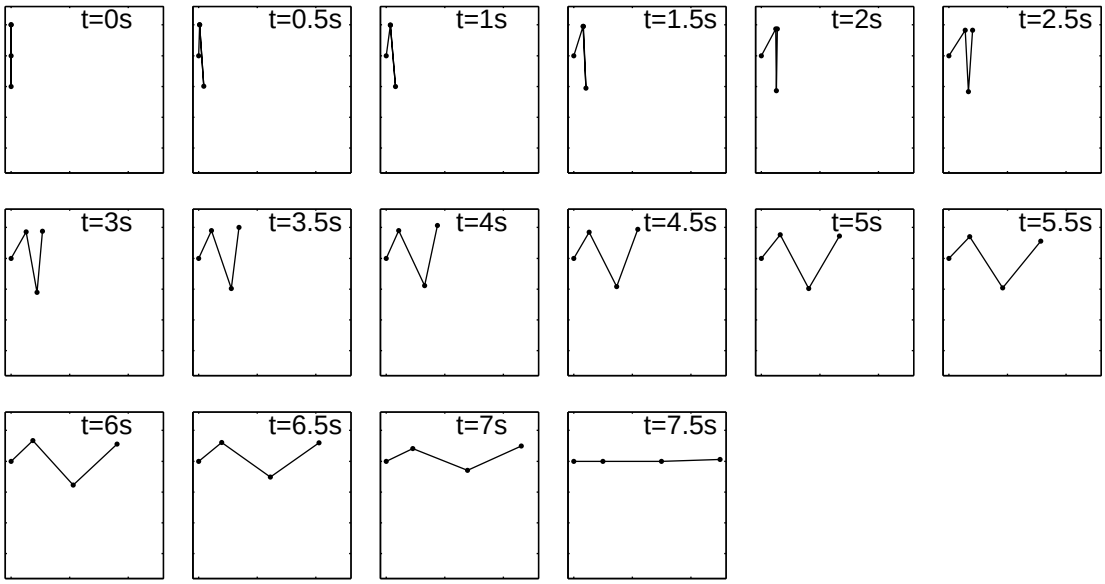

Figure A.7: Predicted Deployment of SSTL Array on Ground with Initial Energy

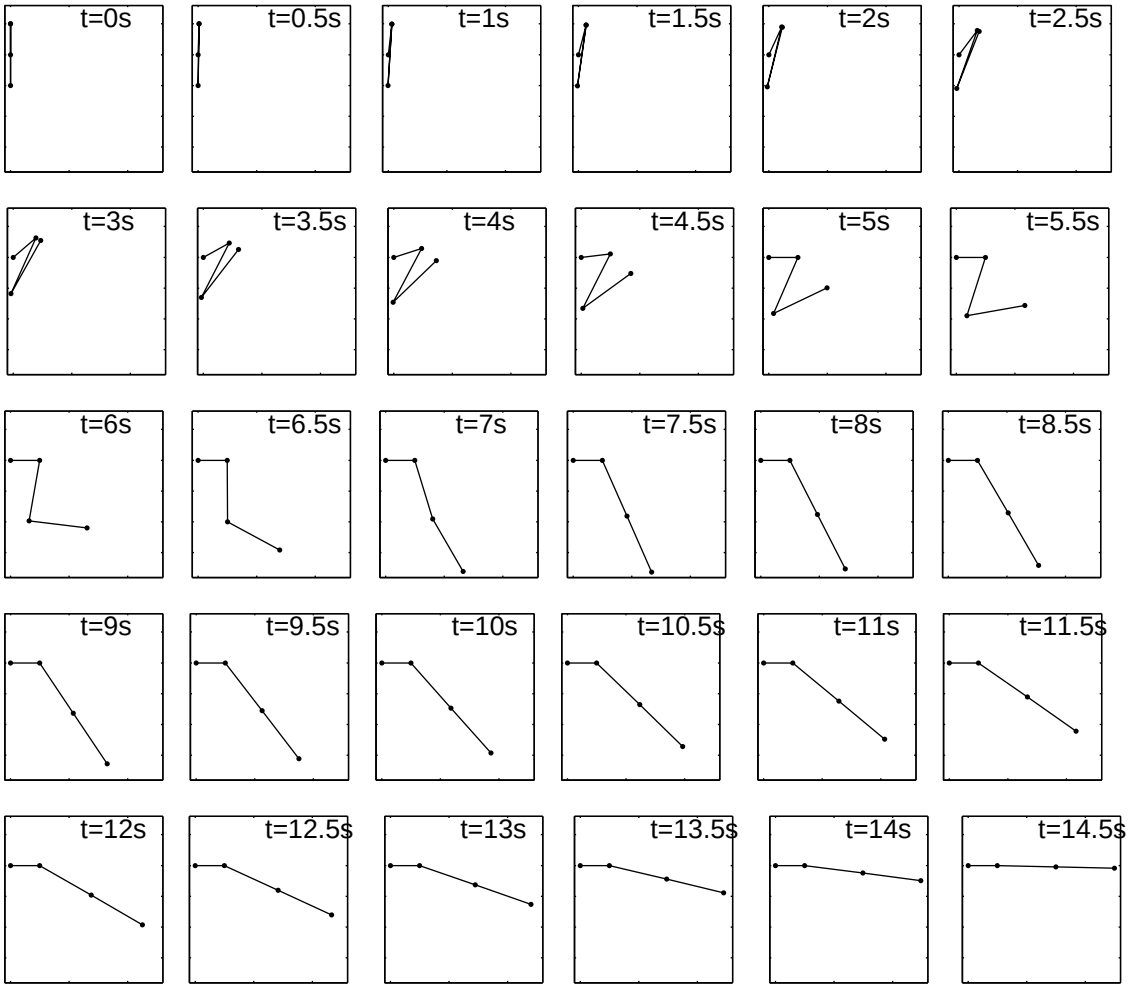

Figure A.8: Predicted Deployment of SSTL Array in Space without Initial Energy

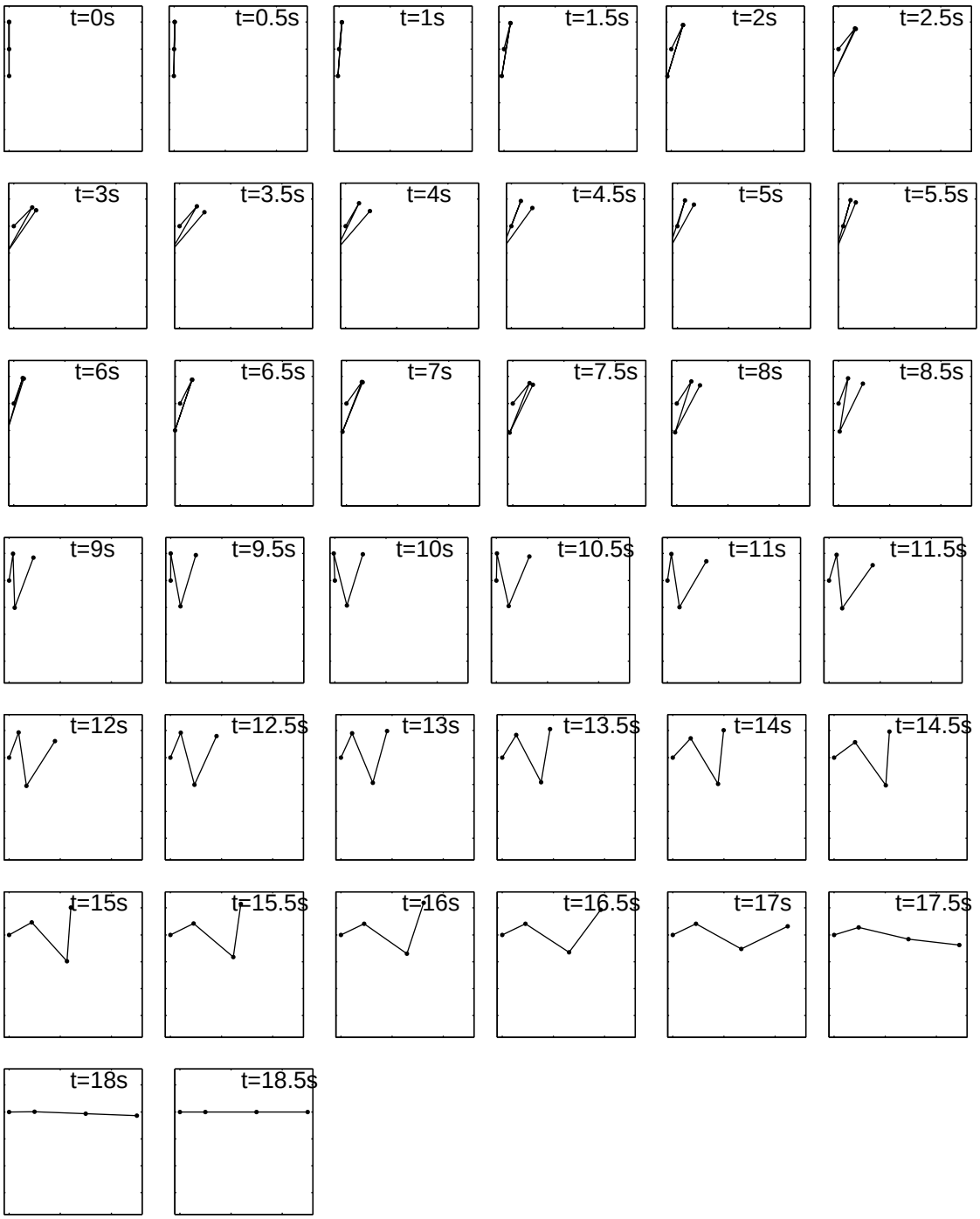

Figure A.9: Predicted Deployment of SSTL Array on Ground without Initial Energy

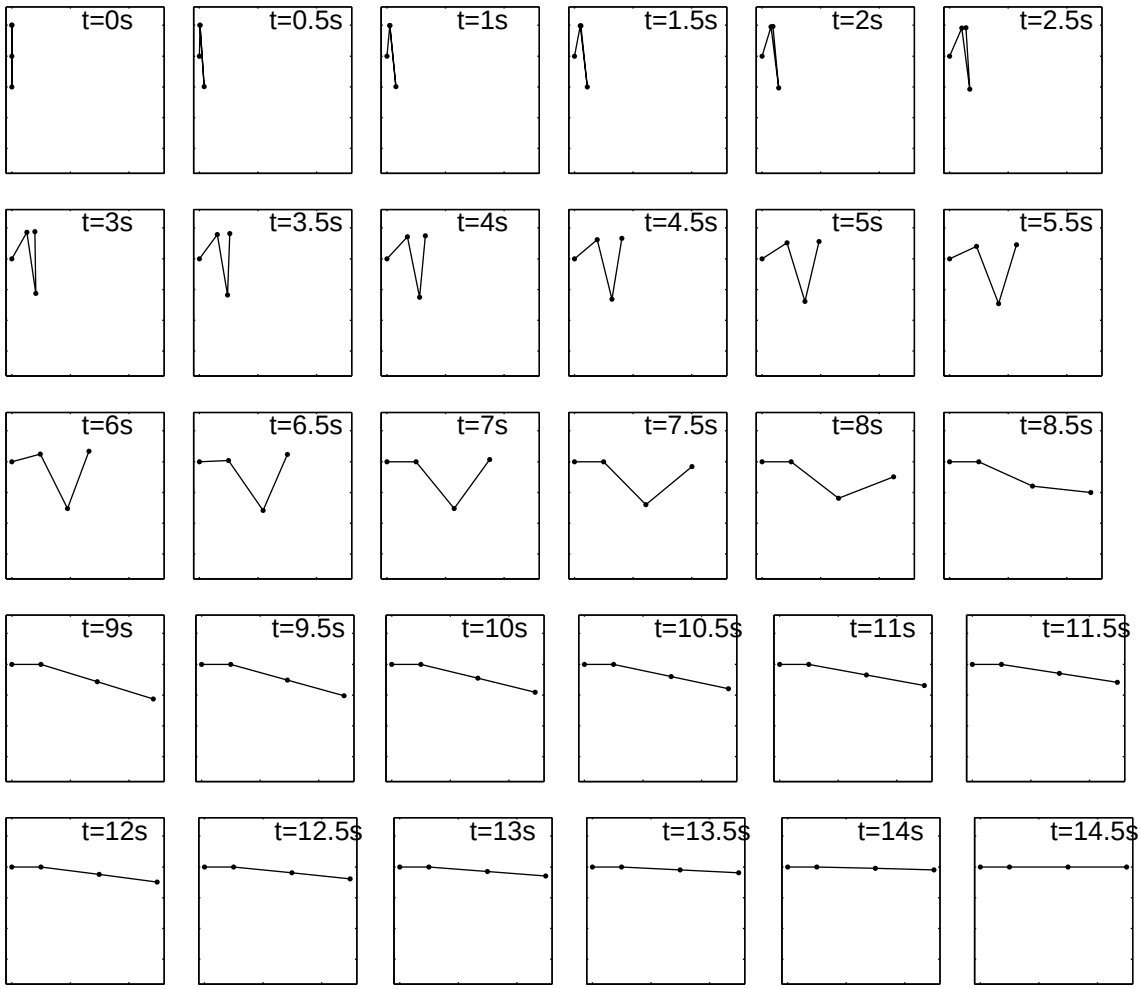

Figure A.10: Deployment of the SSTL Array in the Four-Rail Suspension System with Light-weight Transverse Rails

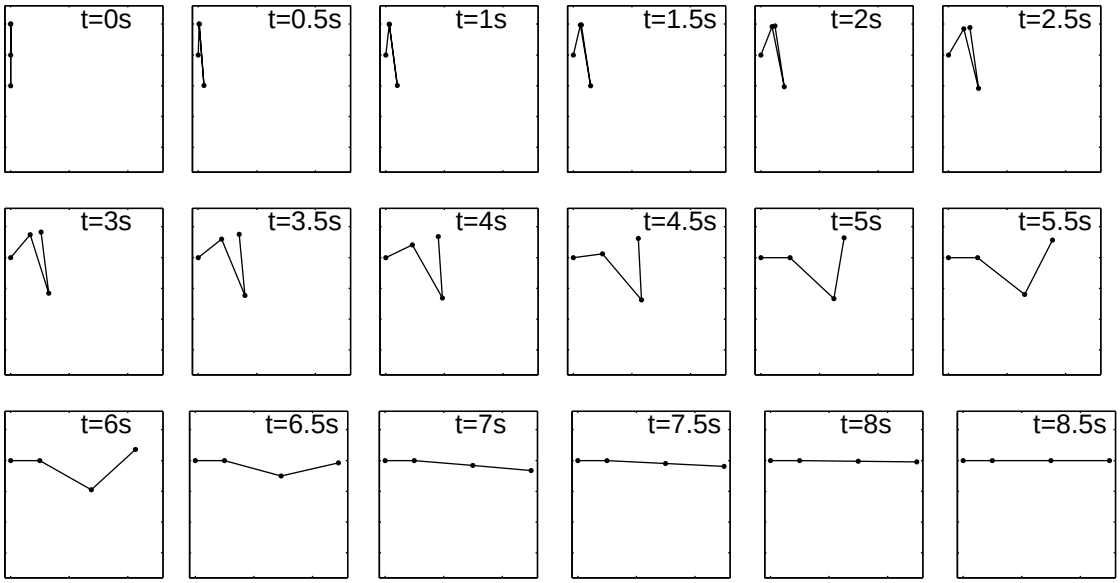

Figure A.11: Predicted Deployment of SSTL Test Array in Space

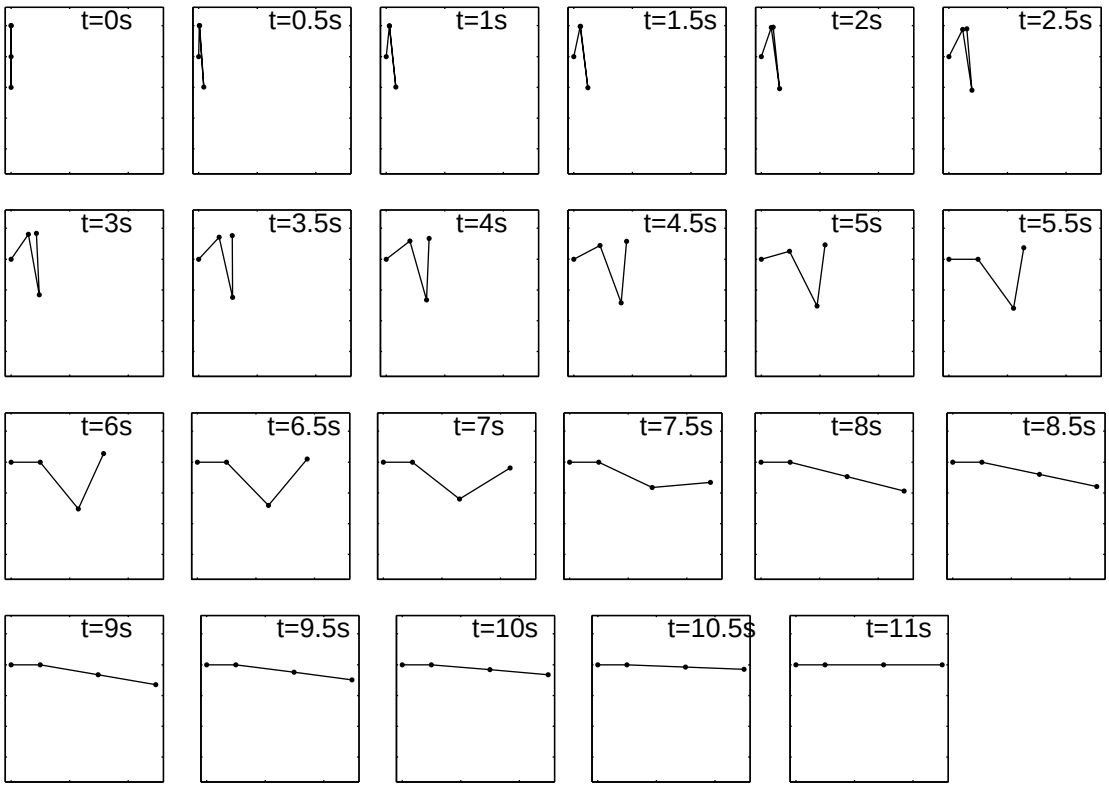

Figure A.12: Predicted Deployment of SSTL Test Array on Earth

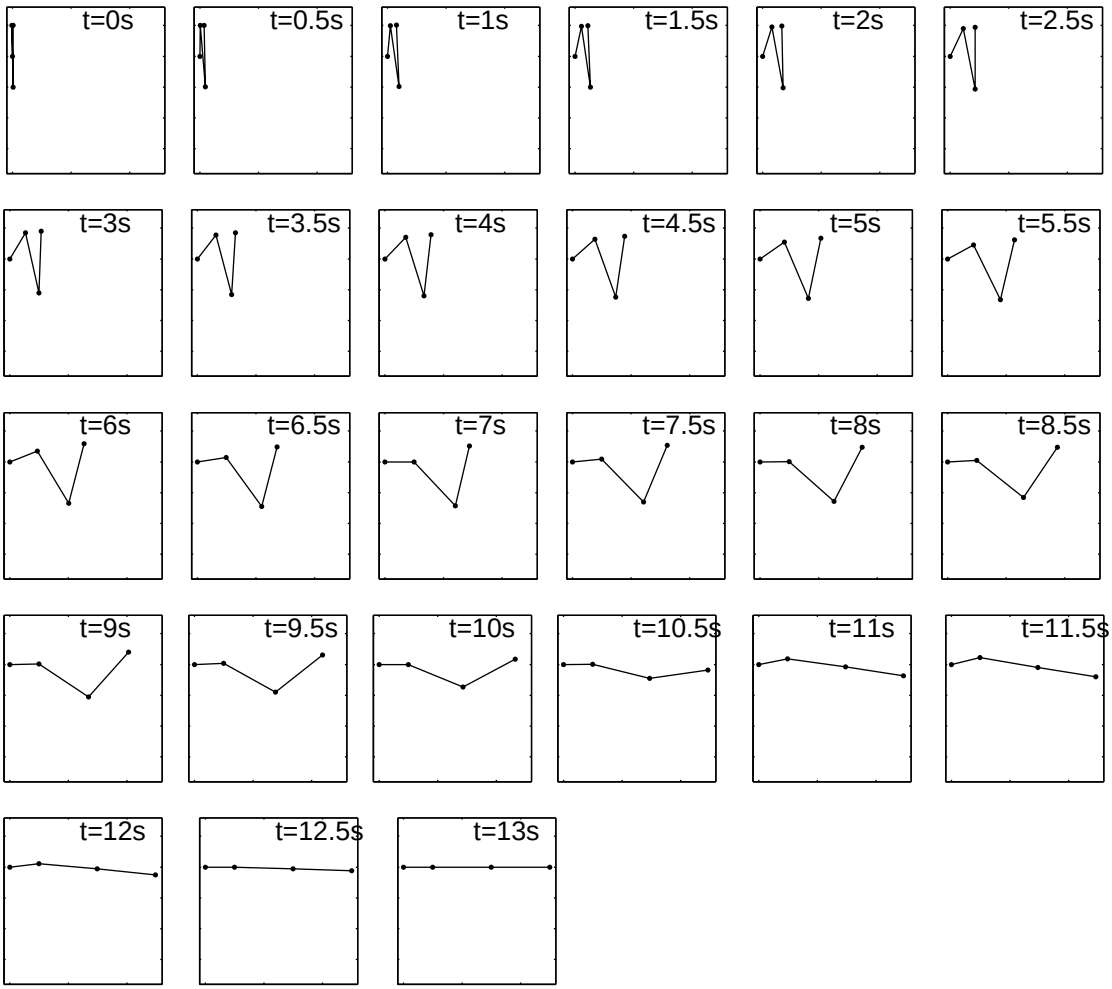

Figure A.13: Deployment of SSTL-Test Array, Results from Experiment

Appendix B

Photos

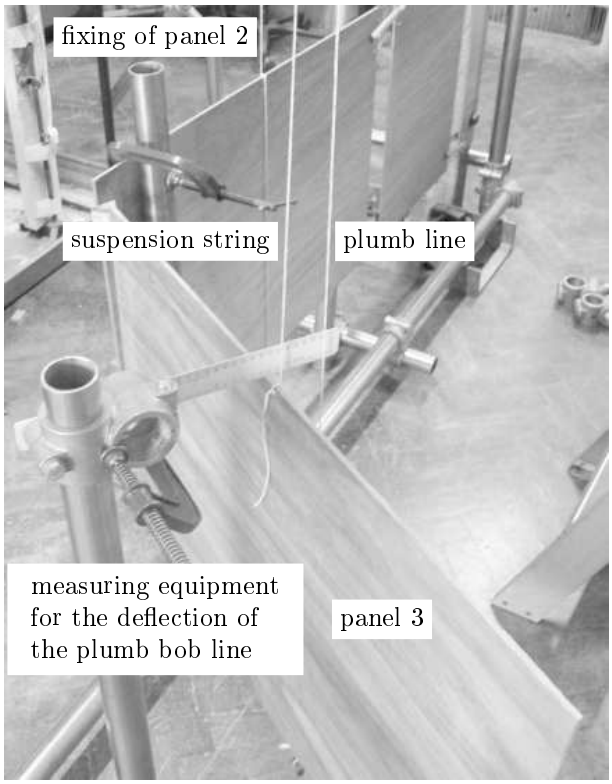

Figure B.1: Experimental Set-up for Measuring the Moment in Hinge Line H_3

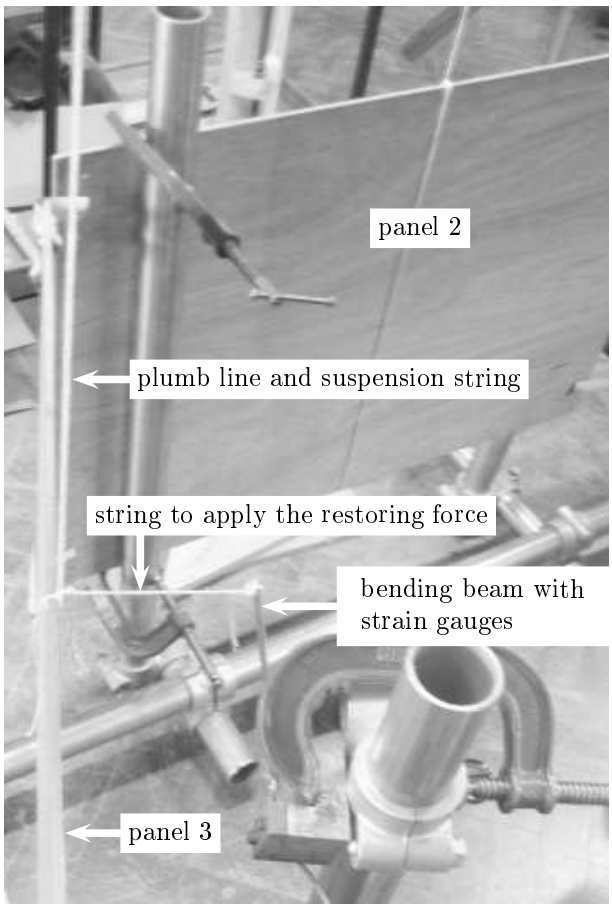

Figure B.2: Experimental Set-up for Measuring the Restoring Force. Notice that the suspension string is aligned with the plumb line

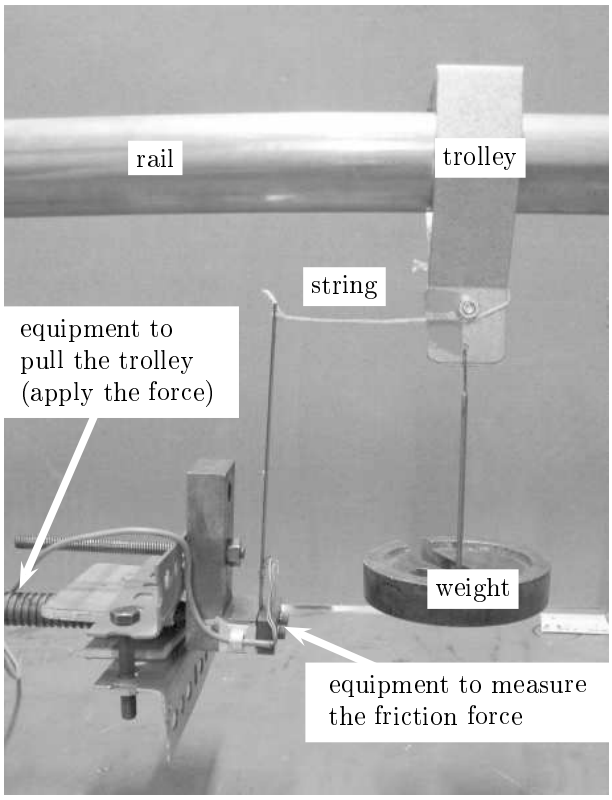

Figure B.3: Close-up of Trolley and Measuring Equipment

(a) The trolley is accelerated

(b) After the hand releases the trolley the velocity is measured using a plate which cuts off a light beam

(c) The trolley has stopped

Figure B.4: Experimental Method to Determine Kinetic Friction

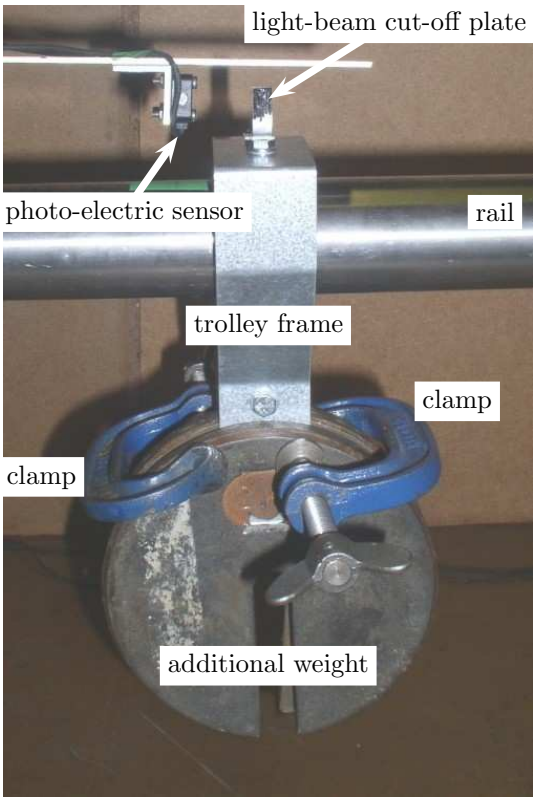

Figure B.5: Measuring the Velocity of the Trolley